

## Review

## Phase shifting algorithms for fringe projection profilometry: A review

Chao Zuo<sup>a,b,c,\*</sup>, Shijie Feng<sup>a,b,c</sup>, Lei Huang<sup>d</sup>, Tianyang Tao<sup>a,b,c</sup>, Wei Yin<sup>a,b,c</sup>, Qian Chen<sup>a,b</sup><sup>a</sup> School of Electronic and Optical Engineering, Nanjing University of Science and Technology, No. 200 Xiaolingwei Street, Nanjing, Jiangsu Province 210094, China<sup>b</sup> Jiangsu Key Laboratory of Spectral Imaging & Intelligent Sense, Nanjing University of Science and Technology, Nanjing, Jiangsu Province 210094, China<sup>c</sup> Smart Computational Imaging (SCI) Laboratory, Nanjing University of Science and Technology, Nanjing, Jiangsu Province 210094, China<sup>d</sup> Brookhaven National Laboratory, NSLS II 50 Rutherford Drive, Upton, New York 11973-5000, United States

## ARTICLE INFO

## Keywords:

Phase shifting profilometry  
Fringe projection  
3D shape measurement  
Phase unwrapping

## ABSTRACT

The principle of structured light and triangulation is used in a wide range of 3D optical metrology applications, such as mechanical engineering, industrial monitoring, computer vision, and biomedicine. Among a multitude of techniques based on this principle, phase shifting profilometry (PSP) plays a dominant role due to its high attainable measurement accuracy, spatial resolution, and data density. Over the past few decades, many PSP algorithms have been proposed in the literature in order to achieve higher measurement accuracy, lower pattern count, and/or better robustness to different error sources. Besides, many unconventional PSP codification techniques address the problem of absolute phase recovery with few projected patterns, allowing for high-efficiency measurement of objects containing isolated regions or surface discontinuities. In this paper, we present an overview of these state-of-the-art phase shifting algorithms for implementing 3D surface profilometry. Typical error sources in phase measurement for a phase shifting system are discussed, and corresponding solutions are reviewed. The advantages and drawbacks of different PSP algorithms are also summarized to provide a useful guide to the selection of the most appropriate phase shifting technique for a particular application.

## 1. Introduction

The physical world we live in is three dimensional (3D). The 3D acquisition and information processing technology reflects the ability of human beings to cognize and grasp the objective world, so to some extent it is an important symbol of human wisdom. Conventional cameras and imaging detectors can only acquire 2D intensity information of the scene but cannot record 3D shape and depth information. Although humans can perceive the depth based on the binocular stereopsis formed by the eyes, they cannot accurately quantify the 3D geometry of objects. To address this issue, 3D shape measurement technologies have been developed to quantitatively obtain 3D geometric information so as to provide a data basis for clearer understanding and better comprehension of the state and function of real-world objects.

The rapid development of modern information technology has promoted the gradual maturity of the 3D shape measurement technology, which has penetrated into almost all fields around us with different styles and characteristics. In industrial design, the reverse engineering based on 3D shape measurement can rapidly create the accurate and digitalized 3D CAD models of the existing products, significantly shortening the development cycle and facilitating the further engineering processes [1]. In the field of intelligent manufacturing, the 3D sensing technology

allows machines to perceive the 3D world, enabling a new starting point for manufacturing automation, intelligence, and re-creation [2]. In the field of virtual reality, a large number of digitized 3D scenes and models have been extensively used in national defense, simulated training, scientific experiments, and 3D animation [3]. In the field of cultural heritage preservation, 3D shape measurement technology has become an essential tool for the non-contact and non-destructive documentation of cultural heritage and its long term preservation [4]. In medical plastic surgery, 3D shape measurement technology has been widely used in facial soft-tissue repairing, surgical examination, and dentures customization [5]. And other applications exist in a variety of fields including manufacturing inspection, biomedicine, architecture, security, and human-computer interaction [6].

3D shape measurement techniques can be classified into two different categories, contact and non-contact [7]. Contact methods measure and reconstruct 3D geometry by probing the 3D surface through physical touch. An example of such a technique is the coordinate measurement machine (CMM) that can measure 3D geometry through a precise carriage system or articulated probe arm [8]. While this type of measurement can achieve high accuracy, it is typically limited to low measurement efficiency, since the system uses a physical probe that needs to touch the object surface point-wisely. Furthermore, due to the neces-

\* Corresponding author at: School of Electronic and Optical Engineering, Nanjing University of Science and Technology, No. 200 Xiaolingwei Street, Nanjing, Jiangsu Province 210094, China.

E-mail addresses: [zuochao@njjust.edu.cn](mailto:zuochao@njjust.edu.cn) (C. Zuo), [chenqian@njjust.edu.cn](mailto:chenqian@njjust.edu.cn) (Q. Chen).

<https://doi.org/10.1016/j.optlaseng.2018.04.019>

Received 15 February 2018; Received in revised form 15 April 2018; Accepted 30 April 2018

Available online 15 May 2018

0143-8166/© 2018 Elsevier Ltd. All rights reserved.

sity of physical contact, it is undesirable for the measurement of soft or deformable objects. In order to solve the problems associated with contact-based techniques, a number of non-contact 3D shape measurement methods have been developed and are now increasingly being used in different fields. Optical methods lead the way in this category with the advances of high-performance light source and imaging devices. Various optical metrology approaches for 3D shape measurement have been developed, such as optical interferometry [9–11], time-of-flight (TOF) technique [12,13], stereo vision [14,15], shape from focus [16–18], and structured light (SL) [19–22]. These methods are based on different principles of optical measurement and have specific measurement sensitivity, spatial/temporal resolution, and measurement range. Readers interested in the basic principle, properties, and application ranges of these optical 3D shape measurement methods can refer to the review articles by Chen et al. [23] or Blais et al. [24].

The following of this paper is focused on the SL technique. SL is a very popular non-contact 3D shape measurement technique with the advantages in terms of simple hardware configuration, high measurement accuracy, high point density, high speed, and low cost. It has found extensive applications in industry and scientific researches. In essence, SL methods can be regarded as a modification of stereo vision. One of the cameras is replaced by a light source which projects the light patterns onto the scene. Since the object surfaces are covered with artificial features created by projected light patterns, the correspondence problem in the (passive) stereo vision for texture-less objects can be easily overcome. A typical 3D shape measurement system based on SL consists of one projection unit and one or more cameras. During the measurement, light patterns with known structures are projected sequentially onto the object being measured. Meantime, images of the object under the light projections are captured by the camera(s). By utilizing triangulation method between the camera and the projector (or between two cameras) and knowledge on the light patterns, the 3D shape of the object can be reconstructed from the captured images based on the pre-calibrated geometric parameters of the SL system. New researchers in this area are recommended to first read the tutorial by Geng et al. [22].

Over the past few decades, 3D shape measurement techniques based on SL have been rapidly developed in both communities of computer vision and optical metrology, and there have been many technical review articles survey and summarize previously published studies from different perspectives [22,25–31]. In the computer vision community, SL technique is also called 3D scanning, and the SL pattern codification strategies are mainly based on discrete intensity-based approaches. They can be further classified into spatial codification approaches and temporal codification approaches. In spatial codification approaches, e.g. De Bruijn patterns [19,20,32], non-formal coding [33,34], and M-arrays [35], the codeword of a specific position is extracted from surrounding points. The key idea is to guarantee the uniqueness of the local codeword over the global range in the pattern. Temporal codification methods are based on the codeword created by the successive projection of patterns onto the object surface. Therefore, the codeword associated to an image pixel is not completely formed until all patterns have been projected. Examples of these temporal codification methods include the temporal binary code [36], temporal n-ary code [37], and gray code [38]. Besides, color patterns or color multiplexing SL approaches with red, green, and blue channels have been proposed to improve the coding efficiency and reduce the number of projected patterns [30,37,39,40]. For more details about the principle and practical performance of these SL codification schemes, readers can access the review articles by J. Salvi et al. [26,27].

In the field of optical metrology, the most commonly used type of SL pattern for 3D shape measurement is fringe patterns, particularly fringe patterns with sinusoidal intensity distributions. Besides, the codification schemes used are mainly focused on continuous phase-based approaches. These sinusoidal SL techniques are often referred as fringe projection profilometry (FPP). By projecting sinusoidal fringe patterns onto the object and capturing the corresponding deformed fringe patterns modulated by the object surfaces, the depth information is encoded

into the phase of the fringe images. The recorded modulated fringe images are then processed by fringe analysis algorithms to extract the phase distribution, which is thereby used to recreate the surface of interest in 3D space based on geometrical relations of the triangulation optical arrangement. For a general overview of FPP, readers can refer to the review article by Gorthi and Rastogi [25]. Traditionally, the typical approach to FPP involves generating fringe images by using laser interferometry, physical grating, or slide projector. However, with more recent developments in the area of digital display, digital video projectors have been increasingly used as the projection units of FPP systems. In contrast to the traditional methods of generating fringe images, digital video projectors are able to accurately control various attributes of the projected fringe patterns at high speed in software, which ultimately facilitate the effective applications of FPP techniques. It should be also mentioned that another classic approach to generate sinusoidal fringe patterns is based on the moiré effect. The application of moiré fringes for surface topology, so-called moiré topography, was first investigated in the late 1960's [41,42], which can be implemented in one of two variations: shadow moiré [43,44] and projection moiré [43–45]. In shadow moiré approaches, a single grating is used to cast a shadow onto the surface to be profiled which is imaged through the same grating from an offset angle to create moiré fringes whose phases are proportional to depth [46,47]. In projection moiré approaches, grating lines are directly projected onto the object surface, and moiré fringes are resolved by applying another reference grating either optically or digitally [43–45,48], so projection moiré topography can be regarded as a predecessor of FPP.

Benefiting from the continuity and periodicity nature of sinusoidal patterns, the FPP generally provides 3D data with both high spatial resolution and high depth accuracy. Considering the means of phase demodulation, the most popular FPP approaches includes Fourier transform profilometry (FTP) and phase shifting profilometry (PSP). The FTP utilizes only a single high-frequency fringe pattern, and the phase is extracted by applying a properly designed band-pass filter in the frequency domain. More technical details about FTP approaches can be found in the review article by Su and Chen [49]. The single-shot nature of FTP makes it highly suitable for the 3D shape measurement of dynamic surfaces. The review article by Su and Zhang provides an overview of dynamic shape measurement based on FTP and its typical applications [28]. Besides, not just limited to FTP, the windowed Fourier transform (WFT) [10,50] and the wavelet transform (WT) [51] can also be used for the phase demodulation of single high-frequency fringe pattern. It has been found that the WFT can provide higher measurement accuracy even in the presence of intensity nonlinearity error and depth discontinuities. For relevant content, readers can refer to the comparison papers by Huang et al. [52] and Zhang et al. [53].

In contrast to FTP, the PSP generally requires more than one (normally at least three) phase-shifted fringe patterns to reconstruct the 3D shape of the object. PSP originally stems from the classical laser interferometry technique. Srinivasan et al. [54] first introduced the phase shifting algorithm into the field of FPP for high-accuracy 3D shape measurement in 1984. Shortly afterwards, the PSP technique was successfully applied to the complete 360° reconstruction of a general 3D diffuse object [55]. Since the mathematical representation of the deformed fringe image intensity distribution is similar to that encountered in conventional optical interferometry, the methods of phase shifting interferometry (PSI) [56,57], well known for their accuracy, can be directly used for the fringe analysis and phase demodulation in FPP. Compared to FTP, the multiple-shot PSP techniques are generally more robust and can achieve pixel-wise phase measurement with higher resolution and accuracy. Furthermore, the PSP measurement is quite robust to ambient illumination and varying surface reflectivity. However, the PSP techniques require more time to acquire the multiple fringe patterns, and the object should be kept stationary during the projection of multiple fringe patterns. Recently, with the rapid advances in high-frame-rate image sensors, high-speed digital projection technology, and high-performance processors, PSP techniques have been increasingly applied

in high-speed, real-time 3D shape measurement of dynamic scenes. More in-depth contents about real-time FPP can be learned in the review articles by Zhang [29] and Jeught and Dirckx [31].

For both the PSP and the FTP, the retrieved phase distribution corresponding to the object height is mathematically wrapped to principle values of arctangent function ranging between  $-\pi$  and  $\pi$ , and consequently, the phase discontinuities occur at the limits every time when the unknown true phase changes by  $2\pi$ . This is the so-called phase ambiguity problem, resulting from the periodical nature of the sinusoidal signal. To establish a unique pixel correspondence between the camera and the projector (or between two cameras), the phase unwrapping must be carried out. Several dozen algorithms have been proposed for 2D phase unwrapping, and they can be divided into two principal groups: spatial phase unwrapping and temporal phase unwrapping. Spatial phase unwrapping usually requires only a single wrapped phase map. By assuming the phase continuity, the unwrapped phase of a given pixel is derived according to the phase values within a local neighborhood of the pixel. With different considerations, a number of spatial phase unwrapping methods have been investigated in variety, such as Goldstein's method [58], quality-guided method [59], Flynn's method [60], and minimum  $L_p$ -norm method [61]. There have been many reviews on the general subject of phase unwrapping [62,63] as well as comparison of different unwrapping algorithms for particular applications [64–66]. However, limited by the precondition of phase continuity, the spatial phase unwrapping cannot handle large surface discontinuities (phase difference between adjacent pixels  $\geq \pi$ ) and isolated objects. Temporal phase unwrapping methods overcome this problem by employing more than one wrapped phase maps or additional black and white coded patterns to provide extra information about the fringe orders [67–77]. The phase ambiguity problem is fundamentally addressed, and each spatial pixel is unwrapped independently from its neighbors. Typical temporal phase unwrapping algorithm includes gray-code approaches [38,67], multi-frequency (hierarchical) approaches [68,69,78], multi-wavelength (heterodyne) approaches [70,71,79], and number theoretical approaches [72,73,80,81]. For more details about the basic principle and practical performance of these methods, readers can refer to the comparative review by Zuo et al. [82].

This article aims to provide a review of the different phase shifting algorithms used in fringe projection techniques. Though there are many excellent books and reviews which deal with the variety of phase shifting techniques in the field of optical interferometry [11,57,83,84], they mainly focuses on conventional sinusoidal phase shifting techniques where the fringe patterns are generated by two-beam interference. However, in digital FPP, the fringe pattern can be created with theoretically any intensity profile using computer software and projected onto the object surface through an off-the-shelf digital projector such as liquid crystal device (LCD), digital mirror device (DMD), and liquid crystal on silicon (LCOS) projectors. Over the past few decades, several FPP approaches based on phase shifting techniques have been proposed in the literature [54,85–104], which provide much more flexible solutions for high-accuracy, efficient, and robust phase retrieval by using or designing different types of intensity patterns. Besides, many novel phase shifting codification techniques have the built-in capabilities of absolute phase recovery and/or temporal phase unwrapping, allowing for high efficiency measurement of complicated objects or surfaces [105–116]. However, there is no previous work summarizing and comparing these approaches together. Therefore, properties extracting and attributes analyzing of these PSP approaches are still missing. This is overcome in the present review, which will focus on these PSP algorithms and analyzes and assesses their respective merits and drawbacks. Because each algorithm has its own features and no single algorithm can be universally applied in any practical situations, the selection of a proper phase shifting algorithm for a particular application needs careful trade-off considerations, which will be also discussed in this work.

The reminder of this paper is organized as follows. In Section 2, the image formation model of FPP is introduced. Section 3 reviews several

phase shifting algorithms for wrapped phase retrieval in FPP. Several error sources in a typical phase shifting system and their corresponding solutions are discussed in Section 4. Section 5 presents another group of phase shifting algorithms which can recover the absolute phase distribution. The characteristics of the reviewed phase shifting algorithms are summarized and compared in Section 6 in order to help the selection of a proper method for a specific application. Section 7 discusses several important issues regarding improving the measurement accuracy and efficiency of PSP techniques. Finally, conclusions are drawn in Section 8.

## 2. Image formation in FPP

Before reviewing different PSP phase retrieval algorithm, we must make clear how the captured fringe images are formed in a practical FPP system. This will be served as a basis to understand the basic principle underlying the pattern codification strategies for different PSP algorithms. In general, the image acquisition procedure in FPP can be divided into the following 3 steps [109,117,118]:

(1) Fringe projection. Some pre-defined fringe patterns are generated by a computer and projected through a projector onto the surface of the measured object. A typical sinusoidal fringe pattern designed in projector space can be represented as

$$I^p(x^p, y^p) = a^p + b^p \cos(2\pi f_0^p x^p) \quad (1)$$

where  $a^p$  is the mean value,  $b^p$  is the amplitude (or projector modulation),  $(x^p, y^p)$  is the pixel coordinate of the projector,  $f_0^p$  is the frequency of the sinusoidal fringe (period/pixel). Without loss of generality, we assume that the fringes are oriented perpendicular to the  $x^p$ -axis, that will be used when triangulating with the camera, which is positioned horizontally besides the projector. When the fringe pattern is sent to a projector, the output light is just the projected fringe image,  $I^p(x^p, y^p)$ .

(2) Fringe reflection. When the fringe pattern is projected onto the object surface, it will be distorted and reflected by the object surface, point by point. The reflected light is attributed to two sources: the projector light as well as the ambient light. The projected fringe pattern  $I^p$  combined with the ambient light  $\beta_1$  is modulated and reflected by the object.

(3) Fringe acquisition. The camera captures the distorted fringe images, point by point. The captured light includes the light reflected by the object as well as some additional ambient light  $\beta_2$  directly entering the camera. So the fringe image finally captured by the camera is:

$$I(x, y) = \alpha(x, y) \{ a^p + b^p \cos[\phi(x, y)] + \beta_1(x, y) \} + \beta_2(x, y) \quad (2)$$

where  $(x, y)$  is the pixel coordinate in the camera space,  $\alpha(x, y)$  is the surface reflectivity of the measured object (strictly speaking,  $\alpha(x, y)$  is the reflectance corresponding to the Lambertian component of the surface reflection, which depends on the surface normal according to the Lambert's cosine law), and  $\phi(x, y)$  is the phase of the distorted fringe containing the depth information of the object surface. The fringe projection, reflection, and acquisition steps as well as the whole image formation process in FPP are clearly illustrated in Fig. 1.

The form of  $I(x, y)$  given by Eq. (2) is very complicated, and generally the quantity of the interest is the phase component of the fringe image. For simplicity, in most literature of FPP,  $I(x, y)$  is expressed as

$$I(x, y) = A(x, y) + B(x, y) \cos[\phi(x, y)] \quad (3)$$

where  $A(x, y)$  is the average intensity of the fringe image, and  $B(x, y)$  is the so-called intensity modulation. They are closely related to the actual physical parameters of the surface reflectivity and ambient light according to the following relations

$$A(x, y) = \alpha(x, y) [a^p + \beta_1(x, y)] + \beta_2(x, y) \quad (4)$$

and

$$B(x, y) = \alpha(x, y) b^p \quad (5)$$

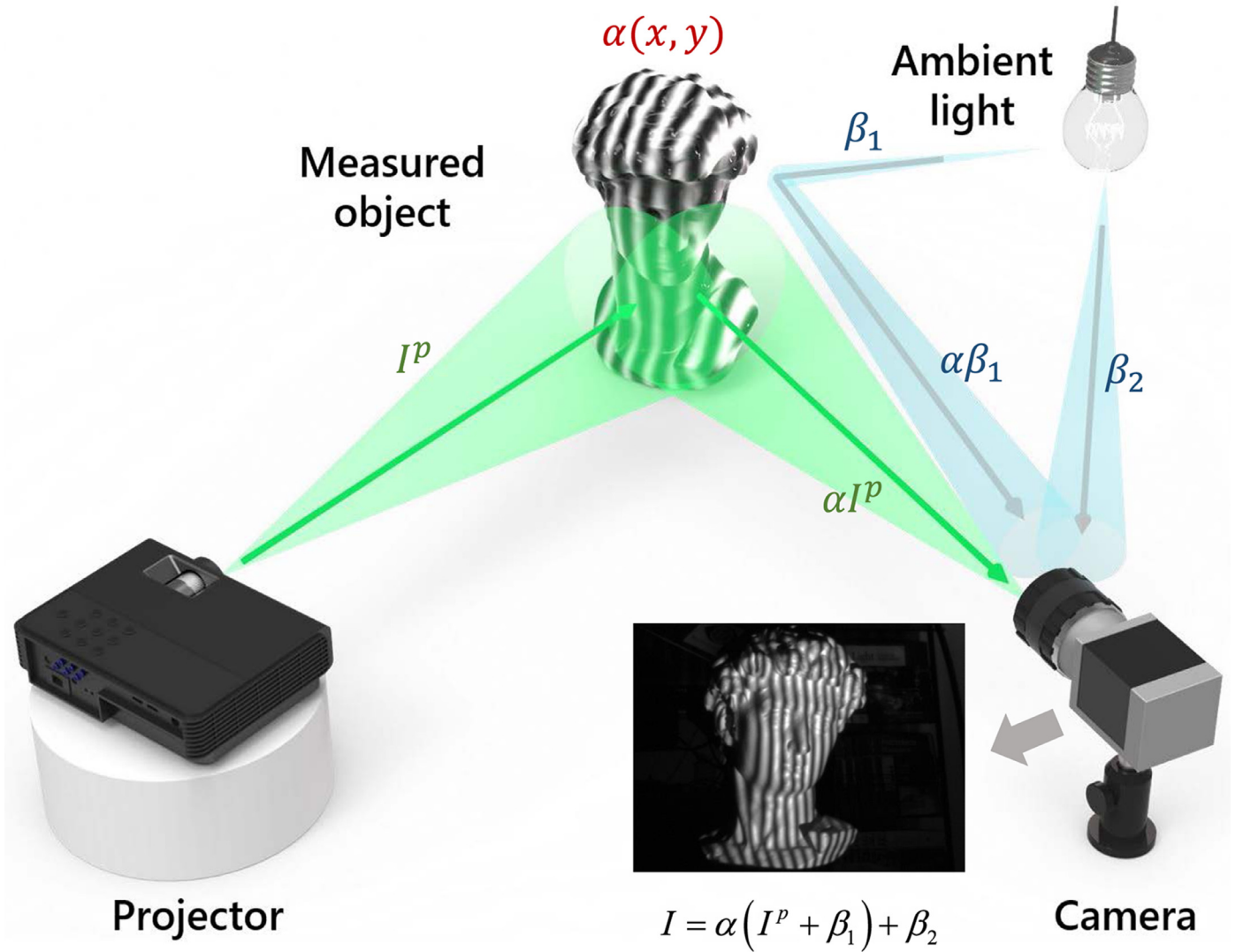


Fig. 1. Illustrations of fringe projection, reflection, and acquisition process.

Fig. 2 shows an example scene with the above-mentioned parameters, such as average intensity, intensity modulation, and phase distribution retrieved by a standard phase shifting algorithm. It can be seen clearly that the average intensity  $A(x, y)$  is equivalent to a normal ‘fringe-free’ image of the scene captured under uniform illumination  $a^p$  from the projector [Figs. 2(b)]. So it is usually used for texture mapping purposes. The intensity modulation  $B(x, y)$  is directly proportional to the surface reflectivity  $\alpha(x, y)$ , which is a quantitative indicator of the signal strength for each object point [Fig. 2(d)]. In many practical applications, the shape of the object and environmental lighting conditions vary a lot and may make some areas saturated or too dark to analyze properly. For these areas, the signal-to-noise ratio (SNR) is very low and the calculated phase information may not be correct [see Fig. 2(c)]. For background, dark or saturated region where  $I(x, y)$  is less modulated by the projected sinusoidal patterns,  $B(x, y)$  will be close to zero. Therefore,  $B(x, y)$  is often employed as a shadow noise detector/filter such that the shadow-noised regions, with  $B(x, y)$  values smaller than a pre-defined threshold, are excluded in the subsequent processing and depth reconstruction [see Fig. 2(e) and (f)].

### 3. Phase shifting algorithms for FPP

The PSP is one of the most widely used and precise strategies among the many proposed SL methods. Over the past few decades, many PSP

algorithms have been proposed or extended from the field of PSI, for example, standard  $N$ -step phase shifting algorithm [54], double 3-step algorithm [90], Hariharan 5-step algorithm [85], modified 2+1 algorithm [100], trapezoidal phase shifting [94], triangular phase shifting [99],  $\pi$ -shift FTP [86] etc. In this section, we will present an overview of these PSP strategies and discuss their respective properties.

#### 3.1. Standard $N$ -step phase shifting

The canonical PSP technique employs a set of phase-shifted sinusoidal wave patterns such that at the point  $(x^p, y^p)$ , in projector space, the intensity values are assigned as:

$$I_n^p(x^p, y^p) = a^p + b^p \cos(2\pi f_0^p x^p - 2\pi n/N) \quad (6)$$

where  $n$  represents the phase-shift index  $n = 0, 1, 2, \dots, N - 1$ . The mean value  $a^p$  and amplitude  $b^p$  are normally both 0.5 in order to cover the entire dynamic range of the projector (without loss of generality, here we assume the projector has a dynamic range of  $[0, 1]$ ). Fig. 3 shows a group of sinusoidal wave patterns with  $N = 3$ ,  $f_0^p = 5$  (/1000 pixel),  $a^p = b^p = 0.5$ . After projecting the patterns sequentially onto the object surface, the distorted fringe distribution, denoted as  $I_n(x, y)$  captured by the camera is:

$$I_n(x, y) = A(x, y) + B(x, y) \cos[\phi(x, y) - 2\pi n/N] \quad (7)$$

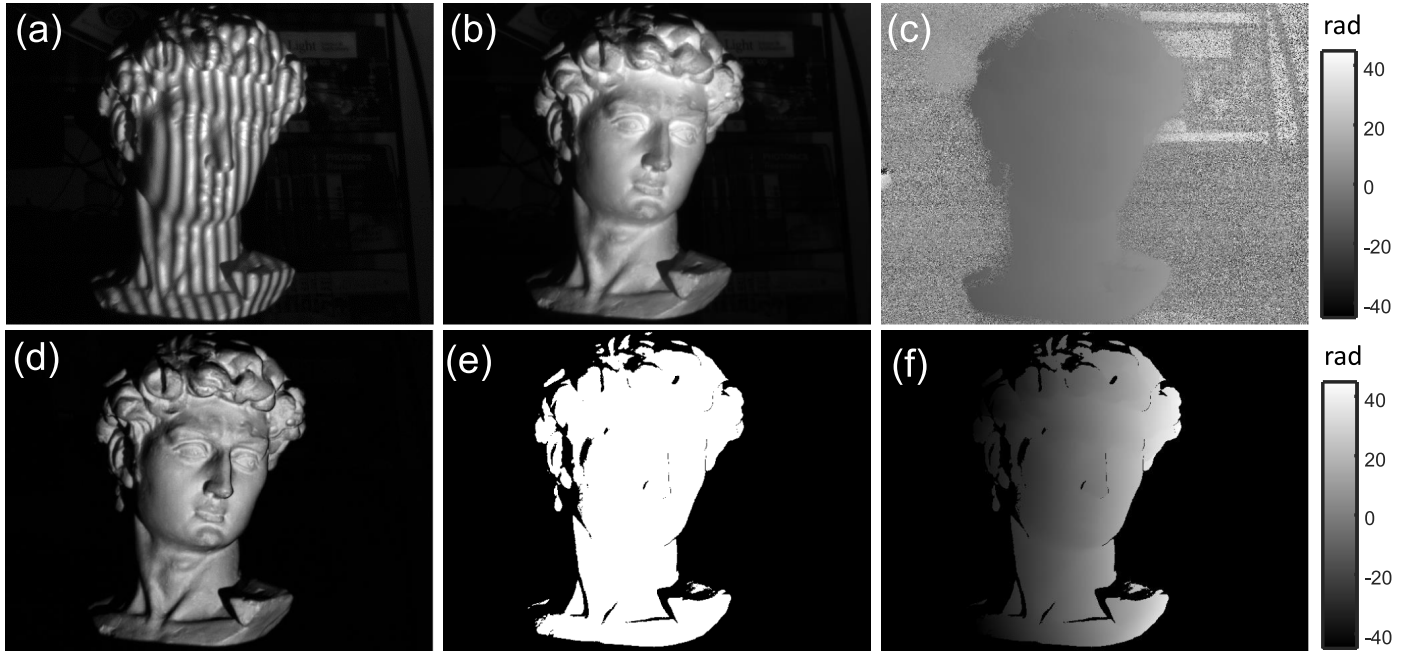


**Fig. 2.** Phase shifting measurement of a typical scene containing a plaster statue. (a) one captured fringe image; (b) average intensity; (c) phase distribution; (d) intensity modulation; (e) binarized intensity modulation as a shadow noise mask (using intensity of 5 as a threshold); (f) masked phase distribution without shadow-noised regions.

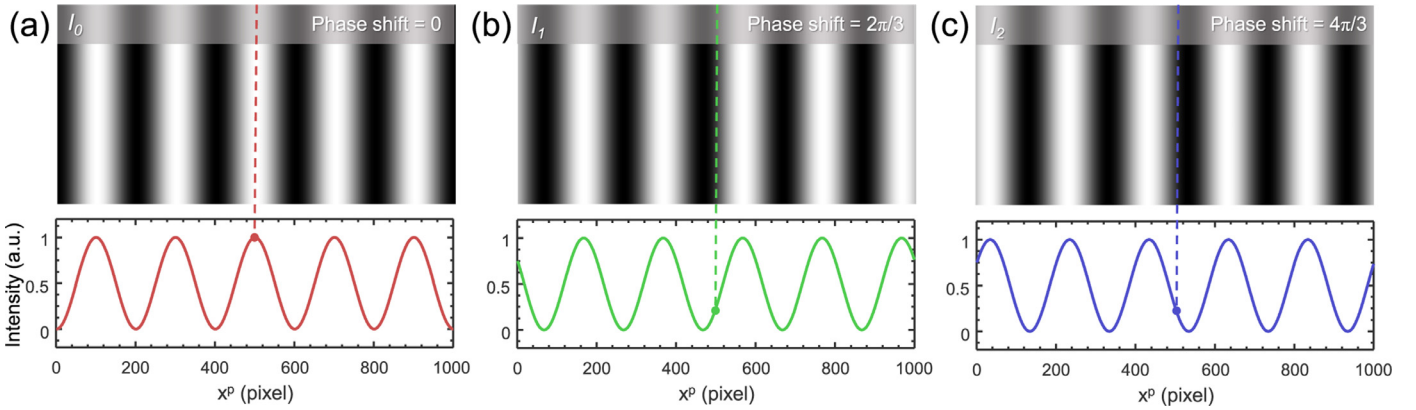


**Fig. 3.** Three-step phase shifting patterns and their corresponding cross sections ( $a^p = b^p = 0.5$ ).

where  $\phi$  is the corresponding wrapped phase which can be extracted by the following equation [54,56,57]:

$$\phi(x, y) = \tan^{-1} \frac{\sum_{n=0}^{N-1} I_n(x, y) \sin(2\pi n/N)}{\sum_{n=0}^{N-1} I_n(x, y) \cos(2\pi n/N)} \quad (8)$$

This is the basic equation for all standard N-step phase shifting techniques. It should be noted that Eq. (8) is just a special case of the least-squares algorithm when phase shifts are equal-spaced over a  $2\pi$  period. In general N-step least-squares algorithm, the phase shifts of the fringe pattern need not to be evenly spaced and can be spread over a range greater than  $2\pi$ . This type of approach is outlined in detail by Greivenkamp [119]. Another important issue is the limited phase range results from the arctan function in Eq. (8). Note that simply applying the arctan function returns values of  $\phi$  only in the range  $-\pi/2$  to  $\pi/2$ , i.e. a total range of  $\pi$ . And the signs of the numerator and denominator can be further used to uniquely define a quadrant for each calculation of  $\phi$ . With the 4-quadrant arctangent, the phase values at each point can be determined modulo  $2\pi$ . It should be mentioned that the phase shifting algorithms discussed in this section focus only on the wrapped phase re-

trieval. Readers should keep in mind that the wrapped phase map  $\phi(x, y)$  contains the modulo  $2\pi$  discontinuity, so phase unwrapping is further required to obtain a continuous or absolute phase map (the PSP algorithms for absolute phase recovery will be discussed in Section 5).

Besides the wrapped phase, the average intensity and intensity modulation can also be demodulated from the phase shifted fringe images according to Eqs. (9) and (10), respectively.

$$A(x, y) = \frac{1}{N} \sum_{n=0}^{N-1} I_n(x, y) \quad (9)$$

$$B(x, y) = \frac{2}{N} \sqrt{\left[ \sum_{n=0}^{N-1} I_n(x, y) \sin(2\pi n/N) \right]^2 + \left[ \sum_{n=0}^{N-1} I_n(x, y) \cos(2\pi n/N) \right]^2} \quad (10)$$

Since the phase reconstruction of phase shifting algorithm is a pixel-wise operation, the coordinate index  $(x, y)$  is removed from our equations henceforth to simplify the notation.

Since there are totally three unknowns  $\phi(x, y)$ ,  $A(x, y)$ , and  $B(x, y)$  in Eq. (7), the minimum number for phase shifting should be 3 in order to

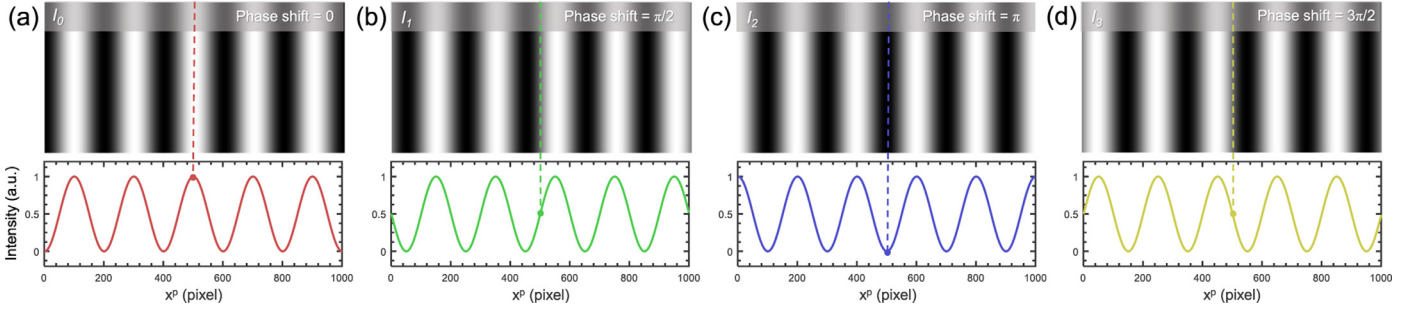


Fig. 4. Four-step phase shifting patterns and their corresponding cross sections.

provide three equations and enable calculation of  $\phi(x, y)$ ,  $A(x, y)$ , and  $B(x, y)$ . Since using the minimum number of fringe images is desirable for reducing the measurement time, the three-step phase shifting algorithm is widely used for real-time or high-speed 3D shape measurement [29,120,121]. As shown in Fig. 3, in three-step phase shifting algorithm, the phase shift  $0$ ,  $2\pi/3$ , and  $4\pi/3$  is used for three fringe images, respectively. The intensities of the three phase-shifted images at each pixel  $(x, y)$  are:

$$I_0 = A + B \cos(\phi) \quad (11)$$

$$I_1 = A + B \cos(\phi - 2\pi/3) \quad (12)$$

$$I_2 = A + B \cos(\phi - 4\pi/3) \quad (13)$$

with the solutions to  $\phi$ ,  $A$ , and  $B$  are given by:

$$\phi = \tan^{-1} \frac{\sqrt{3}(I_1 - I_2)}{2I_0 - I_1 - I_2} \quad (14)$$

$$A = \frac{I_0 + I_1 + I_2}{3} \quad (15)$$

$$B = \frac{1}{3} \sqrt{3(I_1 - I_2)^2 + (2I_0 - I_1 - I_2)^2} \quad (16)$$

The three-step algorithm requires the minimum amount of data and is the simplest to use. However, as will be discussed in Section 4, this algorithm is also sensitive to different types of phase errors. To achieve higher measurement accuracy and better error resistance, four-step phase shifting algorithm is often used. The four-step phase shifting algorithm uses four fringe images with phase shift  $0$ ,  $\pi/2$ ,  $\pi$  and  $3\pi/2$ , as shown in Fig. 4 ( $a^p = b^p = 0.5$ ). The four images acquired can be written as

$$I_0 = A + B \cos(\phi) \quad (17)$$

$$I_1 = A + B \cos(\phi - \pi/2) \quad (18)$$

$$I_2 = A + B \cos(\phi - \pi) \quad (19)$$

$$I_3 = A + B \cos(\phi - 3\pi/2) \quad (20)$$

Using these trigonometric functions,  $\phi$ ,  $A$ , and  $B$  can be calculated as

$$\phi = \tan^{-1} \frac{I_1 - I_3}{I_0 - I_2} \quad (21)$$

$$A = \frac{I_0 + I_1 + I_2 + I_3}{4} \quad (22)$$

$$B = \frac{1}{2} \sqrt{(I_1 - I_3)^2 + (I_0 - I_2)^2} \quad (23)$$

The four-step phase shifting algorithm has a  $90^\circ$  phase shift between adjacent frames and is easier to implement in some situations, making it the most useful algorithm in simultaneous phase shifting systems for PSI [11,83]. In FPP, four-step phase shifting algorithm has also found widespread use for its relatively high measurement accuracy, low pattern count, and good error tolerance. Standard phase shifting algorithm with more than 5 steps are used much less often than 3- and 4-step algorithms due to the need for additional fringe patterns, but they are usually more resistant to some kinds of phase errors. More details about the error analysis of phase shifting algorithms can be found in Section 5.

### 3.2. Double three-step phase shifting algorithm

The conventional three-step algorithm is vulnerable to errors in the PSP system such as phase shifting error, nonlinearity error, and intensity noise. An improvement to the three-step phase shifting algorithm is the double three-step phase shifting algorithm proposed by Huang et al. [90], which can significantly reduce the phase error induced by intensity nonlinearity. It has been proved that a second-order nonlinearity residual in the FPP system can result in an error of  $\Delta\phi$  in the phase map (see Section 5.2 for more detailed discussions about the nonlinearity error)

$$\tan(\Delta\phi) = \tan(\phi' - \phi) = -\frac{\sin(3\phi)}{\cos(3\phi) + m} \quad (24)$$

$$\Delta\phi = \arctan \left[ -\frac{\sin(3\phi)}{\cos(3\phi) + m} \right] \approx \arctan \left[ -\frac{\sin(3\phi)}{m} \right] \quad (25)$$

where  $\phi$  is the ideal phase calculated when the system has perfect linearity.  $\phi'$  is the inaccurate phase retrieved with a traditional three-step algorithm when the fringe intensity has a second-order nonlinearity,  $m$  is a constant that depends on the system linearity, which is usually much larger than 1.

Eq. (25) indicates that the frequency of the phase error is three times that of the original phase. If an initial phase offset is introduced in the phase-shifted fringe patterns, the phase of the error wave will vary correspondingly. When two phase maps are obtained with a relative initial phase difference of  $\pi/3$ , the phase difference between these two inaccurate phases is approximately  $180^\circ$ . Therefore, when the two phases are averaged, the error will be cancelled. This means that we can do phase shifting twice with six fringe patterns with initial phases of  $0$ ,  $2\pi/3$ ,  $4\pi/3$  (group one) and  $\pi/3$ ,  $\pi$ ,  $5\pi/3$  (group two) (see Fig. 5), use the three-step algorithm twice to calculate the two phase maps from each group of fringe patterns, and then average the two phase maps. The intensities of the two groups of three-step phase shifting images for each pixel are

$$I_0 = A + B \cos(\phi) \quad (26)$$

$$I_1 = A + B \cos(\phi - 2\pi/3) \quad (27)$$

$$I_2 = A + B \cos(\phi - 4\pi/3) \quad (28)$$

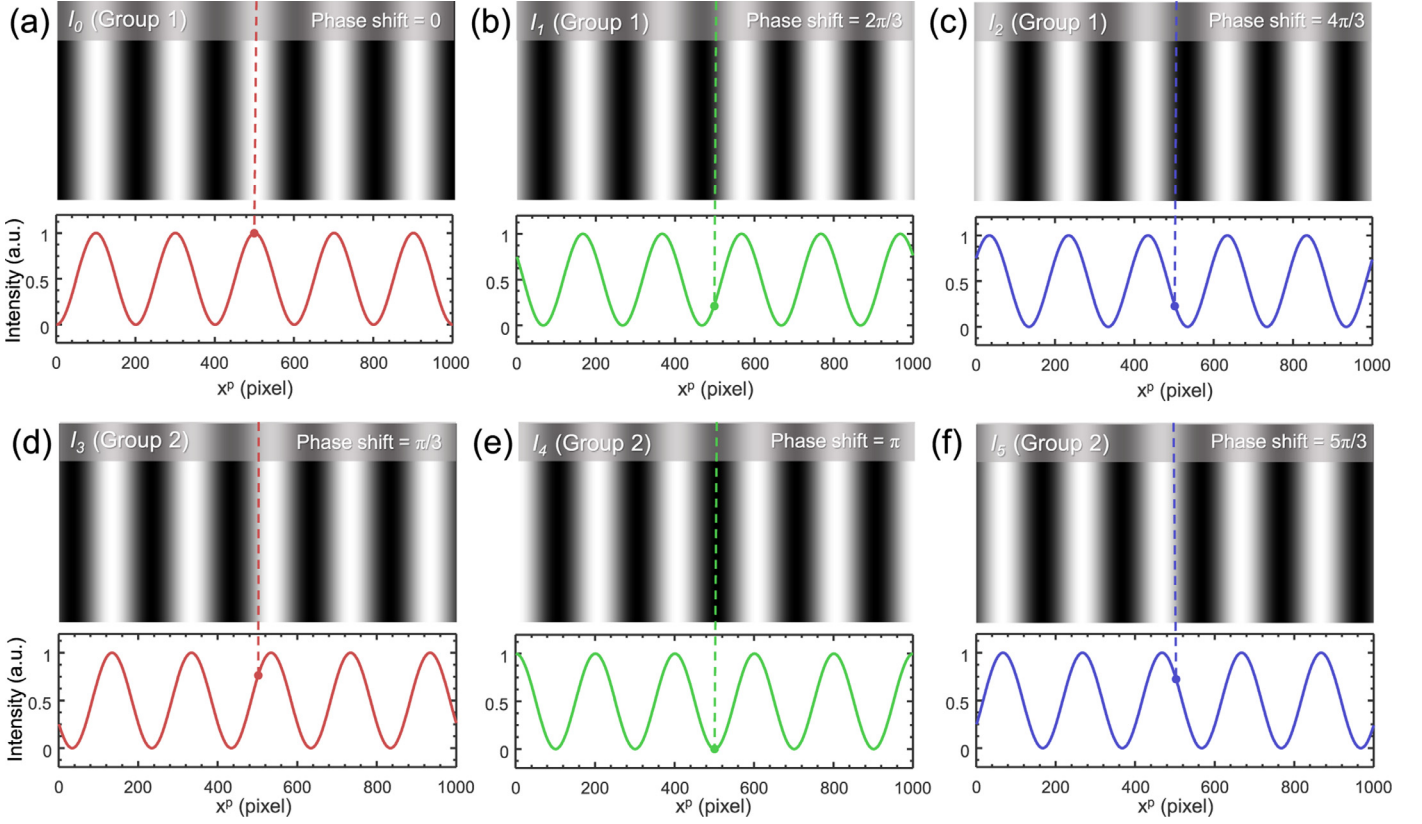


Fig. 5. Double three-step phase shifting patterns and their corresponding cross sections.

$$I_3 = A + B \cos(\phi - \pi/3) \quad (29)$$

$$I_4 = A + B \cos(\phi - \pi) \quad (30)$$

$$I_5 = A + B \cos(\phi - 5\pi/3) \quad (31)$$

The effectiveness of the double three-step algorithm can be verified theoretically. The phase error of the second phase map with an initial phase offset of  $\pi/3$  for the fringe patterns  $I_3 \sim I_5$  can be calculated as

$$\Delta\phi' \approx \arctan \left[ -\frac{\sin[3(\phi + \pi/3)]}{m} \right] = \arctan \left[ \frac{\sin(3\phi)}{m} \right] \quad (32)$$

It is obvious that the sign of the phase error is changed, i.e.  $\Delta\phi = -\Delta\phi'$ . Therefore, if the two obtained phase maps are averaged to generate the final phase map, the second-order nonlinearity error will be effectively removed. Though double three-step phase shifting algorithm can significantly reduce the nonlinearity error, it requires three extra patterns to perform the additional three-step algorithm, thus the acquisition time is doubled compared with conventional three-step algorithm.

### 3.3. Hariharan 5-step phase shifting

The five-step phase shifting algorithm with an unknown but constant phase shift is also called the Hariharan algorithm [57,85], which is designed to be insensitive to phase shift errors. Considering a linear phase shift  $\theta$  between frames, the five fringe images are

$$I_0 = A + B \cos(\phi - 2\theta) \quad (33)$$

$$I_1 = A + B \cos(\phi - \theta) \quad (34)$$

$$I_2 = A + B \cos(\phi) \quad (35)$$

$$I_3 = A + B \cos(\phi + \theta) \quad (36)$$

$$I_4 = A + B \cos(\phi + 2\theta) \quad (37)$$

The five equations are expanded and combined to produce the following relation:

$$\frac{I_1 - I_3}{2I_2 - (I_0 + I_4)} = \left( \frac{\sin \theta}{1 - \cos 2\theta} \right) \tan \phi \quad (38)$$

When the phase shift  $\theta = \pi/2$  (see Fig. 6), the pre-factor  $\left( \frac{\sin \theta}{1 - \cos 2\theta} \right)$  before  $\tan \phi$  has a value of 0.5, then the phase  $\phi$ , average intensity  $A$ , and fringe modulation  $B$  can be calculated as

$$\phi = \tan^{-1} \frac{2(I_1 - I_3)}{2I_2 - (I_0 + I_4)} \quad (39)$$

$$A = \frac{I_0 + I_1 + 2I_2 + I_3 + I_4}{6} \quad (40)$$

$$B = \frac{\sqrt{4(I_1 - I_3)^2 + [2I_2 - (I_0 + I_4)]^2}}{4} \quad (41)$$

It has been also found that  $\left( \frac{\sin \theta}{1 - \cos 2\theta} \right)$  does not depart from 0.5 for small deviations in  $\theta$  from  $\pi/2$ . If  $\theta$  falls between  $86^\circ$  and  $94^\circ$ , then the value of this phase pre-factor does not alter by more than 0.001, as illustrated in Fig. 7. As a result, when the phase shift  $\theta = \pi/2$ , Hariharan 5-step phase shifting algorithm can tolerate fairly large errors in the phase shift.

### 3.4. Modified 2 + 1 phase shifting algorithm

The modified 2 + 1 phase shifting algorithm was proposed by Zhang and Yau [100] in order to alleviate the problem of motion artifacts when measuring moving or shape-changing object. It requires two fringe images with a relative phase shift of  $\pi/2$ , together with a third uniform

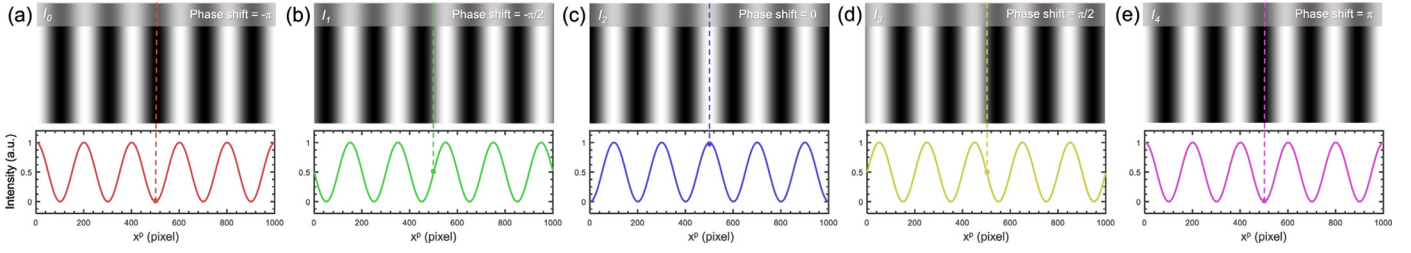


Fig. 6. Hariharan 5-step phase shifting patterns and their corresponding cross sections ( $\theta = \pi/2$ ).

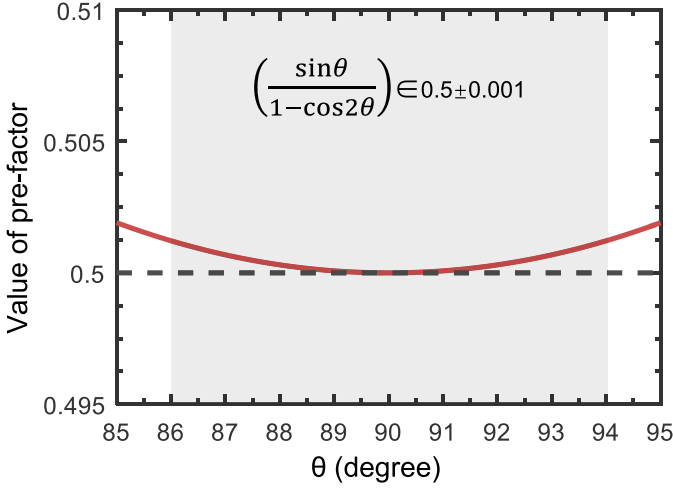


Fig. 7. Variation of the phase pre-factor with  $\theta$  when  $\theta$  is between  $85^\circ$  and  $95^\circ$ . In the shaded region, the value of the pre-factor does not alter by 0.001.

flat image to retrieve the phase information. In the projector space, the three projected patterns are

$$I_0^p(x^p, y^p) = a^p \quad (42)$$

$$I_1^p(x^p, y^p) = a^p + b^p \cos(2\pi f_0^p x^p) \quad (43)$$

$$I_2^p(x^p, y^p) = a^p + b^p \cos(2\pi f_0^p x^p - \pi/2) = a^p + b^p \sin(2\pi f_0^p x^p) \quad (44)$$

Fig. 8 shows modified 2+1 phase shifting patterns with  $f_0^p = 5$ ,  $a^p = b^p = 0.5$ . The intensities of the three images captured by the camera are

$$I_0 = A \quad (45)$$

$$I_1 = A + B \cos(\phi) \quad (46)$$

$$I_2 = A + B \sin(\phi) \quad (47)$$

It can be seen that the average intensity  $A$  is directly given by  $I_0$ . The solutions to  $\phi$  and  $B$  are given by:

$$\phi = \tan^{-1} \frac{I_2 - I_0}{I_1 - I_0} \quad (48)$$

$$B = \sqrt{(I_2 - I_0)^2 + (I_1 - I_0)^2} \quad (49)$$

Since the phase information is only encoded by two fringe images and the flat image is less sensitive to object motion between successive frames, the modified 2 + 1 phase shifting algorithm can reduce the motion-induced measurement error compared to conventional 3-step phase shifting algorithm. However, due to the small number of fringes used, the modified 2 + 1 phase shifting algorithm is more susceptible

to errors resulting from the noise and intensity nonlinearity. It should also be mentioned that the modified 2 + 1 phase shifting algorithm is actually an improved version of 2 + 1 phase shifting method originally developed in the field of PSI, in which the flat image is collected by averaging two interferograms with a  $\pi$  phase shift [122,123].

### 3.5. Trapezoidal phase shifting

The trapezoidal phase shifting proposed by Huang et al. [94] is very similar to the three-step sinusoidal phase shifting method, only that the cross-sectional shape of the patterns has been changed from sinusoidal to trapezoidal. Besides, it uses the intensity-ratio directly rather than the phase, so it is less expensive to compute since it does not use the arctangent function as in conventional phase shifting algorithm. To reconstruct the 3D shape of the object, three trapezoidal patterns, which are phase shifted by  $2\pi/3$  or one-third of the pitch, are needed, as shown in Fig. 9. For each point of captured images, the intensity ratio map  $Q$  is obtained by using the following equation:

$$Q = 2 \text{Round} \left( \frac{K-1}{2} \right) + (-1)^{K+1} \frac{I_{med} - I_{min}}{I_{max} - I_{min}} \quad (50)$$

where  $I_{max}$ ,  $I_{med}$  and  $I_{min}$  are respectively the maximum, median and minimum intensities of the three captured images, and  $K = 1, 2, 3, \dots, 6$  is the region number determined by comparing the three intensities [94]. The value of  $Q$  ranges from 0 to 6. It can then be converted to the same range of  $[-\pi, \pi)$  of the wrapped phase map

$$\phi = \frac{\pi(Q-3)}{3} \quad (51)$$

so that the subsequent processing can be compatible with conventional PSP techniques. Besides, the trapezoidal phase shifting patterns can also be repeated to create high-frequency periodical patterns, as the case of the sinusoidal patterns shown before. In such cases, the periodical nature of the pattern introduces the ambiguity problem, which needs to be further addressed by phase unwrapping. Besides, some transition regions of trapezoidal patterns are very sharp, making the trapezoidal phase shifting method sensitive to the intensity blur effect induced by lens defocusing (discussed in Section 4.3).

### 3.6. Triangular phase shifting

The triangular phase shifting algorithm proposed by Jia et al. [99] has the advantage of requiring only a minimum of two rather than three patterns to reconstruct the 3D shape of the object, as shown in Fig. 10. It also uses the intensity-ratio rather than the phase. After capturing the patterns from camera, the intensity ratio map  $Q$  is obtained as

$$Q = 2 \text{Round} \left( \frac{K-1}{2} \right) + (-1)^{K+1} \frac{|I_0 - I_1|}{I_m^p} \quad (52)$$

where  $K = 1, 2, 3, 4$  is the region number determined by analyzing a small neighborhood of each point [99]. The value of  $Q$  ranges from 0 to 4, and can be converted to the same range of  $[-\pi, \pi)$  as in conventional phase shifting techniques

$$\phi = \frac{\pi(Q-2)}{2} \quad (53)$$

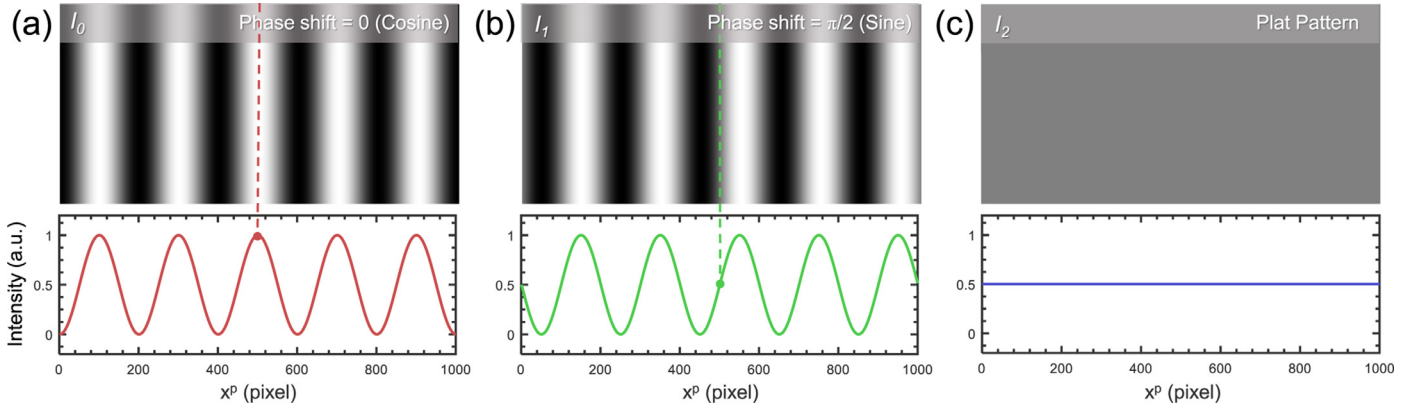


Fig. 8. Modified 2+1 phase shifting patterns and their corresponding cross sections.

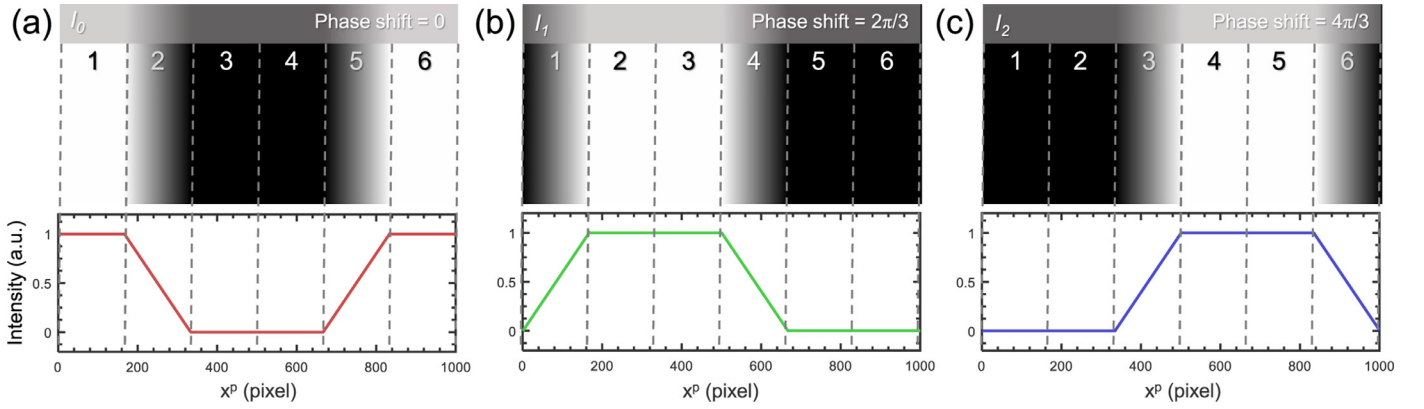


Fig. 9. Trapezoidal phase shifting patterns (single period) and their corresponding cross sections.

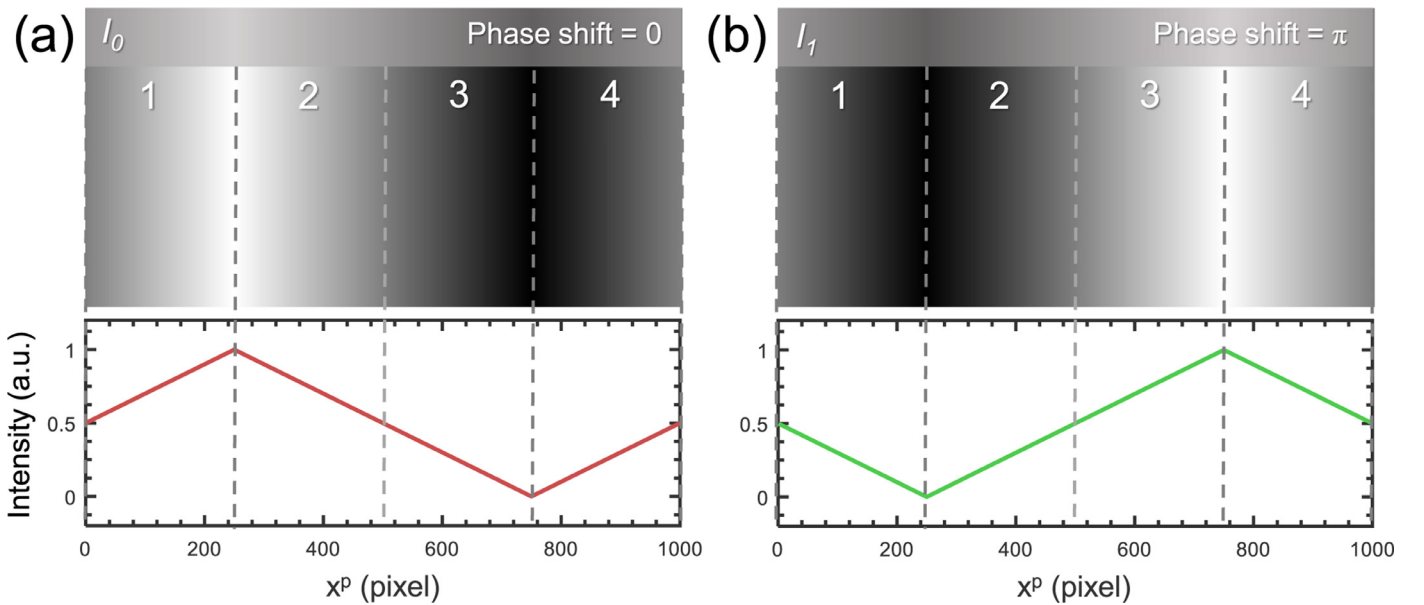


Fig. 10. Triangular phase shifting patterns (single period) and their corresponding cross sections.

$I_m^p$  is so-called the intensity modulation, which is computed as

$$I_m^p = 2b^p = I_{max}^p - I_{min}^p \quad (54)$$

where  $I_{max}^p$  and  $I_{min}^p$  are respectively the maximum and minimum intensities of the projected patterns. It should be mentioned that  $I_m^p$  is not the real intensity modulation since it is calculated from the projected patterns, instead of captured images. Thus, the effect of surface reflectivity

of the measured object cannot be cancelled out in Eq. (52) ( $|I_0 - I_1|$  contains the information of surface reflectivity [see Eqs. (3)–(5)] but  $I_m^p$  does not), making the triangular phase shifting algorithm sensitive to the reflectivity of the measured object. In order to make the triangular phase shifting algorithm perform better in the presence of non-uniform surface reflectivity, at least one more pattern should be projected [124].

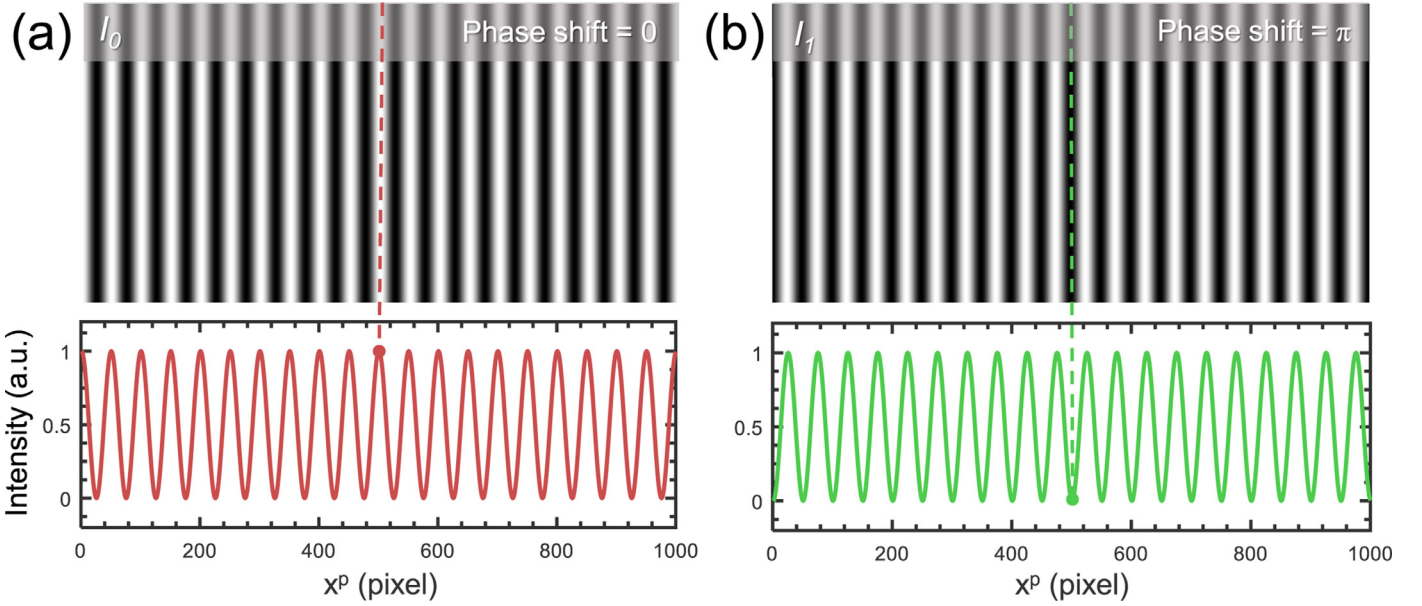


Fig. 11.  $\pi$ -shift Fourier transform patterns and their corresponding cross sections.

Note that usually the triangular pattern needs also be periodically extended to increase the measurement accuracy, and phase unwrapping is needed to remove the discontinuity in the wrapped intensity ratio map. Besides, similar to trapezoidal phase shifting method, the sharp transition points also make triangular phase shifting method sensitive to image blur.

### 3.7. $\pi$ -shift Fourier transform profilometry

The phase shifting techniques can also be combined with FTP to obtain improved accuracy and extended measurement range. In conventional FTP, usually a high-frequency fringe pattern is projected onto the object surface, and the captured intensity  $I(x, y)$  is commonly expressed as [49,125,126]

$$I(x, y) = A(x, y) + B(x, y) \cos[\phi(x, y)] = A(x, y) + B(x, y) \cos[2\pi f_0 x + \phi_0(x, y)] \quad (55)$$

To simplify explanations, here we explicitly represent the phase of the fringe pattern as a sum of independent two components: the object component  $\phi_0(x, y)$  and the linear carrier component  $2\pi f_0 x$ , where  $f_0$  is the carrier frequency of the captured fringe image. Expanding the cosine function in Eq. (55) using Euler's formula, and introducing the definition

$$C(x, y) = \frac{1}{2} B(x, y) \exp\{i\phi(x, y)\} = \frac{1}{2} B(x, y) \exp\{i\phi_0(x, y)\} \exp\{i2\pi f_0 x\} \quad (56)$$

gives

$$I(x, y) = A(x, y) + C(x, y) + C^*(x, y) \quad (57)$$

where \* denotes the complex conjugate. Applying the 2D Fourier transform to  $I(x, y)$  gives

$$\hat{I}(f_x, f_y) = \hat{A}(f_x, f_y) + \hat{C}(f_x, f_y) + \hat{C}^*(f_x, f_y) \quad (58)$$

where  $(f_x, f_y)$  is the vector in spatial frequency domain corresponding to  $(x, y)$ .  $\hat{A}(f_x, f_y)$  and  $\hat{C}(f_x, f_y)$  are the Fourier transforms of  $A(x, y)$  and  $C(x, y)$ , respectively. Fourier shift theorem indicates that multiplying the carrier phase factor  $\exp(\pm i2\pi f_0 x)$  in spatial domain is equivalent to a shift of the signal spectrum by  $\mp f_0$  in the frequency domain. Therefore, in conventional FTP,  $\phi$ ,  $A$ , and  $B$  are assumed to be slowly varying compared to the carrier frequency  $f_0$  such that the zero order ( $\hat{A}(f_x, f_y)$ ) can be well separated with the +1 order ( $\hat{C}(f_x, f_y)$ ) and -1 order ( $\hat{C}^*(f_x, f_y)$ )

in the frequency domain. Then a properly designed band-pass filter can be applied to extracting the +1 order ( $\hat{C}(f_x, f_y)$ ), and the phase can be retrieved by taking the angle part of the resultant inverse Fourier transform.

$$\phi(x, y) = \tan^{-1} \left[ \frac{\text{Re}\{C(x, y)\}}{\text{Im}\{C(x, y)\}} \right] \quad (59)$$

However, when the measured surface contains sharp edges, discontinuities, or large surface reflectivity variations, the support of the three terms in Eq. (58) will be significantly extended, so that the zero frequency may overlap with the +1 and -1 orders [28,49]. The spectrum overlapping makes it difficult to filter out the +1 order ( $\hat{C}(f_x - f_0, f_y)$ ), precluding high-accuracy phase reconstruction of complex objects. To address this problem, Li and Su [86] proposed the  $\pi$ -shift FTP to effectively suppress the zero order by projecting an additional  $\pi$ -shift sinusoidal fringe image. In the projector space, the two projected patterns are (see Fig. 11)

$$I_0^p(x^p, y^p) = a^p + b^p \cos(2\pi f_0^p x^p) \quad (60)$$

$$I_1^p(x^p, y^p) = a^p + b^p \cos(2\pi f_0^p x^p + \pi) = a^p - b^p \cos(2\pi f_0^p x^p) \quad (61)$$

The intensities of the two images captured are

$$I_0(x, y) = A(x, y) + B(x, y) \cos[2\pi f_0 x + \phi_0(x, y)] \quad (62)$$

$$I_1(x, y) = A(x, y) - B(x, y) \cos[(2\pi f_0 x + \phi_0(x, y))] \quad (63)$$

By taking the difference between  $I_0$  and  $I_1$ , the fundamental frequency information is doubled with the zero-frequency term being effectively cancelled:

$$I_d(x, y) = I_0 - I_1 = 2B(x, y) \cos[2\pi f_0 x + \phi_0(x, y)] \quad (64)$$

Then Fourier transform is applied to  $I_d$  to extract the phase information. In this way, the fundamental spectrum modulated by the object height distribution can theoretically be extended from 0 to  $2f_0$ , without overlapping the zero or higher frequency components. Consequently, the maximum measurable slope of height variation can be extended to nearly three times that of the conventional FTP [86].

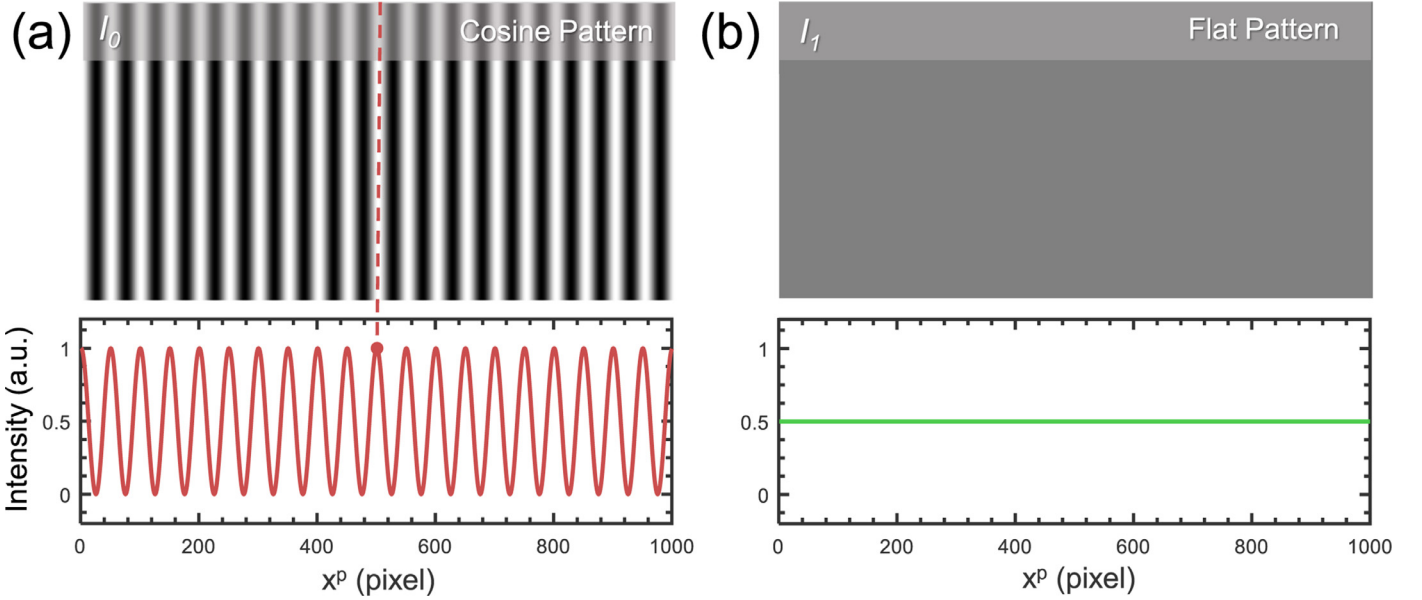


Fig. 12. Modified Fourier transform patterns and their corresponding cross sections.

### 3.8. Modified Fourier transform profilometry

Similar to  $\pi$ -shift FTP, the modified FTP approach proposed by Guo and Huang [127] aims to reduce the impact of the zero-order term by projecting an additional flat pattern, which is similar to the one used in the modified 2+1 PSP approach. In the projector space, the two projected patterns are (see Fig. 12)

$$I_0^p(x^p, y^p) = a^p + b^p \cos(2\pi f_0^p x^p) \quad (65)$$

$$I_1^p(x^p, y^p) = a^p \quad (66)$$

The intensities of the two images captured are

$$I_0(x, y) = A(x, y) + B(x, y) \cos[2\pi f_0 x + \phi_0(x, y)] \quad (67)$$

$$I_1(x, y) = A(x, y) \quad (68)$$

It can be seen that the average intensity  $A$  is directly given by  $I_1$ . By taking the difference between  $I_0$  and  $I_1$ , the zero-frequency term can also be effectively removed:

$$I_d(x, y) = I_0 - I_1 = B(x, y) \cos[2\pi f_0 x + \phi_0(x, y)] \quad (69)$$

Then the phase can be extracted from  $I_d$  based on 2D Fourier transform. Similar to  $\pi$ -shift FTP, the subtraction procedure removes the effect of the 0-order term and thus the fundamental frequency term can be selected more easily from the resultant spectrum. This allows to significantly increase the maximum measurable range and the measurement accuracy. Besides, only a single fringe image is used to encode the phase value in the modified FTP, making it rather insensitive to the motion of the scanned object. However, in  $\pi$ -shift FTP the phase information is encoded in two fringes, and thus it is much more sensitive to object motion.

### 3.9. Background-normalized Fourier transform profilometry

Though the effect of zero order can be largely removed in  $\pi$ -shift FTP and modified FTP, neither approach can handle large surface reflectivity variations, which also introduce spectrum leakage and thus influence the high-quality phase retrieval. To address this issue, the background-normalized FTP was proposed by Zuo et al. [128], which introduces an additional normalization step to modified FTP to alleviate the effect of

the surface reflectivity variations. The two projected patterns are the same as those in the modified FTP, which are a high frequency fringe and an additional flat pattern, respectively:

$$I_0^p(x^p, y^p) = a^p + b^p \cos(2\pi f_0^p x^p) \quad (70)$$

$$I_1^p(x^p, y^p) = a^p \quad (71)$$

The corresponding intensities of the images captured are

$$I_0(x, y) = A(x, y) + B(x, y) \cos[2\pi f_0 x + \phi_0(x, y)] \quad (72)$$

$$I_1(x, y) = A(x, y) \quad (73)$$

The term used for the Fourier transform is the normalized difference between  $I_0$  and  $I_1$ :

$$I_d(x, y) = \frac{I_0 - I_1}{I_1 + \gamma} = \frac{B(x, y)}{A(x, y)} \cos[2\pi f_0 x + \phi_0(x, y)] \quad (74)$$

where  $\gamma$  is a small constant to prevent divide-by-zero error. The rationale for the background-normalized FTP approach lies in the fact that when the ambient light [ $\beta_1$  and  $\beta_2$  in Eq. (4)] is weak compared to the projector light, the average intensity can be simplified as

$$A(x, y) = \alpha(x, y)[a^p + \beta_1(x, y)] + \beta_2(x, y) \approx \alpha(x, y)a^p \quad (75)$$

which is almost proportional to the intensity modulation

$$B(x, y) = \alpha(x, y)b^p \quad (76)$$

So the effect of surface reflectivity  $\alpha(x, y)$  can be cancelled in the normalization step (Eq. (74)),

$$I_d(x, y) = \frac{I_0 - I_1}{I_1 + \gamma} = \frac{B(x, y)}{A(x, y)} \cos[2\pi f_0 x + \phi_0(x, y)] \approx \frac{b^p}{a^p} \cos[2\pi f_0 x + \phi_0(x, y)] \quad (77)$$

With the effect of zero-order as well as surface reflectivity variations removed before the Fourier transform, the spectrum overlap in the frequency domain can be prevented or significantly alleviated. It should be noted that the original version of the background-normalized FTP is specially designed for high-speed 3D measurement with binary patterns, and the additional flat pattern has all values of '1' instead of '0.5' (see Fig. 13) [128]. This is because the mid-value 0.5 is not able to be

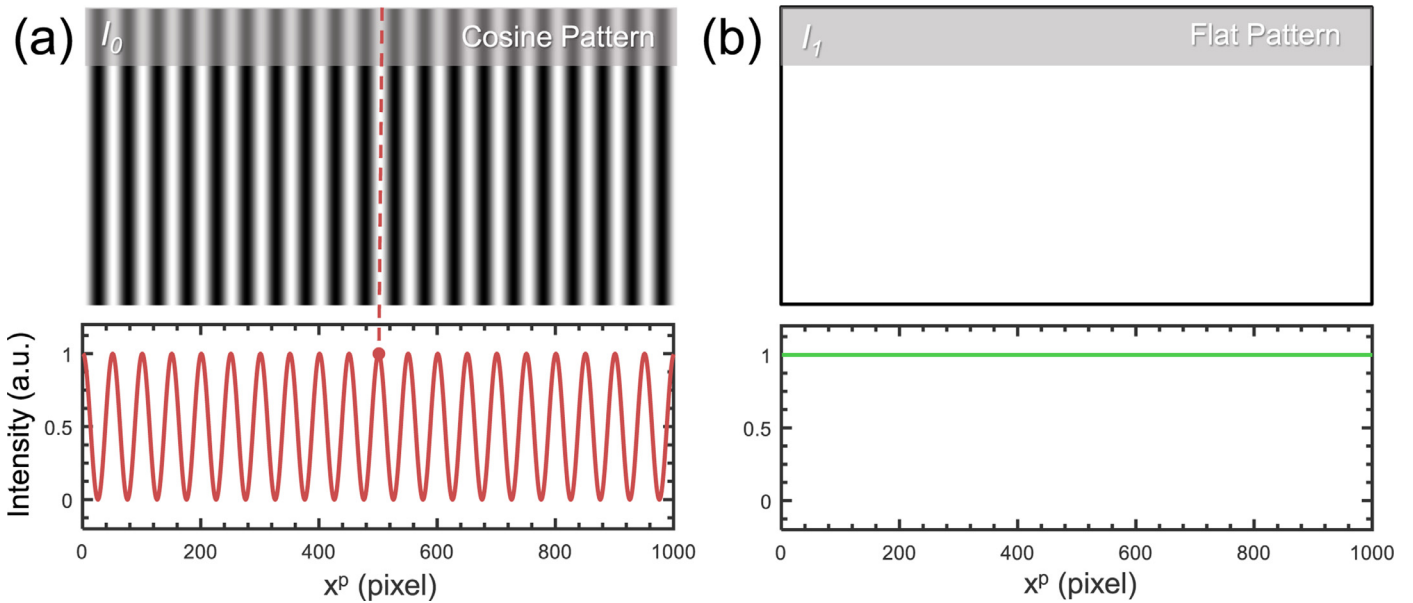


Fig. 13. Background-normalized FTP patterns and their corresponding cross sections.

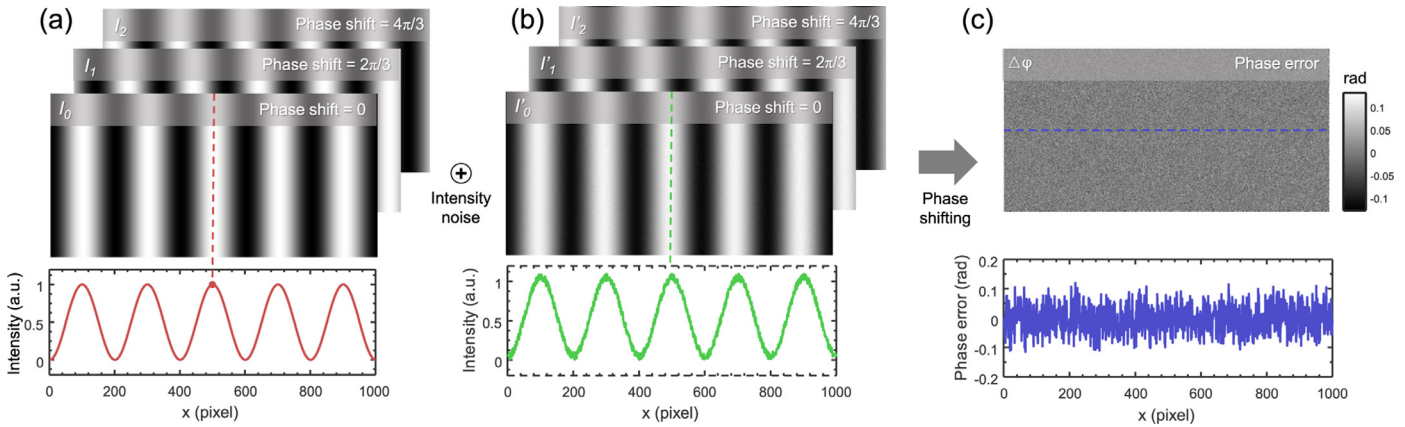


Fig. 14. Effect of intensity noise on the phase reconstruction. (a) Noise-free three-step phase shifting patterns and the corresponding cross section; (b) three-step phase shifting patterns contaminated by intensity noise; (c) resultant phase reconstruction error.

perfectly generated by the DMD operating in binary (1-bit) mode. Besides, strictly speaking, the modified FTP and the BNFTP do not belong to phase shifting techniques. However, since their principles and basic ideas are quite similar to the  $\pi$ -shift FTP, they have been also included in our review.

#### 4. Error analysis and compensation for PSP

In a typical FPP system based on PSP, there are eight major causes of phase error have been recognized: intensity noise, nonlinearity error, lens defocusing, phase shifting error, motion-induced error, detector saturation, illumination fluctuations, and imbalance error in color fringe projection. This section reviews and discusses the behaviors, the impact on the retrieved phase, and corresponding solutions of these error sources.

##### 4.1. Intensity noise

In a practical FPP system, the intensity of the fringe pattern at each point of the object is sampled by a digital camera and inevitably contaminated by intensity noise. The intensity noise sources include unstable ambient light, projector illumination noise, camera/projector flicker,

camera noise, and quantization error in the frame grabber and the projector. As illustrated in Fig. 14, when the captured fringe images suffer from the intensity noise, the phase reconstructed by standard phase shifting formula will deviate from the ideal values, resulting in phase reconstruction errors.

Many studies have been performed to understand the effects of intensity noise on the resulting phase reconstruction, and several noise models have been developed to quantitatively analyze the noise-induced phase error in PSP. Earlier work focused more on the effect of noisy interferograms over the estimated phase in the field of PSI [107,129–133]. For example, Surrel [130] investigated the effect of additive noise in digital phase detection based on characteristic polynomials. He defined a loss factor, which describes how the intensity SNR will influence phase quality in a given phase shifting algorithm. Rathjen [129] studied statistical properties of different phase shifting algorithms for the case of additive Gaussian intensity noise based on an intuitive vector representation. These ideas and noise models have later been adapted to the field of PSP. Li et al. [131] proposed an additive white-noise model for PSP and then applied this model to optimize a two-frequency PSP algorithm. Wang et al. [133] extended the Rathjen’s vector representation to study the noise effect in PSP, and optimized PSP patterns in order to maximize their SNR. Though these models are derived based on different

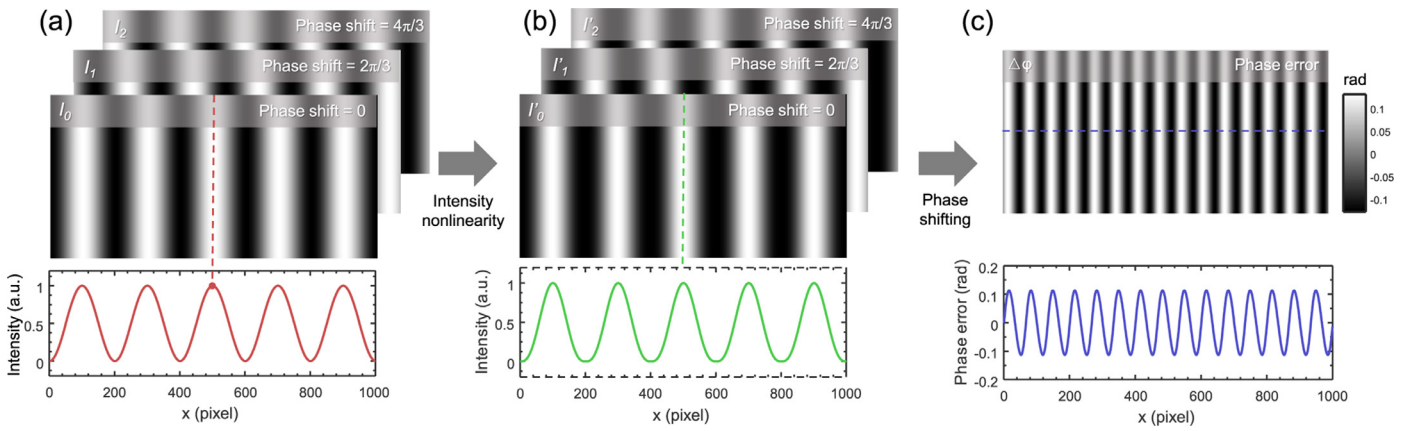


**Fig. 15.** Effect of intensity nonlinearity on the phase reconstruction. (a) Noise-free three-step phase shifting patterns and the corresponding cross section; (b) three-step phase shifting patterns distorted by intensity nonlinearity ( $\gamma = 1.4$ ) and the corresponding cross section; (c) resultant phase reconstruction error.

considerations from various perspectives, the final conclusions they arrived at are quite similar: the variance in the phase error depends primarily on the noise variance, intensity modulation, and the fringe density/frequency. Assuming that the intensity noise is additive, white, Gaussian distributed variable with zero-mean and a standard derivation of  $\sigma_n$ , the standard deviation of phase error of the standard N-step PSP approach is defined as [82,131,133]

$$\sigma_\phi = \sqrt{\frac{2}{N}} \frac{\sigma_n}{B} \quad (78)$$

where  $\sigma_\phi$  is the standard deviation of phase error,  $N$  is the number of phase shifting steps,  $B$  is the intensity modulation. Furthermore, if the phase is unwrapped, the phase unambiguous range can be extended from  $2\pi$  to  $2\pi F$ , where  $F$  is the total number of periods in the fringe pattern. In other words, when the final absolute phase is scaled into the same dynamic range  $[-\pi, \pi]$ , the phase error can be further reduced by a factor of  $F$

$$\sigma_\phi = \sqrt{\frac{2}{N}} \frac{\sigma_n}{BF} \quad (79)$$

According to Eq. (79), typically there are three factors can be considered to suppress noise in the phase reconstruction of PSP. The first one is to increase the number of phase shifting steps ( $N$ ), which will prolong the pattern sequence and increase the measurement time accordingly. The second factor is to improve the intensity modulation  $B$  versus the noise standard derivation  $\sigma_n$ , and the intensity modulation is known to be directly proportional to the surface reflectivity  $\alpha$  and pattern amplitude strength  $b^p$  [see Eq. (5)]. Therefore, for a given measured object and a fixed FPP system, increasing the pattern amplitude  $b^p$  will reduce the error in phase measurement. Besides using the largest possible dynamic range of the projector  $[0, 1]$  for fringe projection ( $a^p = b^p = 0.5$ ), the effective fringe amplitude can also be further improved by carefully optimizing or modifying the standard phase shifting patterns. It has been demonstrated that the trapezoidal pattern [94], edge pattern [133], and third harmonic injected pattern [134] can further provide an improved SNR (by a factor of 15.5–23.6%) compared with conventional (full dynamic range) 3-step PSP patterns due to their higher effective fringe amplitude or contrast. The last factor is to use patterns with higher fringe frequency, i.e., increase  $F$ . Compared with increasing  $N$  or  $B$ , increasing  $F$  will more efficiently reduce  $\sigma_\phi$ . For example, when 10-period fringe patterns are used for phase reconstruction, the standard deviation of phase error will be 10 times smaller than that obtained by using unit-frequency patterns. However, using high-frequency patterns also introduces phase ambiguities in the reconstruction process that need to be addressed by means of phase unwrapping, which will be discussed in detail in Section 5.

#### 4.2. Nonlinearity error in the camera/projector

The second source of error in PSP is due to the nonlinear response in both the camera and the projector. Most industrial digital cameras have very good linearity unless the camera gain is set too high. However, for presentation and home theater digital projectors, the default gamma setting is usually nonlinear because it is set for the nonlinear sensitivity of human vision to intensity. The nonlinear mapping of the projector input to captured image intensity causes distortions of the fringe profiles, which in turn lead to errors in the retrieved phase map, as illustrated in Fig. 15.

For normal phase shifting techniques examined, it is assumed that the projector has a linear response, i.e., the digitized level of fringe intensity  $I^p$  is linearly related to the actual intensity  $I^{real}$

$$I^p = k_0 + k_1 I^{real} \quad (80)$$

where  $k_0$  and  $k_1$  are constants. However, for most off-the-shelf projectors, this may not be true, and the intensity response function of the projector  $f$  may be a nonlinear function

$$I^p = f(I^{real}) \quad (81)$$

There are many models to characterize the response function of the projector. The simplest one is the one-parameter gamma function [135–137], which describes the relationship between input  $I^{real}$  and output  $I^p$  with a gamma  $\gamma$  parameter according to

$$I^p = (I^{real})^\gamma \quad (82)$$

Alternatively, a polynomial function can be used to represent the nonlinear curve [109,120] such as

$$I^p = k_0 + k_1(I^{real}) + k_2(I^{real})^2 + k_3(I^{real})^3 + \dots \quad (83)$$

The majority of state-of-the-art research focused on calibrating the nonlinear response of a FPP system or compensating for the associated error, which can be broadly classified into two categories [135]: active methods (correction before pattern projection) and passive methods (correction after pattern projection). The active method calibrates the response function of the projector and modifies fringe patterns before their projection to ensure sinusoidality. Generally, no matter what kind of model is used (e.g. gamma function [136–138], polynomial [109,120], and constrained cubic spline [139]), the projector response function  $f$  is a monotonically increasing function of the input gray-scale, which means there always exists an inverse function  $f^{-1}$  for  $f$ . Once  $f$  is determined prior to measurement, the corresponding inverse function  $f^{-1}$  can be applied to the gray levels before input to the projector by pre-distorting the projected pattern using the inverse function  $f^{-1}$  to counteract the nonlinearity effect [109,120,137,139,140]. The whole compensation process is demonstrated in Fig. 16.

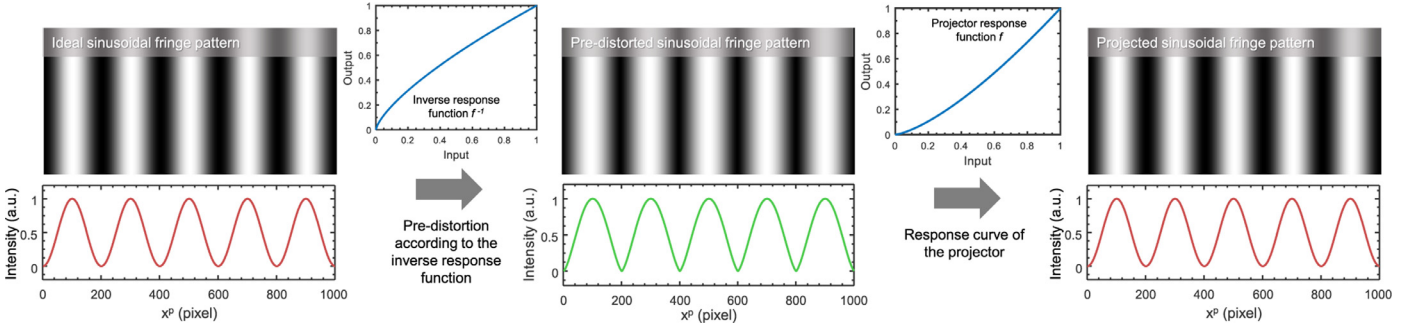


Fig. 16. Nonlinearity compensation process by pre-distorting (correcting) the projected pattern using the inverse response function.

Though the basic ideal behind the compensation process is simple and straightforward, the accurate measurement of the intensity response function  $f$  requires that the input–output relation of the projector  $I^p = f(I^{real})$  can be precisely obtained. Usually a white plane is set and illuminated by the projector with serial predefined uniform intensities (e.g. from 0 to 255 for an 8-bit projector), and the corresponding intensities reflected by the plane are recorded. Based on the captured images, the intensity response function of the overall system is fitted, or the gamma value is estimated [120,140]. Since the image finally captured by the camera is:

$$I_i(x, y) = \alpha(x, y)\{f[I_i^{real}(x, y)] + \beta_1(x, y)\} + \beta_2(x, y) \quad i = 0, 1, 2, \dots, 255 \quad (84)$$

which contains contributions from both the ambient light  $[\beta_1(x, y), \beta_2(x, y)]$  as well as the surface reflectivity  $[\alpha(x, y)]$ . Therefore, the normalized intensity  $\bar{I}_i(x, y)$  should be used to establish the response curves of the projector [109,120,137]

$$\bar{I}_i(x, y) = 255 \times \frac{I_i(x, y) - I_0(x, y)}{I_{255}(x, y) - I_0(x, y)} \quad (85)$$

In Eq. (85), the subtraction unconditionally removes any background offset while the division normalizes the pattern to remove the reflectivity variations across the surface. Besides, since for most commercial video projectors, the response curves of all pixels are identical (no nonuniformity in the projector), the normalized intensity  $\bar{I}_i(x, y)$  can be averaged across the image to further reduce the effect of noise. Rather than calibrating the response function using normal least-square fitting based on uniform gray level patterns, there are also some ‘self-calibration’ methods extracting the nonlinear parameters based on gamma-distorted fringe images directly. Baker et al. [141] exploited the generalization and interpolation capabilities of a feed-forward back propagation neural network to model the intensity response function and map from distorted fringe to nondistorted one. Guo et al. [136] employed the normalized cumulative histogram of the fringe images to estimate the gamma value. The theoretical foundation is that the cumulative distribution functions of sinusoidal signals homologically have fixed forms independent of their phases and frequencies. Liu et al. [138] developed a mathematical model for predicting the effects of gamma distortion on standard PSP. The gamma value is estimated from the harmonic intensity modulation coefficients of PSP with a large number of phase-shifted patterns. Li et al. [142] further incorporated the projector defocus into Liu’s model [138] and determined the level of defocusing by using two preset gamma values. Hoang et al. [143] determined the gamma value through solving the nonlinear function of the ideal phase and the distorted phase, and the ideal phase was determined by phase shifting with a large number of steps. Lü et al. [144] developed a self-correcting method that directly estimates the projector nonlinearity curve from the fringe patterns when measuring an object. The polynomial coefficients are determined by fitting the curve of the normalized fringe intensities against the cosine values of the smoothed phases.

Table 1

Non-linearity phase error for conventional N-step algorithm

Order of Nonlinearity	Phase error $\Delta\phi(x, y)$		
	3-step PSP	4-step PSP	5-step PSP
Linear term $k_0 + k_1 I$	0	0	0
2 <sup>nd</sup> nonlinearity $k_2 I^2$	$-\frac{Bk_2}{2} \sin[3\phi(x, y)]$	0	0
3 <sup>rd</sup> nonlinearity $k_3 I^3$	$-\frac{ABk_3}{2} \sin[3\phi(x, y)]$	$-\frac{Bk_3}{4} \sin[4\phi(x, y)]$	0

Besides the one-parameter gamma model and the polynomial model, actual nonsinusoidal waveforms can also be approximated as an ideal sinusoidal function distorted by high-order harmonics. Specifically, based on the Fourier series expansion, the nonsinusoidal waveform can be represented as

$$I^p(x^p, y^p) = a^p + \sum_{k=1}^{\infty} b_k^p \cos[k(2\pi f_0^p x^p - 2\pi n/N)] \quad (86)$$

where the high order harmonics ( $k > 1$ ) make the waveform deviate from the ideal sinusoidal function. Instead of calibrating the response function and modifying fringe patterns before projection, some other active methods employ the lens defocusing effect as a low-pass filter to suppress the unwanted high-order harmonics in the waveforms to make them become more sinusoidal. For example, Su et al. [145] and Lei and Zhang [146] generated quasi-sinusoidal fringe patterns by defocusing binary fringe patterns. Baker et al. [141] followed this technique to defocus the gamma distorted fringes instead of binary waveforms. These defocus-based approaches are simple to implement and require no additional computation for calibration or compensation, but the improvement is at the cost of reducing the fringe contrast and diminishing the SNR. Alternatively, the high-order harmonics can also be attenuated by blurring the captured fringe image [147]. The blur effect is similar to the defocus, but the high-frequency detail of object surface may also be diminished.

The passive method, in contrast, does not modify the projector’s input fringe patterns, but compensates the phase error by using some post-processing algorithms after nonlinear fringe patterns are captured. In fact, standard N-step phase shifting algorithms have certain resistance to the nonlinearity error inherently. Wingerden et al. [148] analyzed the impact of nonlinearities on various phase shifting algorithms based on the polynomial model [Eq. (82)]. And it has been found that the 3-step phase shifting algorithm is sensitive to all higher order ( $\geq 2$ ) errors, the 4-step phase shifting algorithm is insensitive to the 2nd order error, and the 5-step phase shifting algorithm is insensitive to both the 2nd and 3rd order errors, as summarized in Table 1.

Stetson and Brohinski [149] analyzed various algorithms and nonlinearities based on Fourier series expansion model [Eq. (86)], and their results are summarized in Table 2. The  $\times$  indicates that the nonlinearity affects the phase calculation, the blank indicates that the effect of the nonlinearity is automatically cancelled in the phase calculation. Surrel [150] analyzed different phase shifting algorithms with characteristic

**Table 2**  
Sensitivity of different phase shifting algorithms to high order harmonics.

Number of Step	Harmonics																	
	2	3	4	5	6	7	8	9	10	11	12	13	14	15	16	17	18	
3	×		×	×		×	×		×	×		×	×		×	×		
4		×		×		×		×		×		×		×		×		
5			×		×			×			×		×			×		
6				×		×				×		×				×		
7					×		×				×		×			×		
8						×		×		×			×		×		×	
9							×		×		×			×			×	

polynomials and obtain a more generalized result:  $N$ -step phase shifting is only sensitive to the presence of the  $(p + 1)N \pm 1$ th harmonics, where  $p$  is an integer. For example, the six-step algorithm is not only insensitive to harmonics 2, 3, and 4, but also to harmonics 6, 8, 9, 10, 12, 14.... It is sensitive only to harmonics  $5 + 6p$  and  $7 + 6p$ . Baker et al. [151] found that the period of primary nonlinearity phase error is equal to the number of phase shifts of the captured fringe patterns [e.g., in 3-step PSP, the nonlinear phase error is 3rd-order harmonics, as shown in Figs. 15(c)]. Besides the standard phase shifting algorithms, some other special PSP algorithms have been developed to compensate the nonlinearity error specifically. Hibino et al. [152] designed a phase shifting algorithm that is able to eliminate the effects of harmonic components of intensity signal and a constant phase-shift error with at least 5 projected patterns. Huang et al. [90] proposed the double three-step phase shifting algorithm, which can cancel 2nd order nonlinearity in the polynomial model by averaging two distorted phases with opposite distortion directions (introduced in Section 3.2).

Though using a large number of phase shifting steps can completely remove the effects of nonlinearity theoretically [138,143,153], it requires much longer pattern sequence, more storage space, and longer processing time, which is unappealing for applications of high-speed and real-time measurements. Therefore, many phase compensation algorithms have been proposed to compensate the nonsinusoidal phase error without the need for additional fringe patterns [98,138,141,151,154–159]. For example, Zhang and Huang [154] proposed a look-up-table (LUT) based approach to compensate the phase error directly without employing any mathematical gamma model. The LUT is built based on the phase error calculated from the calibrated gamma of the projector. Zhang and Yau [155] presented another LUT-based phase compensation algorithm that is generic for any phase shifting methods. Without calibrating the gamma of the projector, the LUT is directly established by analyzing the captured fringe images of a flat board directly. Inspired by Zhang's work [155], Jia et al. [98] also proposed a LUT-based compensation algorithm for their two-step triangular phase shifting method. Guo et al. [136] employed statistical methods to analyze and correct for gamma distortion by framing gamma distortion as an uncertainty problem. Pan et al. [156] proposed an iterative phase compensation algorithm based on the period of nonlinearity phase error being equal to the number of phase shifts of the captured fringe patterns. Liu et al. [138] developed a mathematical model for predicting the phase error introduced by gamma distortion and corrected the phase error by solving an nonlinear optimization problem.

Compared with previous active methods, passive phase compensation approaches have to be performed pixel by pixel after measurement, which takes more computing effort. Besides, caution should be given to the calibration conditions and the measurement conditions [135]. Considering the nonlinearity error is a kind of systematic error, the active methods are often preferable if such methods can be adopted. The calibration precedence, though elaborate and time-consuming, only needs to be done once before the measurement. However, in some special circumstances that the time-variant feature of the projector nonlinearity has to be considered explicitly [144,160], reference-based calibration methods cannot follow the drift in the parameters over time. As a re-

sult, passive phase compensation approaches or active methods with self-calibration capability should be used because they are able to continuously suppress the nonlinearity effect without a prior calibration of the intensity response of the projector or of the phase errors.

#### 4.3. Lens defocusing

In sinusoidal phase shifting methods, image defocus will not introduce phase error theoretically because a sinusoidal pattern will still be a sinusoidal pattern when the image is defocused, even though the fringe contrast may be reduced. The defocus effect can be mathematically modeled as the convolution of an ideal sharp image with the point spread function (PSF) of the imaging system, which is usually approximated by a circular Gaussian function:

$$h(x, y) = \frac{1}{2\pi\sigma^2} \exp\left(-\frac{x^2 + y^2}{2\sigma^2}\right) \quad (87)$$

where the standard deviation  $\sigma$  is proportional to the defocusing level. In the frequency domain, the image spectrum is also filtered by the optical transfer function (OTF) of the imaging system accordingly, which is just the Fourier transform of the PSF. As the Fourier transform of a Gaussian function is also a Gaussian function, the OTF is also of Gaussian shape with its width controlled by  $\sigma$ . It attenuates the image spectrum especially for high spatial frequencies. Since the sinusoidal fringe contains only single frequency component, lens defocusing will not change the shape of the waveform but diminish its amplitude, as illustrated in Fig. 17(a) and (b). For non-sinusoidal pattern, such as trapezoidal or triangular phase shifting patterns, image defocus will smooth the waveform, which causes errors that cannot be ignored [94,99]. In general, lens defocusing may affect the measurement result or introduce measurement error if the pattern's waveform is not a smooth function (contains edges, stairs, or abrupt changes) [see Fig. 17(c) and (d)]. In some temporal phase unwrapping approaches, e.g. Gray code [161–164] and stair phase coding methods [165–167], image defocus may also introduce phase unwrapping errors around sharp regions of the pattern, as will be discussed in Section 5.

Rather than just being a kind of error source, lens defocusing can also be utilized as an optical low-pass filter to optimize the projected fringe patterns. As we mentioned in Section 4.2, lens defocusing is helpful to alleviate the nonlinear response of the projector and reduce the associated phase measurement error [141,145,146]. On the other hand, for high-speed (kHz) 3D shape measurement applications, it is preferable to employ only low-bit patterns for fringe projection. Because the DMD is a binary digital device (can be either 'on' or 'off'), a gray-scale image is created with the binary temporal pulse-width-modulation, and the intensity level is reproduced by controlling the amount of time the mirror is on/off. So the less gray-scales are used, the fewer cycles are needed for the DMD to recombine the pattern signals. If binary patterns are used for fringe projection, the DMD can operate in 1-bit mode, which allows for the maximum projection rate up to tens of kilo-Hz [128,168,169]. Since 1-bit grayscale (0 and 1) is insufficient to create an ideal sinusoidal pattern, the lens defocusing has been further introduced as a low-pass filter to filter out the unwanted high-order

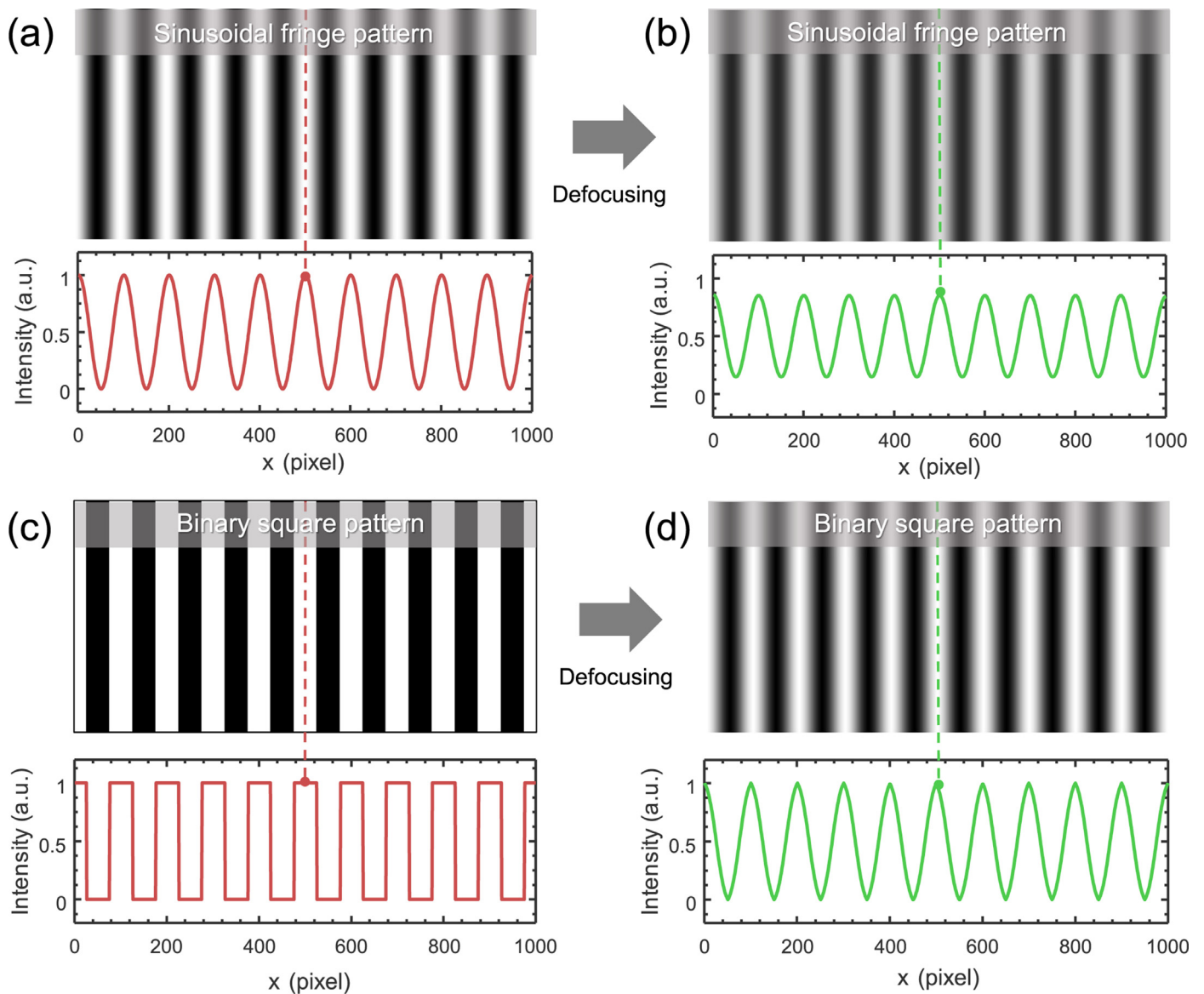


**Fig. 17.** Effect of lens defocusing on sinusoidal fringe pattern and binary square pattern (a  $50 \times 50$  Gaussian kernel with  $\sigma = 15$  is used to simulate the defocusing effect). (a) Ideal sinusoidal fringe pattern; (b) sinusoidal fringe pattern after defocusing; (c) ideal binary square pattern; (d) binary square pattern after defocusing.

harmonics in the waveforms in order to make them become more sinusoidal (as illustrated in Fig. 17(c) and (d), a binary square wave can become ‘quasi-sinusoidal’ after defocusing). It should be mentioned that the similar problem was also encountered earlier in the fringe projection techniques based on a physical grating because an accurate grating with sinusoidal transparency is difficult to manufacture. To address this problem, defocused projection of square wave generated by a Ronchi grating was proposed, which can produce high-quality sinusoidal patterns for PSP phase evaluation [170]. The sinusoidality of fringe patterns can also be improved by area modulation technique, which utilizes only two grayscales to approach the sinusoidal transparency function in the spatial domain during micro-manufacturing [171]. The main concept of these approaches has later been adopted to digital FPP, and a number of approaches have been developed to optimize the defocused binary pattern in order to create ideal sinusoidal pattern or achieve higher measurement accuracy, e.g., squared binary pattern [146], sinusoidal pulse-width-modulation (SPWM) [111,172,173], optimal pulse-width-modulation (OPWM) [173,174], binary dithering techniques [175], and optimized-dithering techniques [176–179]. Besides, as mentioned in Section 5.2, phase shifting techniques have inherent resistance to cer-

tain order harmonics components. This property has also been considered and well-studied for optimizing the binary patterns and reducing the phase reconstruction error [173,179,180]. A detailed introduction of these binary defocusing techniques can be found in [160].

#### 4.4. Phase shifting error

In the field of PSI, the phase shifting error is the principal error source affecting the measurement precision of an interferometric system. Most phase shifting techniques assume a fixed and known phase step size. However, non-linearities in the movement of a piezoelectric ceramic transformer (PZT) performing the phase shifting, or a miscalibration of phase step size can cause the phase shifting error. The phase shifting error will influence inevitably the accurate phase reconstruction if a conventional phase shifting technique is used, as illustrated in Fig. 18. It has been shown by Schwider et al. [181,182] that for a small phase shift error  $\epsilon_p$ , the corresponding phase error calculated by standard N-step phase shifting algorithm is at double the frequency of

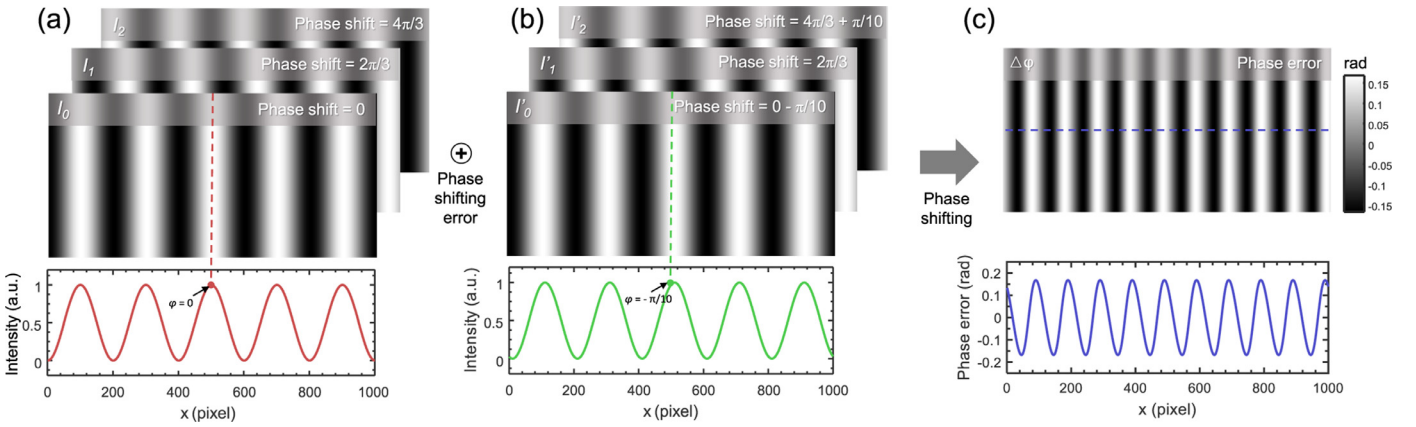


Fig. 18. Effect of phase shifting error on the phase reconstruction. (a) Ideal three-step phase shifting patterns and the corresponding cross section; (b) mis-calibrated three-step phase shifting patterns with a phase shifting error of  $\pi/10$ ; (c) resultant phase reconstruction error.

the phase [this phenomenon can be clearly observed in Figs. 18(c)]

$$\Delta\phi(x, y) \approx a + b \cos[2\phi(x, y)] + c \sin[2\phi(x, y)] \quad (88)$$

where the coefficients  $a$ ,  $b$ , and  $c$  are approximately proportional to  $\epsilon_y$ . Creath [183] also analyzed the phase shifting error by simulation, confirming  $2\phi$  nature of the phase error, and showing that the greater the number of steps, the lower the amplitude of the phase error. Therefore, to reduce the phase shifting error, one can increase the number of phase shifting steps, or select a phase shifting algorithm that is less sensitive to the phase shifting error, such as the Carré [184] and Hariharan phase shifting algorithms [85] (discussed in details in Section 3.3). It should be mentioned that in digital FPP system, the phase shift is generated by a digital projector based on a software program, so theoretically, there is no phase shifting error.

#### 4.5. Motion-induced error

Though digital FPP is totally free from phase shifting error, there is another kind of error so-called motion-induced errors or motion artifacts, which are quite relevant. In conventional PSP, the measured scene is considered static during the capture of the multiple phase-shifted images, so the measured phase will not change. This condition may not hold when the scene becomes dynamic, even a high-speed FPP system is used.

As illustrated in Fig. 19, when the measured surface is not motionless during the acquisition process, one point in the projected pattern sequence can be mapped to different points on the object surface, so the same scene point in the sequentially captured images will have different phase values rather than sharing the same as value in the static case. For example, in 3-step PSP, the intensity images actually captured can be described as

$$I_0 = A + B \cos(\phi - \Delta\phi_1) \quad (89)$$

$$I_1 = A + B \cos(\phi - 2\pi/3) \quad (90)$$

$$I_2 = A + B \cos(\phi - 4\pi/3 + \Delta\phi_2) \quad (91)$$

where  $\Delta\phi_1$  and  $\Delta\phi_2$  are the motion-induced phase offsets with respect to the middle image ( $I_1$ ). It can be seen from Fig. 19 that when the surface is moving towards/away from the measurement system (along the  $z$ -axis), the phase step size is no longer  $2\pi/3$ , which causes the phase measurement error that is quite similar with the phase shifting error. As discussed in Section 4.4, increasing the number of phase shifting steps or using specific algorithms can reduce the phase shifting error. However, it will extend the pattern sequence and prolong the measurement

time (for example, Hariharan phase shifting algorithm [57,85] requires 5 fringe patterns), making the measurement still very sensitive to motion.

Since using the minimum number of fringe images is desirable for reducing the measurement time, researchers tried to improve the three-step phase shifting algorithm in order to explicitly account for the motion-induced error. Weise et al. [121] assumed a linear phase offset model (motion is uniform  $\Delta\phi_1 \approx \Delta\phi_2$ ) for 3-step phase shifting algorithm and used Taylor approximation to generate a close-form expression for the motion error in order to apply motion compensation on a pixel level. Based on a local smoothness assumption, a linear least-square fit is performed in the local neighborhood of each pixel to solve for unknown phase offset and the real phase. Cong et al. [185] proposed a Fourier-assisted phase shifting approach in which the motion-related phase offset in 3-step PSP is estimated by differentiating the phase measurements generated from two adjacent frames with FTP. This approach does not impose specific restrictions on the real phase and works well for the case of non-uniform motion. Li et al. [186] also proposed a hybrid computational framework to reduce motion-induced error by combining the FTP with the PSP. With the assistance of geometric constraints, the high-frequency phase recovered by FTP is unwrapped based on the low-frequency phase obtained by PSP, resulting in an absolute phase map that is resistant to phase errors caused by rapid object movements.

When the measured surface is not simply moving towards/away from the measurement system, the associated measurement error becomes more complicated to analyze. For example, if the direction of sinusoidal patterns is parallel to the motion direction, the movement of the measured object will introduce both the phase shifting error and the surface misalignment. In such cases, pixel matching algorithms [102,187–189] and arbitrary unequal-step phase shifting [190] need to be used to obtain reliable measurements. Otherwise, large measurement error and outliers will occur by simply applying conventional PSP algorithms [191,192]. For more complicated 3D movement of a rigid object, Lu et al. [193] developed a model to describe the fringe patterns influenced by the 3D movement, and refines the unknown phase offset by the least-squares method with constraints of the background intensity and the fringe modulation. Considering different kinds of motion in directions of  $x$ ,  $y$ , and  $z$ , Feng et al. [194] classified the motion-induced artifacts into 3 categories: motion ripples, motion-induced phase unwrapping error, and motion outliers, and developed their respective countermeasures. The phase error (motion ripples) is compensated based on the statistical nature of the sinusoidal fringes; the phase unwrapping errors are corrected by exploiting adjacent reliable pixels, and the outliers are removed by comparing the original phase map with a smoothed phase map.

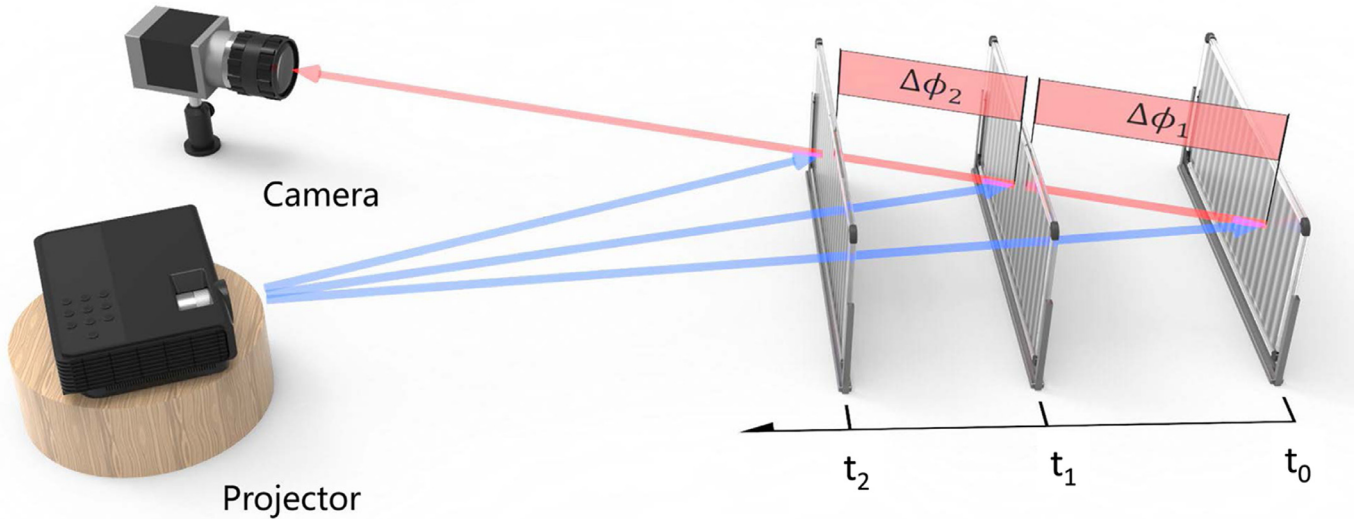


Fig. 19. Illustration of motion-induced phase shifting error in conventional three-step PSP. The measured surface is moving towards the measurement system.

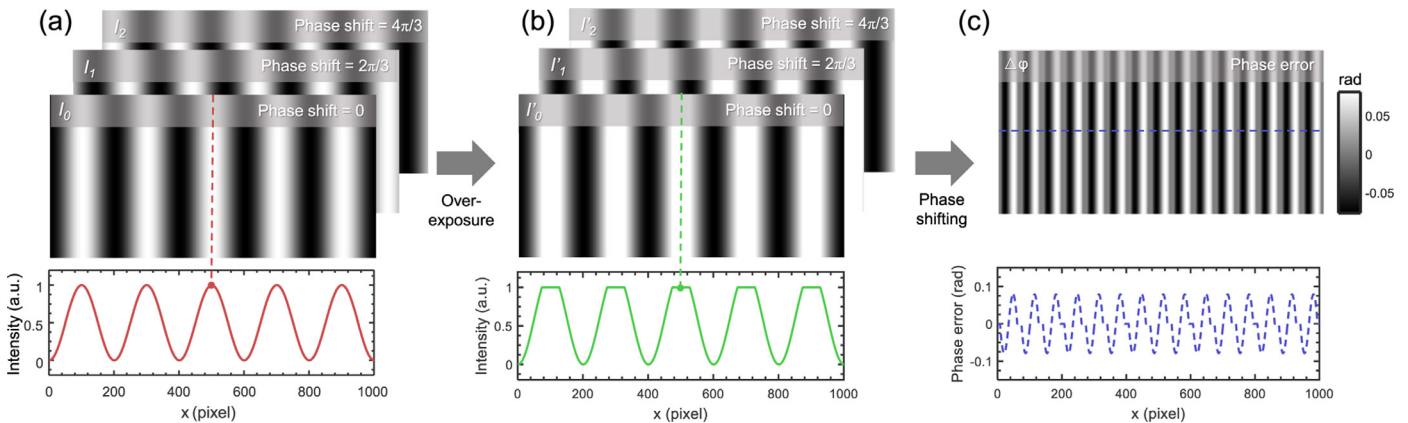


Fig. 20. Effect of intensity saturation on the phase reconstruction. (a) Ideal three-step phase shifting patterns and the corresponding cross section; (b) saturated three-step phase shifting patterns and the corresponding cross section ( $1.2\times$  gain, the original intensity values with a dynamic range of  $[0, 1.2]$  are truncated to  $[0, 1]$ ); (c) resultant phase reconstruction error.

#### 4.6. Intensity saturation

Intensity saturation may take place as a fringe pattern is projected onto an object which has a relatively high reflectivity, or the camera exposure time is set too long. If saturated fringe patterns are used in conventional PSP, the phase error will occur due to the truncated intensity profile of the fringe pattern, as illustrated in Fig. 20. To prevent or compensate the saturation-induced phase error, many state-of-the-art methods have been proposed, and they can be classified into 3 categories: exposure-based approaches [117,118,195–197], projection-based approaches [198–206], and post-processing compensation algorithms [103,207–210].

In exposure-based approaches, the camera exposure is properly adjusted according to the surface reflectivity in order to prevent intensity saturation. For example, Zhang et al. [117] proposed a high dynamic range scanning technique in which a set of fringe images are captured with different exposure times, and the brightest but unsaturated pixel in the fringe pattern set are used to calculate the phase value on a pixel by pixel basis. Instead of choosing the brightest pixel, Jiang et al. [118] presented a similar multi-exposure approach which uses the intensity modulation as the criterion to determine the best fringe pattern set. Ekstrand et al. [195] presented an auto-exposure technique, in which the expo-

sure time is automatically adjusted according to the reflectivity of the measured object. Ri et al. [196] presented an intensity range extension method using a self-developed DMD camera. Each pixel of the camera corresponds exactly to one mirror of the DMD, which can modulate the brightness of incoming light for each camera pixel independently to prevent overexposed areas. Yin et al. [197] suggested a high dynamic range 3D measurement technique based on a single-chip color camera. From the single-shot raw data of the color camera, 4 monochrome sub-images corresponding to R, G, G and B channels can be obtained and synthesized to avoid over-exposure.

The projection-based approaches, however, avoid intensity saturation by adjusting the intensity and contrast of the projected fringe pattern. Waddington and Kofman [198] suggested to project different groups of sinusoidal fringe images with modified maximum input gray levels. This technique follows the similar idea as in the multi-exposure approach but the image intensity is controlled by the projector rather than the camera. Babaie et al. [202] presented a high dynamic range measurement technique that recursively controls the intensity of the projection pattern at pixel level based on the feedback from the reflected images captured by the camera. Li and Kofman [200] proposed an adaptive fringe-pattern projection method that accommodates the maximum input gray level in projected fringe patterns to the local reflectivity of

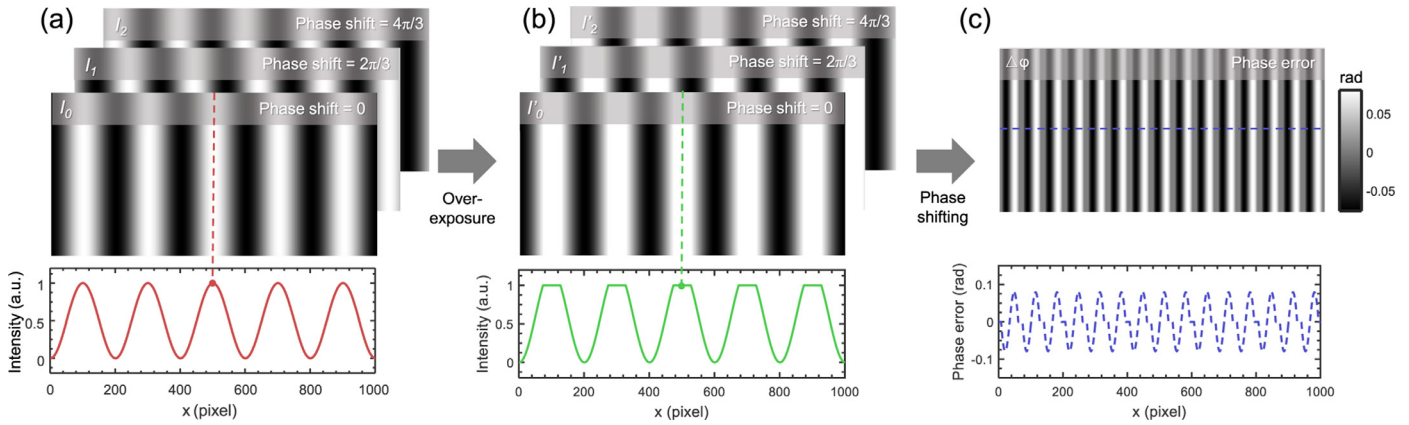


Fig. 21. Effect of illumination fluctuation on the phase reconstruction. (a) Ideal three-step phase shifting patterns and the corresponding cross section; (b) three-step phase shifting patterns captured under fluctuating illumination and the corresponding cross section; (c) resultant phase reconstruction error.

an object surface being measured. Lin et al. [203] developed a similar method to measure objects with a large range of reflectivity variations by adaptively adjusting the pixel-wise intensity of the projected patterns based on non-linear regression. Besides directly controlling the projection intensity, polarization optics have also been introduced in high dynamic range 3D measurement due to their unique advantage of effective specular highlight suppression. Chen et al. [204] introduced two linear polarizers in front of both the projector and the camera and combined the polarization-difference imaging with the phase shifting method to measure shiny objects. Salahieh et al. [205] proposed to use a polarization camera with a pixelated polarizer array which allows to capture 4 images with different polarization states with single camera exposure. The intensity saturation can be effectively avoided by selecting different polarization measurements. It should be mentioned that the projection-based or polarization-based approaches can also be combined with multi-exposure approaches to achieve more accurate measurements for objects with very high dynamic range of surface reflectivity, as demonstrated by Feng et al. [206].

The final category of approaches overcome the saturation-induced phase error by post-processing compensation algorithms. For example, Chen et al. [207] tried to modify the phase retrieval algorithm to bypass the intensity saturation problem based on conventional  $N$ -step ( $N > 3$ ) phase shifting fringe patterns. Since the minimum number for phase shifting is 3, if there are at least three unsaturated intensity values at the same pixel, the phase can be reconstructed accurately without any disturbance from the saturated intensity image. The phase-recovering algorithms corresponding to five- and seven-step phase shifting method were deduced by Hu et al. [103,208]. Guo and Liu [211] proposed a phase shifting algorithm based on Hough transform, which is able to alleviate the impacts of intensity saturation and produce high-accuracy phase reconstruction from saturated fringe patterns. Jiang et al. [210] proposed a real-time high dynamic range scanning method by projecting additional inverted fringe patterns to complement the saturated pixels in original 3-step phase-shifted fringe images. Chen and Zhang [209] proposed to use a large-step phase shifting algorithm to overcome the intensity saturation error. All captured fringe images are used for phase calculation regardless of whether they are saturated or not. Since the intensity saturation can also be regarded as a special kind of nonlinearity error, it is not difficult to understand that using a sufficiently large number of phase shifting steps can completely eliminate the saturation error.

#### 4.7. Illumination fluctuation

In most phase shifting algorithms, the background intensity and modulation at each point of the fringe patterns are assumed to be constant during phase shifting. In practical measurement, however, this

condition is not always satisfied due to the power fluctuations of light sources and the instability of environmental lighting. It has been found that the stability of the projected light intensity significantly decreases with aging of the projector bulb [212]. For DLP projectors, the transient response of the DMD may also introduce illumination fluctuations especially with short exposure times because the camera may capture the dynamic binary on/off integration of the DMD pixels during image formation [213]. When there are uniform fluctuations of projection and ambient light, the captured phase shifting fringe patterns can be represented as

$$I_n(x, y) = \alpha_n A(x, y) + \beta_n B(x, y) \cos[\phi(x, y) - 2\pi n/N] \quad (92)$$

where  $\alpha_n$  and  $\beta_n$  are the fluctuation factors of the background and modulation, respectively. The fluctuation of intensity changes the average intensity and modulation of the fringe patterns, which contributes to phase errors, as illustrated in Fig. 21.

Several approaches have been proposed to prevent or compensate the phase error associated with illumination fluctuations. Among them, the most straightforward approach is to use a highly stabilized light source in the measurement system. For example, Lu et al. [214] used a xenon lamp with intensity stability better than 0.2% as the light source of a FPP system, which guarantees that the phase measuring error induced by the illumination fluctuation does not exceed 0.002 rad in theory. An additional photo-detection device can be introduced to monitor illumination variations in real time, which provides a feedback to the stabilization or compensation mechanisms [215,216]. Besides these hardware-aided techniques, a more convenient and economic solution is to compensate the illumination fluctuations by post-processing the captured fringe patterns. If the fluctuation of the source is random and varying rapidly, simply averaging multiple fringe images at each phase shifting step can effectively mitigate the effect of the illumination fluctuations [212]. In the presence of systematic and slowly varying intensity fluctuations, specific algorithms have to be designed. Based on an assumption that the power of the light source varies linearly as the phase shift, Onodera and Ishii [217] developed a six-step phase shifting algorithm for compensating for the linear change in illumination in PSI. Several iterative self-calibrating PSI algorithms have also been proposed, which allow to estimate the mis-calibrated phase shifts as well as the fluctuation factors simultaneously [218,219]. However, due to more unknowns are involved, these self-calibrating PSI approaches generally require capturing more additional fringe patterns in order to make the system of equations well-determined. To compensate the illumination fluctuations in FPP, Zhang et al. [21] proposed a method based on empirical mode decomposition algorithm to remove the intensity fluctuations caused by background light and the intensity of projection system light source before phase calculation. Lu et al. [220] segmented each phase shifting fringe pattern using Otsu's method and then corrected the

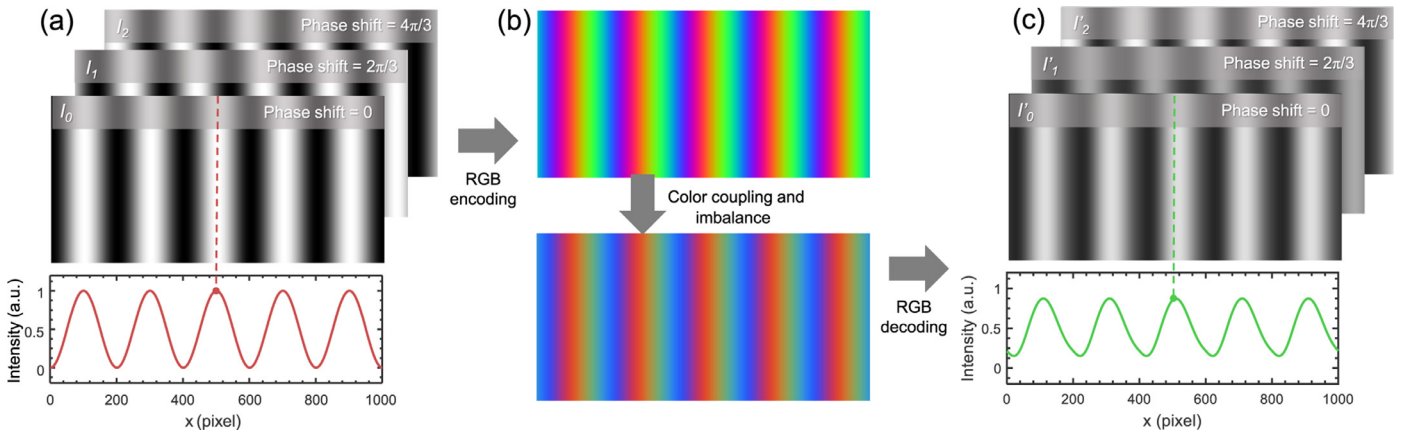


**Fig. 22.** Illustration of color coupling and imbalance in color fringe projection. (a) Ideal three-step phase shifting patterns and the corresponding cross section; (b) the color pattern after RGB encoding and the corresponding distorted color pattern with color coupling and imbalance; (c) the distorted three-step phase shifting patterns and the corresponding cross section after RGB decoding. (For interpretation of the references to color in this figure legend, the reader is referred to the web version of this article).

effect of the illumination fluctuations based on a linear gray-level transformation. Chen et al. [221] investigated the characteristics of the instability of light source and found that the time-dependent phase error can hardly be uniquely represented by a deterministic function for different measurements, precluding the use of pre-calibration-based compensation procedures. Thus, they proposed two real-time correction methods for reducing the time-dependent phase error by introducing additional reference regions for obtaining the time-dependent phase error and establishing the mapping function.

#### 4.8. Coupling and imbalance error in color fringe projection

For conventional PSP techniques, multiple phase-shifted monochrome fringe patterns are sequentially projected onto the object surface and then captured by a monochrome camera. However, this multiple-shot mechanism is sensitive to object motion during the time gap between two images. Single-shot color fringe pattern techniques have been used to address this problem because three color channels can encode three separate fringe patterns within one single color pattern [30]. When the color fringe image is captured with a color camera, three monochrome fringe images can then be extracted from the three color (RGB) channels. The whole process of color fringe encoding and decoding is illustrated in Fig. 22.

Color fringe projection enables three-step phase shifting in one color fringe [222–225] [see Fig. 25(b)], allowing for fast measurement of dynamic scenes. However, for color fringe projection, color coupling and imbalance will distort the intensities of fringe patterns encoded in the three color channels, resulting in major errors in the phase reconstruction [see Fig. 25(c)] [30,159,222–230]. Projectors and cameras are usually designed to have some overlaps with the spectra of the color channels to avoid color-blind regions in the spectrum, which unfortunately causes color coupling. Because of color coupling, the three primary color channels cannot be split correctly from a color fringe pattern. As a result, the three phase-shifted fringe patterns will have distorted intensity profiles, which causes significant errors in phase calculation. Many correction methods based on either hardware or software have been proposed to address the color coupling problem in color FPP [159,223–227,229,230].

Color imbalance is another big challenge. Because human eyes have different sensitivity to different colors, most projectors are intentionally designed to have different intensity responses for RGB colors. In PSP, the imbalances among the three color channels (corresponding to three fringe images) may lead to phase error. The color imbalance problem is also related to the nonlinearity effect of the projector (see Section 4.2 for

details), but three color channels (RGB) need to be compensated simultaneously [222–225,227,230]. The measurement of colored object surface is also an important problem requiring special considerations. Since RGB colors of the fringe image captured by the camera are dependent upon both the projected fringe and the surface color of the measured object, it is very challenging to measure a colored object accurately with color fringe projection.

Finally, it should be also mentioned that for most single-chip DLP projectors, the RGB channels of a color image are actually displayed sequentially, modulated by a synchronized rotating color wheel [109,120,121,231]. Thus, in order to achieve accurate phase measurements, the color fringe projection technique can only be applied when the camera frame rate is much lower than (or exactly integer times of) the refresh rate of a digital video projector.

## 5. Phase shifting algorithms for absolute phase recovery

In PSP, the sinusoidal fringe pattern with zero phase shift carries the absolute phase information that is defined implicitly on itself and its phase-shifted counterparts. Although the intensity distribution in a sinusoidal fringe pattern is periodic with  $2\pi$  phase ambiguity, the absolute phase value is unique at every pixel due to the use of fringe order information. Once the absolute phase  $\Phi(x, y)$  is obtained, we can establish a unique correspondence value  $x^p$  for each camera pixel  $(x, y)$  through the linear equation

$$\Phi(x, y) = 2\pi f^p x^p = \frac{2\pi}{\lambda} x^p \quad (93)$$

where  $\lambda$  is the fringe wavelength/pitch (in pixel) and obviously  $f^p = 1/\lambda$ . However, when using phase shifting algorithms described in Section 3 for phase measurement, the acquired phase map of the surface being measured is wrapped within principle values ranging between  $-\pi$  and  $\pi$ , which means the fringe order information is lost. In order to recover the fringe orders and obtain the absolute phase map of the measured surface, phase unwrapping needs to be performed. As demonstrated in Fig. 23, the rudimentary phase unwrapping procedure is revealed as a process concerned with finding the fringe order  $k$  for each camera pixel  $(x, y)$  and adding corresponding integer multiples of  $2\pi$ :

$$\Phi(x, y) = \phi(x, y) + 2\pi k(x, y) \quad (94)$$

As we mentioned in introduction, there are two principal groups of phase unwrapping algorithms: spatial phase unwrapping [58–61] and temporal phase unwrapping [68–70,72,81,232]. Since the spatial phase unwrapping methods are based on the phase information of spatial

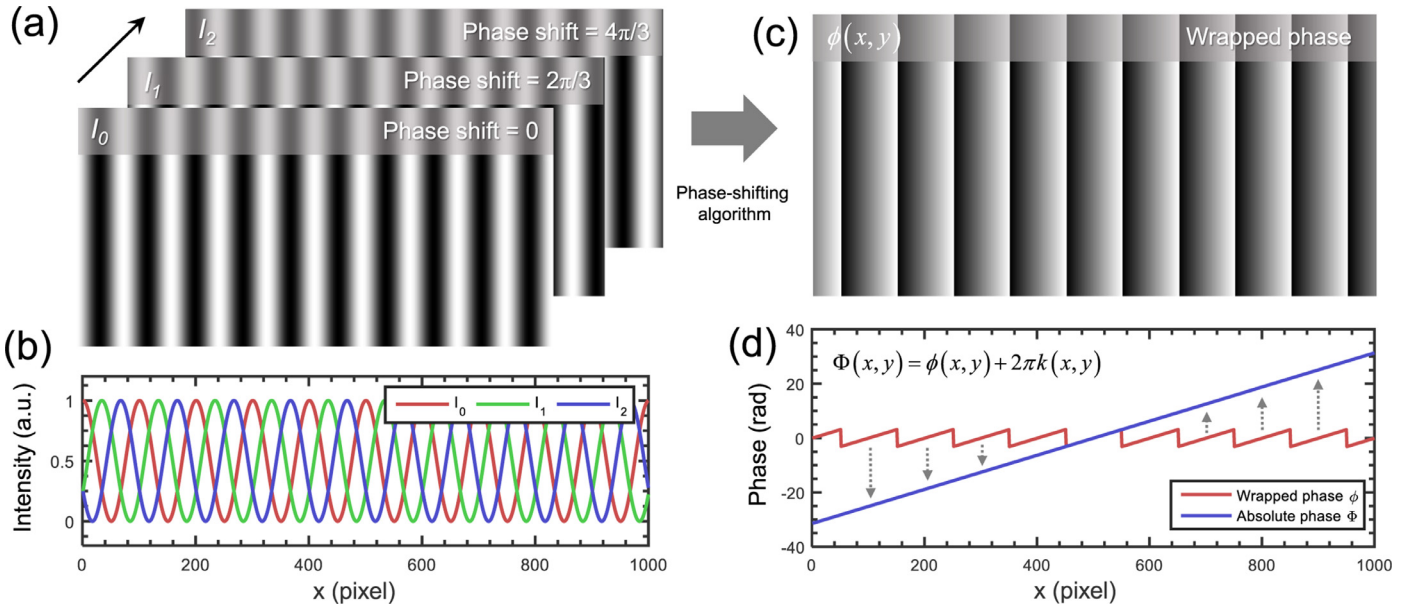


Fig. 23. Example of three-step phase shifting algorithm and phase unwrapping. (a) three-step phase shifting patterns; (b) intensity cross sections of  $I_0$ ,  $I_1$ , and  $I_2$ ; (c) wrapped phase map retrieved by phase shifting algorithm; (d) the relation between the wrapped phase  $\phi(x, y)$  and the absolute phase  $\Phi(x, y)$ .

neighboring pixels, it cannot uniquely determine the period numbers of isolated surfaces or depth discontinuities by using only single phase distribution. Thus, to unwrap a more general phase map which may contain large discontinuities and separations, temporal phase unwrapping approaches should be used.

### 5.1. Phase shifting plus standard temporal phase unwrapping (3+3) method

Standard temporal phase unwrapping (TPU) algorithms unwrap the wrapped phase map with the aid of additional wrapped phase maps with different fringe periods. This category of algorithms can be further divided into 3 sub-groups: multi-frequency (hierarchical) approaches [68,69,78], multi-wavelength (heterodyne) approaches [70,71,79], and number theoretical approaches [72,73,80,81]. These methods are investigated and compared in details in [82], and it has been found that the multi-frequency (hierarchical) approach provides the best unwrapping reliability and is the most robust to noise. Besides, it is quite easy to implement. In the following part of this review, we only use two-frequency hierarchical TPU as a representative of these TPU approaches. But it should be noted that the following PSP schemes may also be combined with other related TPU algorithms.

The two-frequency hierarchical TPU requires two wrapped phase maps with different fringe pitches. These two wrapped phase maps are both retrieved from phase shifting algorithm or other phase detection approaches, ranging from  $-\pi$  to  $\pi$ . The first set of phase shifting patterns is normal high-frequency periodical fringes, which leads to a high-frequency phase map  $\phi_h(x, y)$  with several  $2\pi$  wraps. The other (low-frequency) phase map  $\phi_l(x, y)$  is retrieved by using a set of unit-frequency patterns, and thus, no phase unwrapping is required. This unit-frequency phase is then used as a reference to determine the integer fringe order  $k_h(x, y)$  of the high-frequency phase map  $\phi_h(x, y)$  for each pixel

$$k_h(x, y) = \text{Round} \left[ \frac{(\lambda_l / \lambda_h) \phi_l(x, y) - \phi_h(x, y)}{2\pi} \right] \quad (95)$$

where  $\text{Round}[\ ]$  denotes to obtain the closest integer value. By this means the high-frequency phase  $\phi_h(x, y)$  can be successfully unwrapped based on Eq. (94). Since according to the phase shifting formula [Eqs. (7) and (8)], the minimum number of patterns required to get the phase

information is 3. So if we implement TPU based on standard PSP algorithms, at least 6 patterns (two separate 3-step phase shifting patterns) should be involved for obtaining two wrapped phases  $\phi_h$  and  $\phi_l$ , as illustrated in Fig. 24. In the following, we refer this specific phase shifting plus standard TPU method as 3+3 phase shifting algorithm for simplicity.

### 5.2. Phase shifting plus Gray code method

The Gray code is a popular SL technique which uses projection patterns with only black and white fringes [38]. It can be used by itself for phase measurement, or as a phase unwrapping tool for phase shifting method [67]. The basic idea of Gray code method is to construct a set of binary fringe patterns with different fringe arrangements such that the projection pattern space can be partitioned into a number of sections and each section can be uniquely identified by its binary intensities in the sequence of patterns.

If a number of  $N$  patterns are used, the number of sections defined in the projection pattern space could reach  $2^N$ . Since every partition in the projection pattern space is related to a certain range of absolute phase values, the possible range of the pixel's absolute phase value can be determined. The phase unwrapping process can hence be done by adding multiples of  $2\pi$  to the wrapped phase value of the pixel, which can be obtained from phase measurement techniques such as phase shifting method, to make it consistent with the known range of the pixel's absolute phase value. For a phase map with the total number of fringe orders  $F$ , the minimum number of additional Gray code patterns required is  $\lceil \log_2 F \rceil$ , where  $\lceil \cdot \rceil$  is the ceiling operator. Since the entire duration of data acquisition may be significantly prolonged due to the extended pattern sequence (especially when  $F$  is large), this approach proves to be inefficient in time-critical measurement situations [108,109]. Furthermore, pattern edges blur caused by lens defocusing is also an additional error source [161–163,233]. It is common to see pixels incorrectly unwrapped at the partial boundary between different Gray coded image areas. Therefore, improving the coding efficiency by introducing color-multiplexing or additional gray-scale to the Gray code (instead of using black/white pattern) [164,234] and eliminating/compensating the edge error by monotonicity detection [161], medium filter [163], or projecting an additional complementary code pattern [162] are still hot research topics in this area.

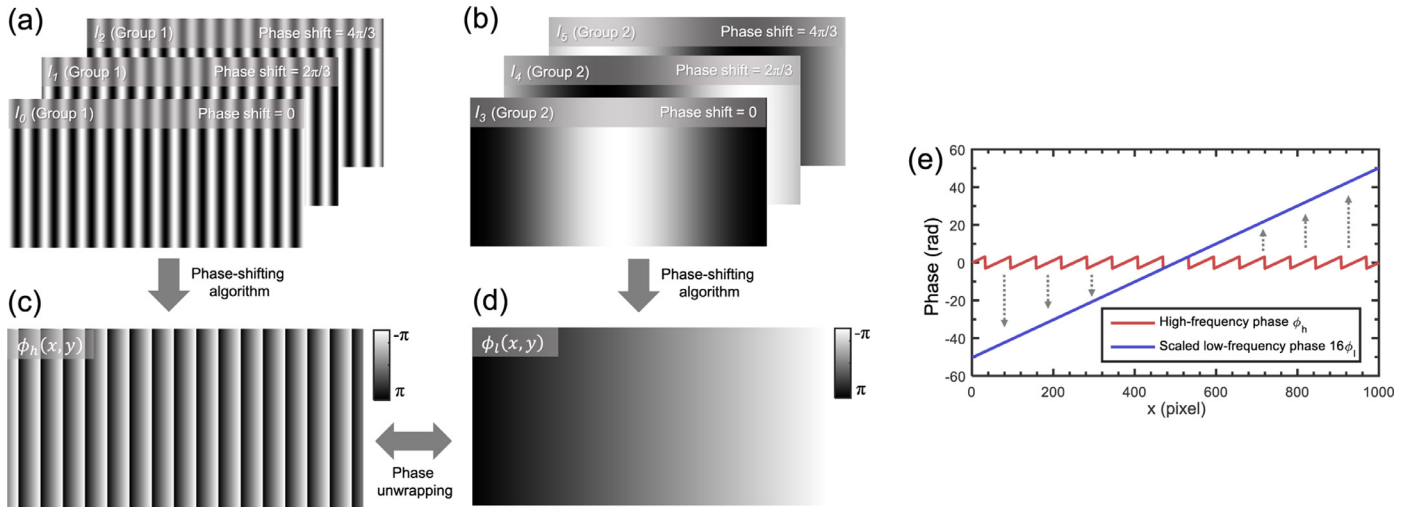


**Fig. 24.** Example of 3 + 3 step phase shifting algorithm and TPU. (a) Three-step phase shifting high-frequency patterns; (b) Three-step phase shifting unit-frequency patterns; (c) high-frequency wrapped phase map  $\phi_h$  retrieved by phase shifting algorithm; (d) unit-frequency wrapped phase map  $\phi_l$  retrieved by phase shifting algorithm; (e)  $\phi_l$  is scaled and served as a reference to unwrap  $\phi_h$ .

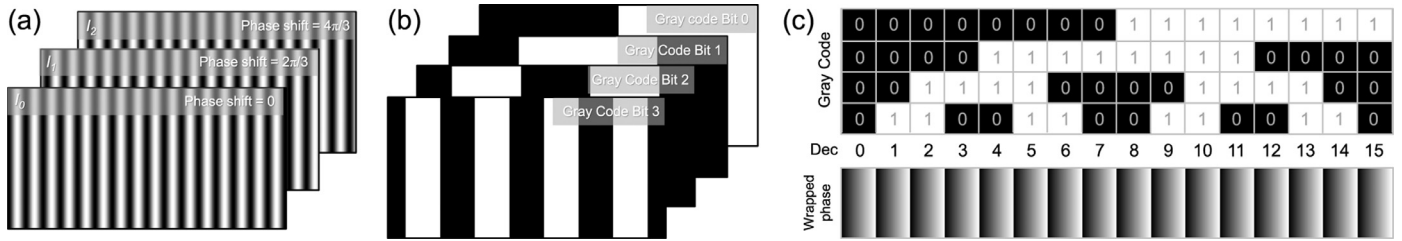


**Fig. 25.** Three-step phase shifting plus Gray code phase unwrapping. (a) Three-step phase shifting patterns; (b) 4 Gray code patterns; (c) correspondence between the Gray code sequence and the 16 sections of the wrapped phase map  $\phi_h(x, y)$ .

Fig. 25 shows an example of three-step phase shifting plus Gray code phase unwrapping for 16-period fringe patterns. By using the 4 Gray code patterns in a sequence, the wrapped phase space can be partitioned into 16 sections with each section having a unique Gray code sequence [see Fig. 25(c)].

### 5.3. Phase shifting plus phase coding method

To address the disadvantages of Gray code method, such as low coding efficiency and high sensitivity to surface reflectivity, Wang and Zhang [165] proposed a phase coding method for absolute phase retrieval by embedding the  $N$ -bit ( $2^N$  level) codewords into the phase component of 3-step phase shifting patterns. Besides the conventional three-step phase shifting fringe patterns ( $I_0^p$ ,  $I_1^p$ , and  $I_2^p$ ), the additional three phase coding patterns in the projector space can be represented as (see 26):

$$I_3^p(x^p, y^p) = a^p + b^p \cos[\phi_s(x^p)] \quad (96)$$

$$I_4^p(x^p, y^p) = a^p + b^p \cos[\phi_s(x^p) - 2\pi/3] \quad (97)$$

$$I_5^p(x^p, y^p) = a^p + b^p \cos[\phi_s(x^p) - 4\pi/3] \quad (98)$$

where  $\phi_s(x^p)$  is a stair phase function representing the fringe period

$$\phi_s(x^p) = -\pi + [x^p/P] \times \frac{2\pi}{F} \quad (99)$$

Here  $k(x^p) = [x^p/P]$  is the truncated integer representing fringe order for each pixel;  $P$  the fringe pitch, or the number of pixels per period;

and  $F$  the total number of fringe periods. By using standard 3-step phase shifting algorithms, the stair phase can be decoded from the corresponding captured intensity patterns, which can be used to determine the fringe order for each camera pixel. The high-frequency phase can then be unwrapped by adding corresponding integer multiples of  $2\pi$  based on Eq. (94). Since generally the phase coding approach can be represent more than  $8 (2^3)$  unique codewords for phase unwrapping [235,236], it can reduce the pattern count compared with the Gray code approach. Besides, this technique is more robust to surface reflectivity variations because it uses the phase instead of the intensity to determine codewords. But compared with the 3 + 3 phase shifting algorithm discussed in Section 5.1, the advantage of the phase coding approach is not obvious. Similar to the Gray code approach, the designed codewords, though embedded in phase, still contain abrupt edges and discontinuities, therefore the defocus-induced unwrapping error at the boundary between adjacent codewords still remains. This further requires elaborate post-processing algorithms such as the median filter to compensate the associated spike artifacts [166,167].

### 5.4. Dual-frequency pattern scheme

In 3 + 3 phase shifting and phase shifting plus phase coding methods, we need 2 separate groups of phase shifting patterns with at least 6 images. To reduce the number of patterns and minimize the effect of sensor noise, Liu et al. [106] proposed a dual-frequency pattern scheme by superimposing two groups of phase shifting patterns with different frequencies. The dual-frequency patterns in the projector space can be

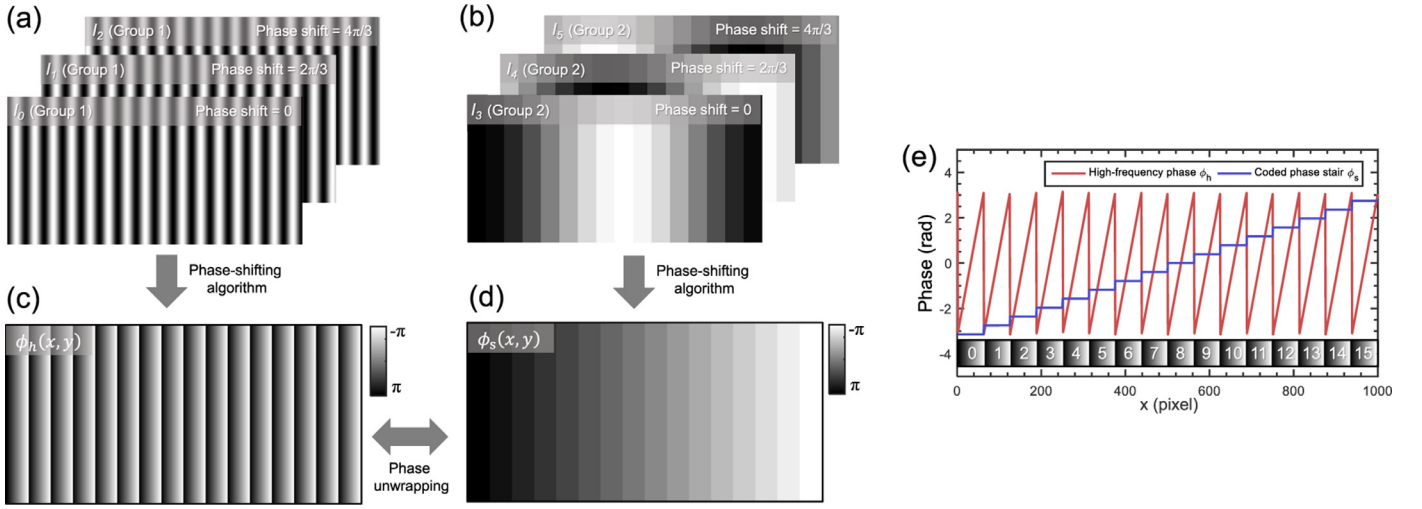


**Fig. 26.** Three-step phase shifting plus phase coding method. (a) three-step phase shifting patterns; (b) three phase coding patterns; (c) wrapped phase map retrieved by phase shifting algorithm  $\phi_h(x, y)$ ; (d) decoded phase stair function by phase shifting algorithm  $\phi_s(x, y)$ ; (e) correspondence between the stair function  $\phi_s(x, y)$  and the 16 sections of the wrapped phase map  $\phi_h(x, y)$ .

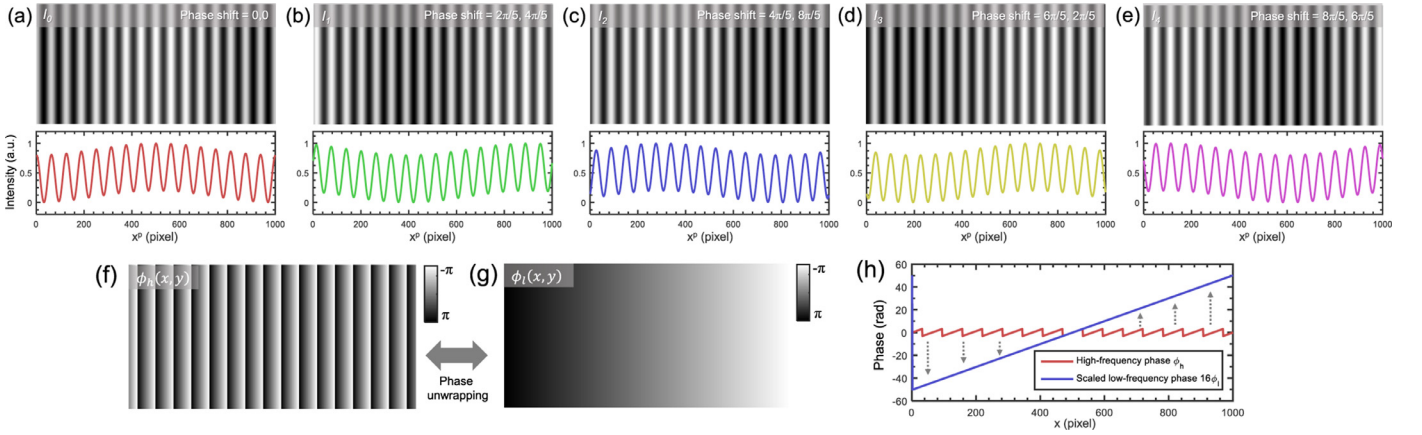


**Fig. 27.** Example of dual-frequency pattern scheme ( $N = 5$ ,  $f_h^p = 16$ ,  $f_l^p = 1$ ,  $a^p = 0.5$ ,  $b_h^p = 0.4$ , and  $b_l^p = 0.1$ ). (a–e) Five dual-frequency phase shifting patterns and their corresponding cross sections; (f) retrieved high-frequency wrapped phase map  $\phi_h(x, y)$ ; (g) retrieved low-frequency phase map  $\phi_l(x, y)$ ; (h) the relation between the high-frequency wrapped phase  $\phi_h(x, y)$  and the scaled low-frequency phase  $16\phi_l(x, y)$ .

represented as:

$$I_n^p(x^p, y^p) = a^p + b_h^p \cos(2\pi f_h^p x^p - 2\pi n/N) + b_l^p \cos(2\pi f_l^p x^p - 4\pi n/N) \quad (100)$$

where the fringe patterns contain two different sinusoidal components with different amplitudes ( $b_h^p$  and  $b_l^p$ ), frequencies (high frequency  $f_h^p$  and unit frequency  $f_l^p = 1$ ), and phase shifts ( $2\pi n/N$  and  $4\pi n/N$ ). The high-frequency component generates wrapped phase, which is more resilient to sensor noise, while the unit-frequency component enables phase unwrapping. In order to cover the entire dynamic range of the projector  $[0, 1]$ , we should choose  $a^p = 0.5$ , and  $b_h^p + b_l^p = 0.5$ . Fig. 27 illustrates the pattern set along with their intensity profiles for  $N = 5$ ,  $f_h^p = 16$ ,  $f_l^p = 1$ ,  $a^p = 0.5$ ,  $b_h^p = 0.4$ , and  $b_l^p = 0.1$ . The corresponding intensities of the captured images are

$$I_n = A + B_h \cos(\phi_h - 2\pi n/N) + B_l \cos(\phi_l - 4\pi n/N) \quad (101)$$

where the intensity modulation of two different sinusoidal components are  $B_h$  and  $B_l$ , respectively. Since there are 5 unknowns in Eq. (101), the minimum number of fringe patterns is 5 ( $N \geq 5$ ), instead of 6 [105]. The solutions to the unknown parameters in Eq. (101) are given by

$$A = \frac{1}{N} \sum_{n=0}^{N-1} I_n \quad (102)$$

$$B_h = \frac{2}{N} \sqrt{\left[ \sum_{n=0}^{N-1} I_n(x, y) \sin(2\pi n/N) \right]^2 + \left[ \sum_{n=0}^{N-1} I_n(x, y) \cos(2\pi n/N) \right]^2} \quad (103)$$

$$B_l = \frac{2}{N} \sqrt{\left[ \sum_{n=0}^{N-1} I_n(x, y) \sin(4\pi n/N) \right]^2 + \left[ \sum_{n=0}^{N-1} I_n(x, y) \cos(4\pi n/N) \right]^2} \quad (104)$$

$$\phi_h = \tan^{-1} \frac{\sum_{n=0}^{N-1} I_n \sin(2\pi n/N)}{\sum_{n=0}^{N-1} I_n \cos(2\pi n/N)} \quad (105)$$

$$\phi_l = \tan^{-1} \frac{\sum_{n=0}^{N-1} I_n \sin(4\pi n/N)}{\sum_{n=0}^{N-1} I_n \cos(4\pi n/N)} \quad (106)$$

Based on above formulas, we can recover two phase maps ( $\phi_h$  and  $\phi_l$ ), ranging from  $-\pi$  to  $\pi$  with a minimum of 5 fringe patterns. The wrap-free unit-frequency phase  $\phi_l$  is then used as a reference to unwrap  $\phi_h$  according to two-frequency hierarchical TPU approach [Eq. (95)], as illustrated in Fig. 27(h). Besides, the large phase shifting steps ( $N \geq 5$ )

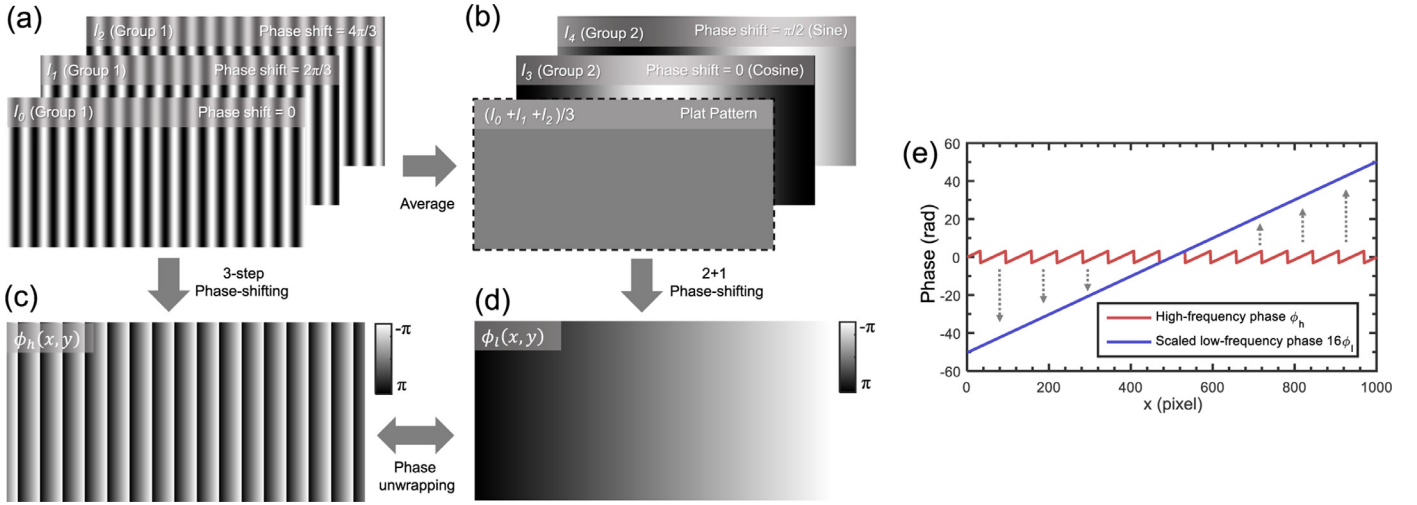


**Fig. 28.** Example of bi-frequency phase shifting algorithm ( $f_h^p = 16$ ,  $f_l^p = 1$ ). (a–e) Three high-frequency phase shifting patterns; (b) two fringe images with  $\pi/2$  phase-shift, the additional flat pattern is obtained by averaging the three high-frequency phase shifting patterns shown in (a); (c) retrieved high-frequency phase map  $\phi_h(x, y)$ ; (d) retrieved low-frequency phase map  $\phi_l(x, y)$ ; (e) the relation between the high-frequency wrapped phase  $\phi_h(x, y)$  and the scaled low-frequency phase  $16\phi_l(x, y)$ .

allow to further reduce the measurement error compared to 3-step PSP algorithm. However, the fringe amplitude should be properly allocated to the two phase components ( $b_h^p$  and  $b_l^p$ ) in order to make a good trade-off between the measurement accuracy and the phase unwrapping reliability.

### 5.5. Bi-frequency (3 + 2) phase shifting algorithm

The bi-frequency phase shifting method proposed by Zuo et al. [111] also employs 5 fringe patterns to realize both high-frequency phase retrieval and TPU. It can be viewed as a special combination of three-step PSP and modified 2 + 1 PSP, in which the flat image is obtained by averaging the three-step phase-shifted images without actual projection. Fig. 28(a) and (b) illustrate the pattern set for  $f_h^p = 16$ ,  $a^p = 0.5$ ,  $b^p = 0.5$ . The first three intensity images captured are the same as those in conventional three-step PSP:

$$I_0 = A + B_h \cos(\phi_h) \quad (107)$$

$$I_1 = A + B_h \cos(\phi_h - 2\pi/3) \quad (108)$$

$$I_2 = A + B_h \cos(\phi_h - 4\pi/3) \quad (109)$$

with the high-frequency phase distribution and the average intensity recovered by

$$\phi_h = \tan^{-1} \frac{\sqrt{3}(I_1 - I_2)}{2I_0 - I_1 - I_2} \quad (110)$$

$$A = \frac{I_0 + I_1 + I_2}{3} \quad (111)$$

In order to obtain an additional phase map with unit frequency, another two fringe images with  $\pi/2$  phase-shift are used:

$$I_3 = A + B_l \cos(\phi_l) \quad (112)$$

$$I_4 = A + B_l \sin(\phi_l) \quad (113)$$

Since the average intensity  $A$  is already calculated from Eq. (111), there is no need to project the flat image any more. By applying the modified 2 + 1 phase shifting algorithm (discussed in details in Section 3.4), the phase for the unit-frequency fringes can be recovered:

$$\phi_l = \tan^{-1} \frac{I_4 - A}{I_3 - A} \quad (114)$$

So with only 5 fringe patterns, two wrapped phases ( $\phi_h$  and  $\phi_l$ ) can be recovered and  $\phi_h$  can be unwrapped with respect to  $\phi_l$  according to two-frequency TPU approaches, such as hierarchical TPU [Eq. (95)] [237] (Fig. 28) and - (number theoretical TPU [111]. The associated fringe modulation for  $\phi_h$  and  $\phi_l$  can also be calculated by formulas similar to Eqs. (16) and (49). Since in bi-frequency phase shifting method, the high-frequency phase used for depth calculation is encoded by three individual phase-shifted fringes with full dynamic range, it is less affected by object motion compared with dual-frequency scheme. Recently, the bi-frequency phase shifting algorithm has been extended to the phase coding method by replacing the low-frequency phase  $\phi_l$  with a stair phase function  $\phi_s$  [167]. By this means, the total number of patterns required in phase shifting plus phase coding method can also be reduced from 6 to 5.

### 5.6. 2 + 2 phase shifting algorithm

The 2 + 2 phase shifting method proposed by Zuo et al. [109] uses only two  $\pi$ -shifted fringe images and two linearly increasing/decreasing slope intensities to reconstruct both a high-frequency wrapped phase map as well as a base phase map without any wraps. The intensities of the designed fringe images in the camera space are:

$$I_0^p(x^p, y^p) = a^p + b^p \cos(2\pi f_h^p x^p) \quad (115)$$

$$I_1^p(x^p, y^p) = a^p + b^p \sin(2\pi f_h^p x^p) \quad (116)$$

$$I_2^p(x^p, y^p) = a^p + b^p(2x^p/X - 1) \quad (117)$$

$$I_3^p(x^p, y^p) = a^p - b^p(2x^p/X - 1) \quad (118)$$

where  $X$  is the total number of pixels along each row of the projected patterns. Fig. 29(a) and (b) illustrate the pattern set for  $f_h^p = 16$ ,  $a^p = 0.5$ ,  $b^p = 0.5$ . The corresponding captured patterns are

$$I_0 = A + B \cos(\phi_h) \quad (119)$$

$$I_1 = A + B \sin(\phi_h) \quad (120)$$

$$I_2 = A + B\phi_b \quad (121)$$

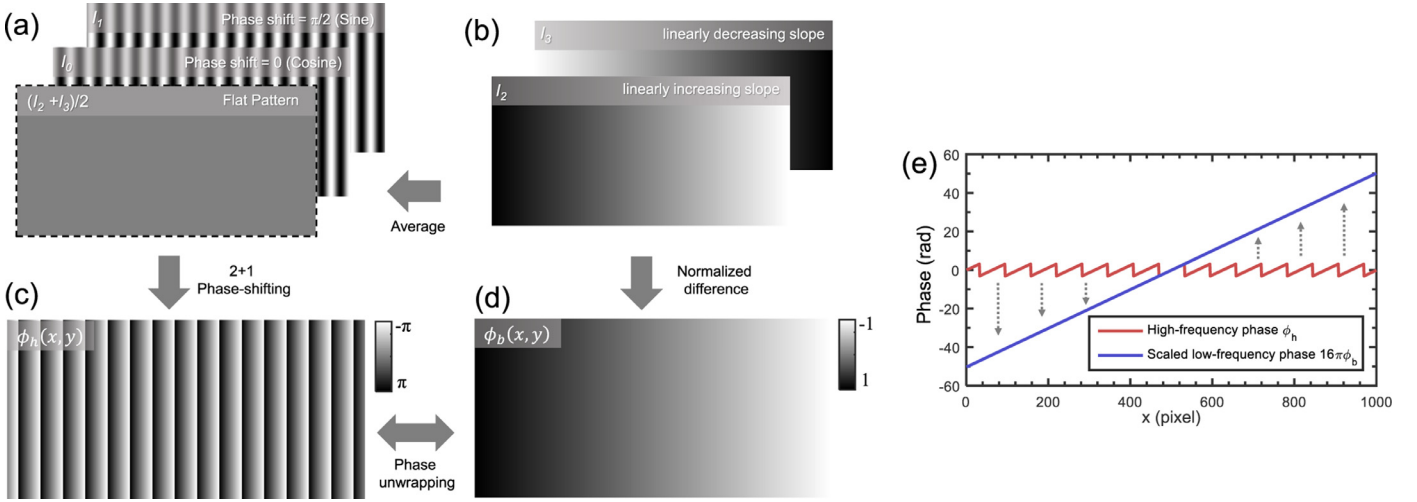


**Fig. 29.** Example of 2 + 2 phase shifting algorithm ( $f_h^p = 16$ ,  $f_b^p = 1$ ). (a) Two high-frequency patterns with  $\pi/2$  phase-shift; (b) two linearly increasing/decreasing slope images, an additional flat pattern shown in (a) can be obtained by averaging the two slope patterns; (c) retrieved high-frequency phase map  $\phi_h(x, y)$ ; (d) retrieved base phase map  $\phi_b(x, y)$ ; (e) the relation between the high-frequency wrapped phase  $\phi_h(x, y)$  and the scaled base phase  $16\pi\phi_b(x, y)$ .

$$I_3 = A - B\phi_b \quad (122)$$

where  $\phi_b$  is the so-called base phase with values ranging from  $[-1, 1]$ ,  $\phi_h$  is the high-frequency phase to be unwrapped. The average of  $I_2$  and  $I_3$  is just a flat image, which can be combined with  $I_0$  and  $I_1$  to constitute a 2 + 1 phase shifting pattern set, as demonstrated in Fig. 29. The high-frequency phase, average intensity, and intensity modulation can be solved by:

$$\phi_h = \tan^{-1} \frac{2I_1 - I_2 - I_3}{2I_0 - I_2 - I_3} \quad (123)$$

$$A = \frac{I_2 + I_3}{2} \quad (124)$$

$$B = \frac{\sqrt{(2I_1 - I_2 - I_3)^2 + (2I_0 - I_2 - I_3)^2}}{2} \quad (125)$$

The base phase can then be obtained by taking the normalized difference between  $I_2$  and  $I_3$

$$\phi_b = \frac{I_2 - I_3}{2B} \quad (126)$$

After obtaining two phases  $\phi_b$ , and  $\phi_h$  from these four captured images,  $\phi_b$  should be scaled to the same dynamic range of  $[-\pi, \pi]$  ( $\phi_i = \pi\phi_b$ ) and used as a reference to unwrap the high-frequency phase  $\phi_h$  based on two-frequency hierarchical TPU [Eq. (95)]. Similar to the 2 + 1 phase shifting algorithm, the high-frequency phase information in 2 + 2 PSP approach is encoded within only two fringe images, so it is less sensitive to motion-induced measurement error than other phase shifting algorithms, e.g. three-/four-step PSP. Besides, the base phase utilizes full dynamic range of two individual slope patterns, which provides improved unwrapping robustness compared to other 4-pattern schemes, as will be introduced below. The premise of the 2 + 2 PSP is that the two phases ( $\phi_h$  and  $\phi_b$ ) share the same intensity modulation  $B$ , so that we can further save one pattern compared with dual-frequency or bi-frequency phase shifting approach. This is only a reasonable assumption when the fringe frequency is not too high. When very high-frequency ( $> 20$  period) fringe patterns are used, the lens defocusing will attenuate the fringe contrast while the modulation of the slope signal will be less affected due to its very low frequency. Under this condition, the discrepancy in intensity modulation will make the phase wrapping process less unstable.

### 5.7. Coded phase shifting algorithm

The coded phase shifting (CPS) algorithm developed by Wissmann et al. [108] extends the conventional four-step PSP algorithm with embedded period information suited to assist the phase unwrapping process. The embedded period information does not change the phase obtained by the conventional four-step phase shifting algorithm but can be used to solve the phase ambiguity problem in the presence of discontinuous or isolated surfaces without extending the length of the pattern sequence. Based on this idea, the intensities of the designed fringe images in the projector space are:

$$I_0^p(x^p, y^p) = a^p + b^p[(1 - M) \cos(2\pi f_0^p x^p) + M p_0^p(x^p)] \quad (127)$$

$$I_1^p(x^p, y^p) = a^p + b^p[(1 - M) \cos(2\pi f_0^p x^p - \pi/2) + M p_1^p(x^p)] \quad (128)$$

$$I_2^p(x^p, y^p) = a^p + b^p[(1 - M) \cos(2\pi f_0^p x^p - \pi) + M p_2^p(x^p)] \quad (129)$$

$$I_3^p(x^p, y^p) = a^p + b^p[(1 - M) \cos(2\pi f_0^p x^p - 3\pi/2) + M p_3^p(x^p)] \quad (130)$$

where  $p_n^p(x^p)$  ( $n = 0, 1, 2, 3$ ) represents the period information that is embedded to the original sinusoidal waves, and the factor  $M$  determines the strength of the amplitude modulation of the embedded signal, e.g.  $M = 0.2$  resulting in 20% of the amplitude reserved for encoding the period information yet the remaining fringe amplitude is reduced to 80% to accommodate the phase. Due to the embedded signals, the projected patterns are no longer sinusoidal. The corresponding captured images are

$$I_0 = A + B_h \cos(\phi) + B_p p_0 \quad (131)$$

$$I_1 = A + B_h \cos(\phi - \pi/2) + B_p p_1 \quad (132)$$

$$I_2 = A + B_h \cos(\phi - \pi) + B_p p_2 \quad (133)$$

$$I_3 = A + B_h \cos(\phi - 3\pi/2) + B_p p_3 \quad (134)$$

where  $B_h$  and  $B_p$  are the intensity modulation functions of the high-frequency sinusoidal waves and the embedded signals, respectively. According to Eq. (5), the intensity modulation is directly proportional to the surface reflectivity  $\alpha(x, y)$  and the amplitude of the original signal,

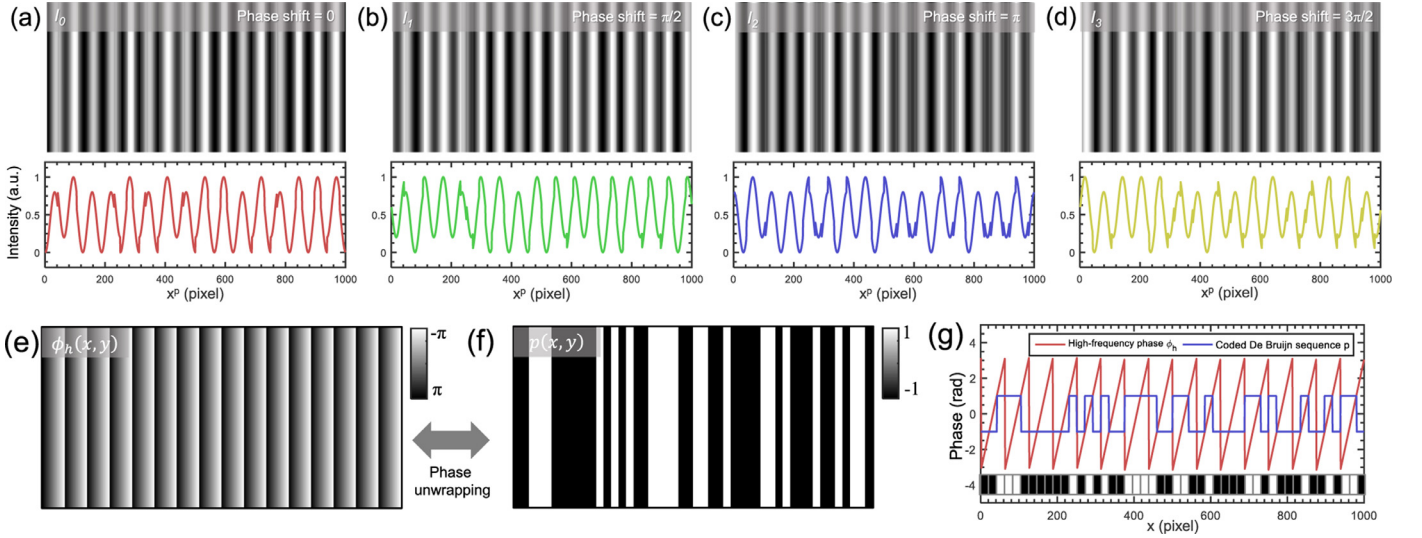


**Fig. 30.** Example of coded phase shifting patterns ( $f_h^p = 16$ ,  $a^p = 0.5$ ,  $b^p = 0.5$ ,  $M = 0.2$ ). (a–d) four-step coded phase shifting patterns and the corresponding intensity cross sections; (e) wrapped phase map  $\phi_h(x, y)$  retrieved by phase shifting algorithm; (f) decoded binary De Bruijn sequence  $p(x, y)$  (3 symbols per phase period, unique window length 7 symbols), (g) the relation between the wrapped phase  $\phi_h(x, y)$  and the decoded De Bruijn sequence  $p(x, y)$ .

so we have  $B_p \approx \frac{M}{1-M} B_h$  (neglecting the defocus-dependent modulation discrepancy). To guarantee that the phase retrieved by conventional four-step phase shifting algorithm [Eq. (21)]

$$\phi_h = \tan^{-1} \frac{I_1 - I_3}{I_0 - I_2} \quad (135)$$

is unaffected by the embedded signals, the coding functions should satisfy:

$$p_0^p(x^p) = p_2^p(x^p) \quad (136)$$

$$p_1^p(x^p) = p_3^p(x^p) \quad (137)$$

so that the coded information can be cancelled out in both the numerator and the denominator of Eq. (135). It has also been found that if the sign of the period information is alternated over the pattern sequence according to  $p^p(x^p) \equiv p_0^p(x^p) = -p_1^p(x^p) = p_2^p(x^p) = -p_3^p(x^p)$ , the average intensity and intensity modulation can be also calculated by the original equations [Eqs. (22) and (23)] without any modification

$$A = \frac{I_0 + I_1 + I_2 + I_3}{4} \quad (138)$$

$$B = \frac{1}{2} \sqrt{(I_1 - I_3)^2 + (I_0 - I_2)^2} \quad (139)$$

With all these parameters at hand, the embedded signal can be demodulated as:

$$p = \frac{(I_0 + I_2) - (I_1 + I_3)}{4B_p} \quad (140)$$

Then embedded signal is used to provide additional information about the fringe period and assist the phase unwrapping process. In CPS algorithm, Wissmann et al. [108] suggested to use a 1-dimensional (1D) binary De Bruijn sequence as the period signal. The designed coding function and the final waveforms of the 4 CPS patterns are illustrated in Fig. 30(a)–(d) ( $f_h^p = 16$ ,  $a^p = 0.5$ ,  $b^p = 0.5$ ,  $M = 0.2$ ). In this example, we use 3 symbols per phase period, and the unique window length is 7 symbols (each consecutive 7-symbol subsequence appear only once in the entire De Bruijn sequence) [Fig. 30(f)]. The fringe period is determined by correlating the wrapped phase map with the unambiguous codewords/symbol index reconstructed by using standard decoding precedence of De Bruijn sequences [Fig. 30(g)].

Since the CPS pattern contains many abrupt edges and discontinuities, it can be expected that the CPS method is strongly sensitive to

the defocus blur. Furthermore, since the codewords are determined by the neighborhood relation between adjacent sequence symbols, the decoding algorithm tends to be unstable around discontinuous and small isolated regions. Besides, the symbol extraction and tracing algorithm is relatively complicated and time-consuming, especially compared with conventional TPU approaches. It is also interesting to note that in the original demodulation equation proposed by Wissmann et al. (Eq. (6) in [108]), the intensity difference is normalized with respect to the average intensity  $A$  instead of the intensity modulation of the embedded signal  $B_p$ , so it does not account for the surface reflectivity correctly.

### 5.8. Period-coded phase shifting algorithm

The period-coded phase shifting (PCPS) algorithm developed by Wang et al. [107] shares the similar idea with the CPS algorithm and solves the unambiguous phase retrieval problem by embedding additional period signals into standard 4-step phase shifting patterns. However, instead of reducing the amplitude of the original sinusoidal waves, the embedded signals are wisely designed to be fitted in the “free space” of the conventional 4-step phase shifted waveforms. This allows to embed additional period signals without affecting the amplitude of the original sinusoidal component. The intensities of the PCPS fringe images in the projector space are:

$$I_0^p(x^p, y^p) = a^p + b^p \cos(2\pi f_0^p x^p) + p_0^p(x^p) \quad (141)$$

$$I_1^p(x^p, y^p) = a^p + b^p \cos(2\pi f_0^p x^p - \pi/2) + p_1^p(x^p) \quad (142)$$

$$I_2^p(x^p, y^p) = a^p + b^p \cos(2\pi f_0^p x^p - \pi) + p_2^p(x^p) \quad (143)$$

$$I_3^p(x^p, y^p) = a^p + b^p \cos(2\pi f_0^p x^p - 3\pi/2) + p_3^p(x^p) \quad (144)$$

where  $p_n^p(x^p)$  ( $n = 0, 1, 2, 3$ ) represents the coding functions added to the original sinusoidal waves. Compared with Eqs. (127)–(130), there is no factor  $M$  in the designed fringe image. Similarly, to guarantee that the phase retrieved by conventional 4-step PSP algorithm [Eq. (21)] is unaffected by the embedded signals,  $p_n^p(x^p)$  should satisfy:

$$p_0^p(x^p) = p_2^p(x^p) \quad (145)$$

$$p_1^p(x^p) = p_3^p(x^p) \quad (146)$$

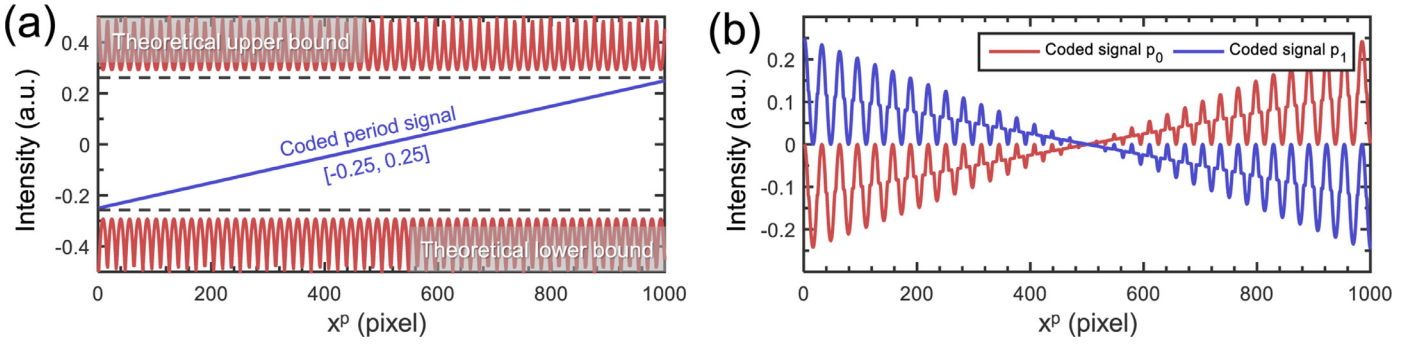


**Fig. 31.** (a) The ‘free’ dynamic range of 4-step phase shifted waveforms when  $f_h^p = 16$ . The period signal is designed within the range of  $[-0.25, 0.25]$ . (b) The designed coding signals for  $f_h^p = 16$ , where  $p_0 = p_2$ , and  $p_1 = p_3$ .

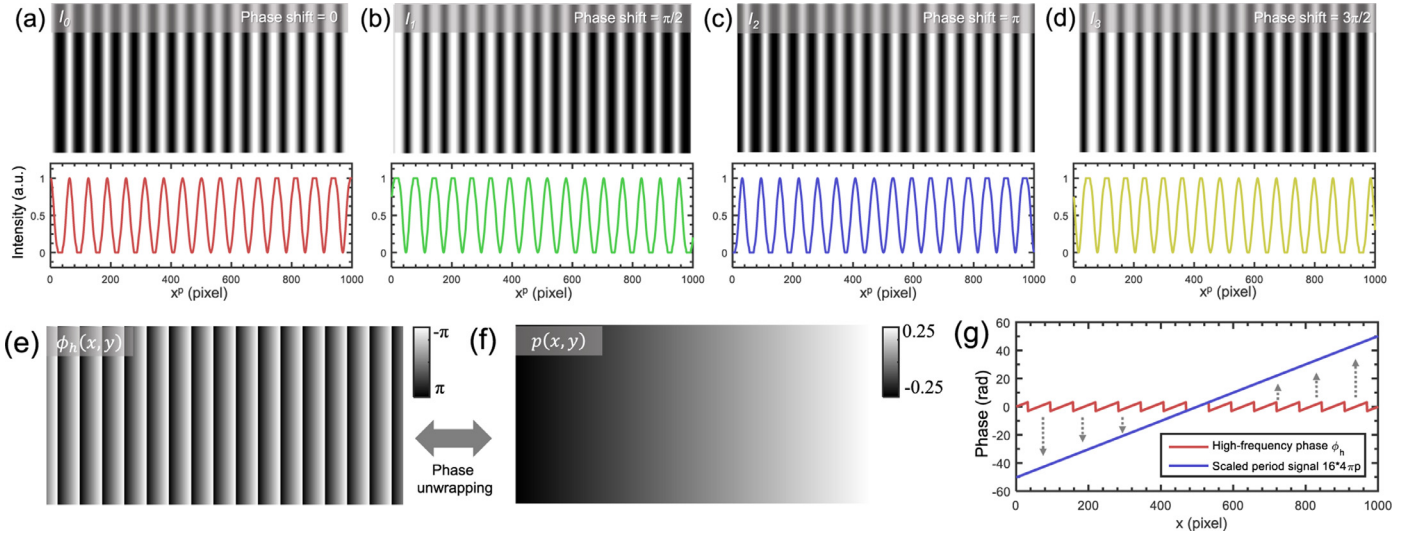


**Fig. 32.** Example of PCPS patterns. (a–d) four-step PCPS patterns and the corresponding intensity cross sections; (e) wrapped phase map  $\phi_h(x, y)$  retrieved by phase shifting algorithm; (f) decoded period signal  $p(x, y)$ ; (g) the relation between the wrapped phase  $\phi_h(x, y)$  and the decoded period signal  $p(x, y)$ .

After fringe projection and acquisition, the embedded period signal  $p(x)$  is also demodulated from the normalized intensity difference given by

$$p = \frac{(I_0 + I_2) - (I_1 + I_3)}{2B/b_p} \quad (147)$$

$$B = \frac{1}{2} \sqrt{(I_1 - I_3)^2 + (I_0 - I_2)^2} \quad (148)$$

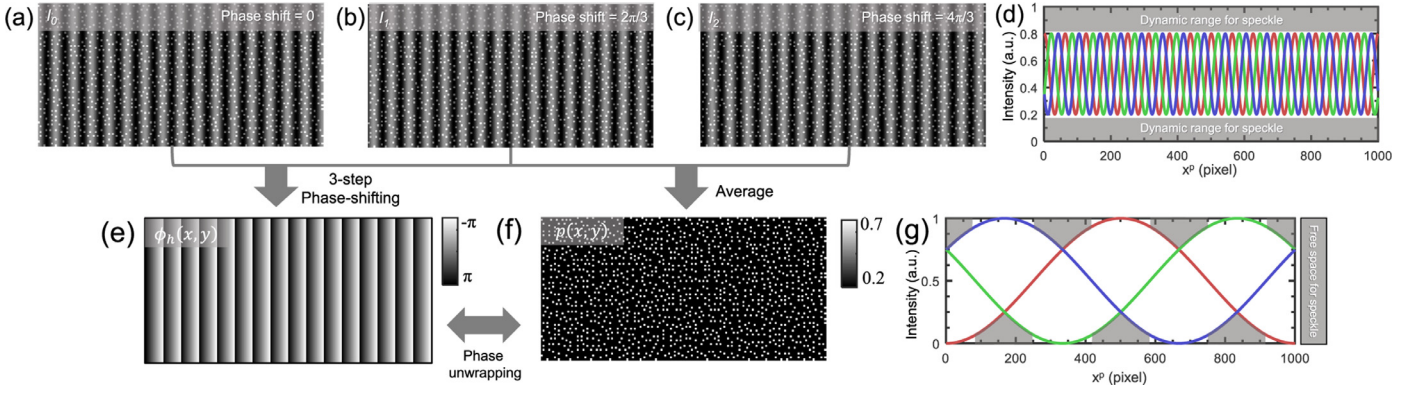
To simplify the decoding procedure and make full use of the remaining free dynamic range of the 4-step phase shifted waveforms, the coded period function is designed as a slope signal that has unique values along the  $x^p$  axis with a dynamic range of  $[-0.25, 0.25]$  [107]. This means the difference between  $p_0^p(x^p)$  and  $p_1^p(x^p)$  should be a linear slope signal, as shown in Fig. 31(a). Furthermore, the amplitude of the intensity waveform and the pattern entropy are also maximized in order to increase the SNR of the phase measurement [107]. The designed coded signals  $p_0^p(x^p)$  (for  $I_0^p$  and  $I_2^p$ ) and  $p_1^p(x^p)$  (for  $I_1^p$  and  $I_3^p$ ) are illustrated in Fig. 31(b). Note that since the alternating sign condition ( $p^p(x^p) \equiv p_0^p(x^p) = -p_1^p(x^p) = p_2^p(x^p) = -p_3^p(x^p)$ ) is no longer satisfied, the average intensity  $A$  of the fringe image cannot be retrieved.

Fig. 32(a)–(d) show the resultant 16-period PCPS patterns and their corresponding cross sections. After phase retrieval based on standard 4-step PSP [Eq. (21)] and embedded signal demodulation [Eq. (147)], the period signal  $p$  (slope function) obtained should also be scaled to  $[-\pi, \pi]$  ( $\phi_l = 4\pi p$ ) before being used to unwrap the high-frequency phase  $\phi_h$  based on two-frequency (hierarchical) TPU approach [Fig. 32(g)]. The

advantage of the PCPS approach lies in the fact that it effectively addresses the phase ambiguity problem without compromising the phase measurement accuracy of the conventional 4-step PSP. Besides, the pixel-wise decoding procedure is significantly simplified compared with the De Bruijn sequence used in CPS. However, the PCPS patterns also become no longer smooth due to the added coding signals, making it sensitive to lens defocusing. Besides, to ensure robust TPU, the number of sinusoidal periods is often restricted to a very small range ( $< 10$ ) due to the limited dynamic range of the (noisy) periodic signal, which limits the measurement accuracy. To unwrap a high-frequency phase with a larger number of periods (e.g. 16 as in [107]), additional spatial domain post-processing algorithms need to be used to further compensate phase unwrapping errors. It should be also noted that instead of embedding additional period signal into the fringe background as in CPS and PCPS, the amplitude of the fringe pattern ( $b^p$ ) can also be a spatially variant function to encode additional codewords for identifying the fringe order without affecting the wrapped phase, as recently demonstrated by Liu and Kofman [116].

### 5.9. Speckle-embedded phase shifting algorithm

Besides standard 4-step phase shifting, 3-step phase shifting patterns can also be served as the basis for embedding additional period signal in order to further reduce the number of required images. Since the average intensity will be canceled during the phase calculation, the direct current (DC) offset of fringe need not be a constant, which provides certain flexibility for signal coding in order to solve the phase ambiguity



**Fig. 33.** Example of speckle-embedded phase shifting patterns ( $f_h^p = 16$ ,  $a^p = 0.5$ ,  $b^p = 0.5$ ,  $M = 0.4$ ). (a–c) three-step speckle-embedded phase shifting patterns; (d) dynamic range for fringe and speckle ( $M = 0.4$ ); (e) wrapped phase map  $\phi_h(x, y)$  retrieved by 3-step phase shifting algorithm; (f) decoded speckle image by averaging the three fringe images; (g) free space for speckle signal in conventional 3-step phase shifted waveforms.

problem. Based on this idea, Zhang et al. [110,113] proposed to embed a fixed pseudorandom speckle signal  $p^p(x^p)$  into the original 3-step phase shifting sinusoidal waves. The 3 speckle-embedded fringe patterns are described as

$$I_0^p(x^p, y^p) = a^p + b^p[(1 - M) \cos(2\pi f_0^p x^p) + M p^p(x^p)] \quad (149)$$

$$I_1^p(x^p, y^p) = a^p + b^p[(1 - M) \cos(2\pi f_0^p x^p - 2\pi/3) + M p^p(x^p)] \quad (150)$$

$$I_2^p(x^p, y^p) = a^p + b^p[(1 - M) \cos(2\pi f_0^p x^p - 4\pi/3) + M p^p(x^p)] \quad (151)$$

where the factor  $M$  controls the relative strength of the amplitude modulation of the sinusoidal waves and embedded speckle signal. Fig. 33(a)–(c) shows the 3 speckle-embedded phase shifting patterns ( $f_h^p = 16$ ,  $a^p = 0.5$ ,  $b^p = 0.5$ ,  $M = 0.4$ ). In this example, the original binary speckle signal  $p^p(x^p)$  has the values of -1 (background) and 1 (speckle), and 40% of the pattern dynamic range is reserved for encoding this speckle signal [Fig. 33(d)].

Since the speckle signal is fixed in the three images, it can be effectively cancelled during the phase calculation by using standard 3-step PSP algorithm [Fig. 33(e)]:

$$\phi = \tan^{-1} \frac{\sqrt{3}(I_1 - I_2)}{2I_0 - I_1 - I_2} \quad (152)$$

While in the average intensity, the sinusoidal fringes are cancelled, leaving only background and the embedding speckle signal [Fig. 33(f)]

$$A = \frac{I_0 + I_1 + I_2}{3} \quad (153)$$

The phase unwrapping process follows the idea of patch based image matching used in the Kinect. The pseudorandom distribution of the speckle pattern guarantees uniqueness and high distinguishability within a local window, so the average intensity can be used for correlation-based image matching algorithm (with reference image taken with a planar surface at a proper distance) to determine the fringe order of the high-frequency unwrapped phase. Since the fringe order is an integer within  $[0, F-1]$ , at most  $F$  possible candidates need to be checked for each wrapped phase.

It should be also noted that similar to the previous PCPS method, if the amplitude of the speckle signal can be spatial variant and even be negative, it can be accommodated in the “free space” of conventional 3-step phase shifted waveforms without attenuating the dynamic range of the primarily sinusoidal component [110], as illustrated in Fig. 33(g). As can be seen, the margin of intensity dynamic range in three phase-shifted fringes is fully exploited in this way. The upper margin is used to embed positive speckle (brighter dots) while the lower margin is used to embed negative speckle (darker dots).

The speckle-embedded phase shifting algorithm uses the theoretical minimum of three images for phase shifting and absolute phase recovery, so it greatly facilitates the application of phase shifting in time-critical conditions. However, the accuracy of the phase unwrapping is still limited by the spatial coding strategy and is strongly sensitive to the intensity change of the speckle image caused by various degradation during image capture, e.g., deformation, resampling, attenuation, defocus, and surface reflectivity variations. So region-based processing (e.g. phase map segmentation, spatial phase unwrapping, and voting strategy) still needs to be used to produce a more reliable unwrapping result [110,113], which significantly increases the complexity of the reconstruction algorithm and may cause reliability issues in complex scenes. To overcome these limitations, Tao et al. [115] proposed to embed a triangular wave into the DC offset of original 3-step phase shifting patterns under the guidance of the number theory to ensure the uniqueness of the phase unwrapping problem. By combining the triangular wave information and the geometry constraint, the ambiguities in the high-frequency wrapped phase can be effectively removed based on a much simpler, less computationally intensive decoding algorithm.

### 5.10. Speckle-embedded Fourier transform algorithm

The idea of signal embedding is not just limited to conventional phase shifting algorithm. As demonstrated by Feng et al. [114], the flat pattern used in modified FTP (discussed in Section 3.8) can also be replaced by a speckle signal, which allows to solve the phase ambiguity without projecting additional patterns. This method, so called speckle-embedded FTP, can thus effectively address the high-frequency phase retrieval and the phase disambiguation problems with only two projected patterns. In the projector space, the two projected patterns are

$$I_0^p(x^p, y^p) = a^p + b^p[(1 - M) \cos(2\pi f_h^p x^p) + M p^p(x^p, y^p)] \quad (154)$$

$$I_1^p(x^p, y^p) = a^p + b^p M p^p(x^p, y^p) \quad (155)$$

where  $p^p(x^p, y^p)$  is the binary speckle signal with values of -1 (background) and 1 (speckle), the factor  $M$  controls the relative strength of the amplitude modulation of the sinusoidal wave and embedded speckle signal. Fig. 34(a)–(b) shows the two projected patterns with  $f_h^p = 16$ ,  $a^p = 0.5$ ,  $b^p = 0.5$ ,  $M = 0.4$ . As is shown, the first pattern is a speckle embedded fringe pattern while the other pattern is a just normal speckle pattern. The corresponding captured intensities in the camera space are

$$I_0(x, y) = A(x, y) + B(x, y) \cos[2\pi f_h x + \phi_0(x, y)] + B_p(x, y)p(x, y) \quad (156)$$

$$I_1(x, y) = A(x, y) + B_p(x, y)p(x, y) \quad (157)$$

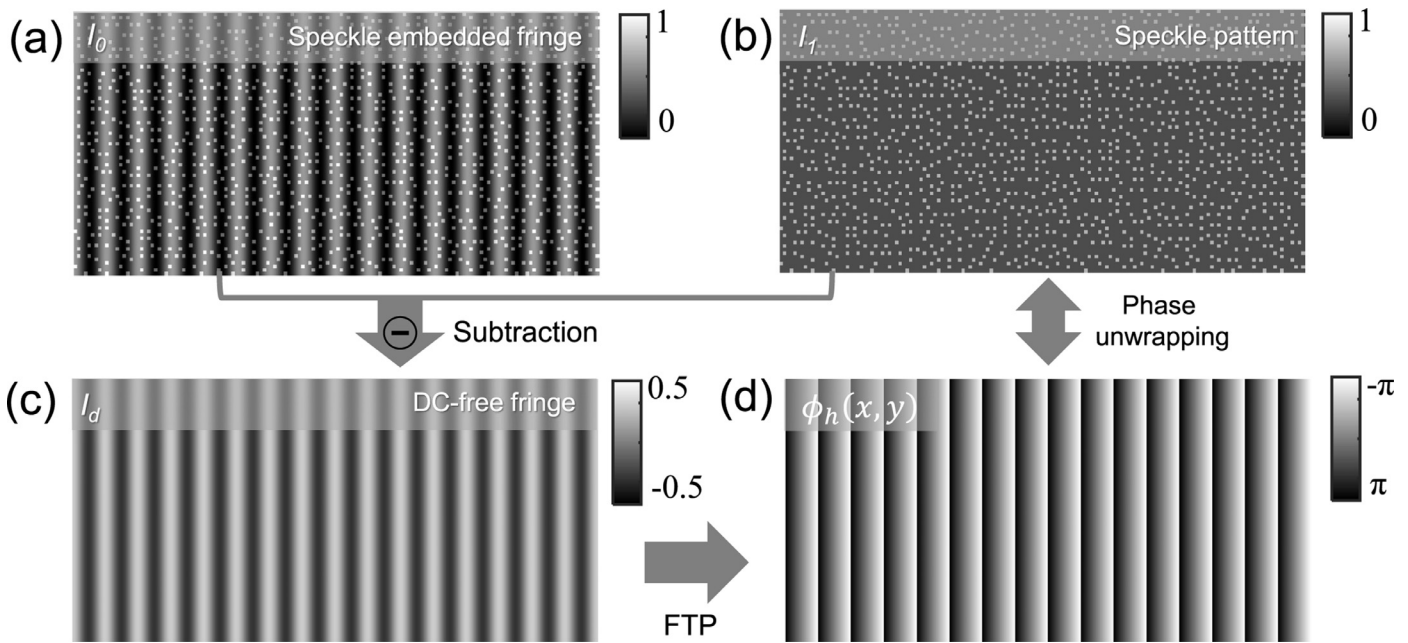


**Fig. 34.** Example of speckle-embedded FTP patterns. (a) Speckle-embedded fringe; (b) speckle fringe; (c) DC-free fringe image after subtraction; (d) high-frequency wrapped phase map  $\phi_h(x, y)$  retrieved by FTP algorithm, which can be unwrapped with the help of the speckle image  $I_1$  using correlation-based image matching algorithm.

By the subtraction of these two images, a DC-free sinusoidal fringe can be obtained with the background and the speckle signal effective cancelled [Fig. 34(c)]

$$I_d(x, y) = I_0 - I_1 = B(x, y) \cos[2\pi f_h x + \phi_0(x, y)] \quad (158)$$

Note here  $I_d$  is the same as the one in modified FTP [Eq. (69)], which further indicates that combining a spatially varying speckle signal within both the flat pattern and the sinusoidal pattern will not influence the phase extraction. The high-frequency phase can be extracted from  $I_d$  based on Fourier transform technique [Fig. 34(d)], and the additional speckle image  $I_0$  can be used for correlation-based image matching algorithm to determine the fringe order of the high-frequency phase. The speckle-embedded Fourier transform algorithm share the advantages of both modified FTP and speckle correlation-based phase unwrapping. Since only two images are involved to recover an unambiguous depth map, it is highly suitable for dynamic measurement of moving objects. Besides, it is insensitive to the object motion as the phase information is encoded within only single fringe image. However, the accuracy of phase unwrapping is strongly dependent on the quality of the speckle image, which may be unstable when measuring complicated surfaces, especially with large height and reflectivity variations or disturbed by partial discrete shadowing. Besides, the basic algorithms involved for phase retrieval and robust TPU, e.g. Fourier transform, speckle correlation, candidate searching, and median filtering, demand expensive computations, and thus have to be accelerated by graphics processing units (GPUs) to achieve better real-time performance [114].

## 6. Selection of PSP algorithms

In Sections 3 and 5, we have reviewed many different phase shifting algorithms, which can be used to reduce different types of phase error or realize TPU without projecting too many additional patterns. Because each algorithm has its own features and no single algorithm can meet all requirements in practical applications, selection of the most appropriate phase shifting algorithm for a specific phase shifting measurement system needs careful analysis and trade-off considerations. For the retrieval of only the wrapped phase (without requiring TPU), one can select the most suitable algorithm from those we reviewed in Section 3. And the

important characteristics of these algorithms are summarized in Fig. 35. Several observations are addressed as follows:

(a) Standard N-step PSP is the most widely used PSP algorithm due to its balanced performance and flexibilities in choosing phase shifting steps. It provides high measurement accuracy, good resistance to different error sources, and relatively low computational complexity. Increasing the phase shifting steps can obtain lower measurement uncertainty and better tolerance to intensity nonlinearity (saturation) error, but it requires longer fringe pattern sequences (acquisition time). So for the 3D shape measurement of static objects, using a large-step PSP algorithm is a simple yet very effective choice for achieving high-accuracy and robust measurements.

(b) Double three-step PSP is relatively insensitive to the intensity nonlinearity but requires three extra patterns to perform the additional three-step PSP, making it unsuitable for dynamic or real-time measurement. Hariharan 5-step PSP is relatively insensitive to phase shifting error and motion-induced phase error when the surface is moving in the  $z$  direction. However, it also require 5 fringe patterns (need two more patterns compared to 3-step PSP) and thus is still not ideal for the measurement of dynamic surfaces.

(c) By encoding the phase information only within two fringe images, the modified 2 + 1 PSP is less sensitive to motion-induced measurement error compared to conventional 3-step PSP. This property makes it appropriate for measuring moving or deforming surfaces. However, the resistance to noise and intensity nonlinearity induced phase error is also compromised compared to that of conventional 3-step PSP.

(d) Trapezoidal PSP and triangular PSP use the intensity-ratio directly rather than the phase. They are highly computationally efficient since there is no need to calculate the arctangent function as in conventional PSP. But they become more sensitive to lens defocusing and intensity nonlinearity because their sharp-edged intensity profiles. The triangular PSP uses only two patterns and thus is less sensitive to object motion. However, it becomes sensitive to surface reflectivity variations and cannot measure highly textured surfaces.

(e)  $\pi$ -shift FTP, modified FTP, and background-normalized FTP are actually FTP based approaches but with additional features of phase shifting or background elimination. They require relatively complicated

	Pattern count	Measurement uncertainty	Background intensity	Surface reflectivity variations	Lens defocusing	Intensity nonlinearity	Motion tolerance	Computational complexity
Standard N-Step PSP	$\geq 3$	✓	✓	✓	✓	⊖ (large step ✓)	⊖ (large step ✗)	✓
Double Three-Step PSP	6	✓	✓	✓	✓	✓	✗	⊖
Hariharan 5-step PSP	5	✓	✓	✓	✓	⊖	⊖	✓
Modified 2+1 PSP	3	⊖	✓	✓	✓	✗	✓	✓
Trapezoidal PSP	3	✓	✓	✓	✗	✗	⊖	✓ ✓
Triangular PSP	2	⊖	✓	✗	✗	✗	✓	✓ ✓
$\pi$ -shift FTP	2	✗	✓	✗	✓	⊖	✓	✗
Modified FTP	2	✗	✓	✗	✓	⊖	✓ ✓	✗
Background-normalized FTP	2	✗	✓	⊖	✓	⊖	✓ ✓	✗

Fig. 35. Comparative assessment of 9 phase shifting algorithms reviewed in Section 3. Green ✓, blue ⊖, and red ✗ indicate good, fair, and bad performance with respect to different properties. (For interpretation of the references to color in this figure legend, the reader is referred to the web version of this article).

frequency-domain processing and provide phase measurements with relatively low accuracy and spatial resolution. All these three algorithms use only two fringe patterns and thus are suitable for dynamic 3D measurement. Moreover, the modified FTP and background-normalized FTP are almost immune to motion artifacts since only a single fringe image is used to encode the phase information. Due to the additional normalization step, the background-normalized FTP can partially alleviate the spectrum leakage problem caused by large surface reflectivity variations.

For the measurement of complicated surfaces (e.g. spatially isolated objects or depth discontinuities), one should choose the phase shifting algorithms with the feature of absolute phase recovery or TPU, which have been reviewed in Section 5. Some important characteristics of these algorithms are summarized in Fig. 36. Several key observations can be made as follows:

(a) The PSP plus TPU (3+3 PSP) method is a simple and reliable approach for absolute phase recovery. It provides high unwrapping reliability and is insensitive to lens defocusing. But it requires at least 6 patterns (two separate 3-step phase shifting patterns) for obtaining two wrapped phases with different frequencies, making it relatively sensitive to object motion.

(b) The PSP plus Gray code approach requires even more (typically > 6) projected patterns for absolute phase recovery, making it unsuitable for high-speed or dynamic 3D shape measurement. It is also very sensitive to the image blur induced by lens defocusing. By encoding codewords into the phase component of the fringe, the PSP plus phase

coding approach employs 6 patterns to represent more fringe orders than the PSP plus Gray code approach, but it also suffers from the defocus-induced unwrapping error at the boundary between adjacent codewords.

(c) The dual-frequency PSP and bi-frequency PSP methods both use 5 patterns to recover two wrapped phases with different frequencies for absolute phase retrieval. In dual-frequency PSP, both low- and high-frequency patterns are superimposed and sharing the dynamic range of 5 phase-shifted patterns, so it can theoretically obtain better measurement accuracy (comparable to that of 5-step PSP). While in bi-frequency PSP method, the both low- and high-frequency phase information used for phase unwrapping and depth calculation are encoded by individual phase-shifted fringes (3 and 2) with full dynamic range, so it has better reliability of phase unwrapping and is also less affected by the object motion.

(d) The 2+2 PSP, CPS, and PCPS are all 4-pattern based absolute phase retrieval approaches. As an extension to the modified 2+1 phase shifting algorithm, the 2+2 PSP method is less sensitive to the motion-induced measurement error since the high-frequency phase information is encoded within only two fringe images. The decoding algorithm is pixel-wise, computationally simple, and compatible to standard TPU methods. However, it is slightly sensitive to lens defocusing (due to the discrepancy in intensity modulation for the base phase and high-frequency phase), and the measurement uncertainty is slightly compromised compared to other 4-pattern approaches. The CPS and PCPS methods embed additional period signals into standard 4-step phase shifting

	Pattern count (for typical 20- period fringes)	Measurement uncertainty	Unwrapping reliability	Lens defocusing	Motion tolerance	Computational complexity
PSP+TPU	3+3	✓	✓ ✓	✓	✗	✓
PSP+Gray code	3+5	✓	✓	✗	✗	✓
PSP+phase coding	3+3	✓	✓	✗	✗	✓
Dual- frequency PSP	5	✓ ✓	✓	✓	✗	✓
Bi-frequency PSP	5	✓	✓ ✓	✓	–	✓
2+2 PSP	4	–	✓	–	✓	✓
CPS	4	✓	✓	✗	–	✗
PCPS	4	✓	– ( w/ spatial domain post-processing ✓ )	✗	–	✓ ( w/ spatial domain post-processing – )
Speckle- embedded PSP	3	✓	✓	–	✓	✗
Speckle- embedded FTP	2	✗	✓	–	✓ ✓	✗

Fig. 36. Comparative assessment of 10 phase shifting algorithms for absolute phase recovery reviewed in Section 5. Green ✓, blue –, and red ✗ indicate good, fair, and bad performance with respect to different properties. (For interpretation of the references to color in this figure legend, the reader is referred to the web version of this article).

patterns, so they can obtain better measurement accuracy (especially for the PCPS, it can achieve the same phase measurement accuracy as conventional 4-step PSP theoretically). Besides, since the modified intensity profiles contain abrupt edges and discontinuities, the CPS and PCPS methods are also sensitive to defocus blur. In order to achieve ro-

bust phase unwrapping, the decoding algorithms of CPS and PCPS are also more complicated and time-consuming due to the involvement of spatial domain processing (De Bruijn sequence demodulation and spatial domain compensation).

(e) The speckle-embedded PSP and speckle-embedded FTP methods address the phase ambiguity problem by embedding a speckle signal into conventional 3-step PSP patterns and modified FTP patterns, respectively. They require less pattern projections, and thus are highly suitable for measuring dynamic scenes. Moreover, the speckle-embedded FTP method requires only 2 patterns and only a single fringe image is used to encode the phase information, which makes it rather insensitive to object motion. However, the FTP-based algorithms can only provide phase measurements with relatively low depth accuracy and spatial resolution. Besides, the speckle correlation and related decoding algorithms also require expensive computations, and thus the real-time implementation of the speckle-embedded PSP and speckle-embedded FTP methods is still quite challenging.

## 7. Further discussions

It should be mentioned that improving the measurement accuracy, pattern efficiency, and robustness to different types of errors is the permanent objective for the future development of PSP algorithms. As we discussed in Section 4, using more fringe patterns is the most direct way to get improved measurement accuracy and robustness, while reducing the pattern count is the key factor to achieve high efficiency measurement, which is particularly important for high-speed, real-time 3D shape measurement applications. This section further discusses three important issues regarding improving the measurement accuracy and efficiency of PSP techniques: further reducing the number of patterns, phase-depth sensitivity, and computational efficiency.

### 7.1. Further reducing the number of patterns

As we reviewed in Section 5, researchers are always in pursuit of minimizing the number of patterns for efficient phase detection and unwrapping. But by doing so, it is also quite challenging to increase the sensitivity of the measurement to noise and other distortions. To alleviate this problem, an important common characteristic of these approaches is that they introduce a low-frequency phase/period signal/speckle pattern into the projected pattern set such that phase demodulation involves extracting two terms with one serving as the phase unwrapping reference and the other high-frequency phase serving as a noise-resilient term for 3D reconstruction. For traditional two-frequency PSP, it involves at least 6 patterns to retrieve two groups of phases. However, according to the image formation model of FPP introduced in Section 2, there is certain information redundancy in the average intensity and the intensity modulation of the fringe images, which can be effectively utilized to encode additional period information without affecting the phase calculation, reducing the number of patterns to 5 [106,111], 4 [107–109,116], 3 [113–115], and even 2 based on FTP approach [114]. Furthermore, additional priori knowledge, e.g. the environment ambient light is changing slowly on the object's surface, may be explored to further reduce the number of patterns in PSP while maintaining the robustness to the environment light and reflectivity of the scene.

#### 7.1.1. Frequency multiplexing

All PSP strategies reviewed in Section 3 and Section 5 are based on spatial multiplexing or time multiplexing techniques with use of at least two fringe patterns. However, it should also be noticed that frequency multiplexing techniques have been proposed to effectively reduce the pattern count or even realize single-shot PSP or TPU [80,238–240]. Guan et al. [238] proposed a frequency multiplexing PSP pattern named composite pattern, in which 4 unit-frequency phase shifting patterns are spatially modulated by different carrier frequencies along the orthogonal dimension and combined into a single pattern. The 4 individual patterns can then be demodulated by applying appropriate band-pass filters in the frequency domain. Based on the similar idea, Yue et al. [240] proposed a single-shot  $\pi$ -shift FTP scheme by generating a composite pattern with two  $\pi$ -shifted fringes. By combining two sinusoidal

fringes with different two-component carrier frequencies into one pattern, Takeda et al. [80] proposed a single-shot two-frequency FTP technique to realize both phase retrieval and number-theoretical TPU. Similarly, Sansoni and Redaelli [239] presented a one-shot two-frequency TPU method by directly overlapping two sinusoidal gratings at different frequencies. Since the phase ambiguity problem can be addressed by introducing two phase components, these two approaches are suitable for measuring objects having discontinuities and spatially isolated surfaces [80,239]. Although these single-shot frequency multiplexing methods can achieve a high-quality 3D reconstruction in theory or simulation. In practice, due to limited band width and gray-level quantization of both the projector and the camera, they tend to produce measurement results with low spatial resolution and poor depth accuracy.

#### 7.1.2. Geometric constraint

Though not discussed in this review, geometry constraint based approaches are also very efficient to solve the phase ambiguity problem for measuring complex surfaces without requiring additional projection patterns [115,116,121,128,241–249]. Based on the projector-camera system geometry, several candidate points are selected based on the phase value along the epipolar line, and correspondence search is performed within a small range for each point on the object surface. If the measured objects are known to be placed within certain depth measurement volume, depth constraint can also be applied to rejecting some false candidates falling out of the measurement range [128,242,243,245]. Since the phase unwrapping procedure can be effectively bypassed, any phase shifting algorithms reviewed in Section 3 can be combined with geometry-constraint based approaches to realize absolute phase measurement. Thus, it also allows us to develop several new measurement schemes with 3 or even less than 3 patterns for the measurement of complicated surfaces. However, since the number of candidate corresponding points would be very high if high-frequency patterns were used, these geometry-constraint based methods are normally designed with a low fringe frequency in order to minimize the number of candidate points [115,116]. To realize high-precision measurement based on high-frequency patterns, more cameras can be involved to enforce a tighter geometry constraint and guarantee the unique correspondence [249]. Besides, phase shifting algorithms for absolute phase recovery reviewed in Section 5 can also be combined with geometry constraint based approaches to achieve higher measurement accuracy by using high-fringe-density patterns [247,248], or obtain better reliability of phase unwrapping [115,116,167].

#### 7.2. Phase-depth sensitivity

This review mainly focuses on improving the phase measurement accuracy, efficiency, and robustness based on PSP techniques. However, it should be mentioned that high-quality phase measurements do not necessarily produce accurate 3D reconstruction results. The calibration method and the model used to convert an absolute phase map to a 3D point cloud are also critical for accurate 3D measurement. Numerous system calibration techniques for FPP have been proposed, which generally involve both camera calibration and projector calibration [250–260]. Camera calibration is a well-known and well-studied problem in computer vision. Considering the projector as an inverse camera, projector calibration is often performed based on the same optic model as the camera with the help of a pre-calibrated camera. For a lens with large distortion (which may be a combination of magnification errors, field curvature, as well as geometric optical distortion), there is no way to obtain accurate results without considering the distortion parameters during the calibration [253,257,260]. Precision of the target, quality of the calibration setup, and calibration model including both selected intrinsic and extrinsic parameters all contribute to the calibration results.

Another important factor influencing the measurement accuracy of FPP is the phase-depth sensitivity, which characterizes how markedly

the depth variations induce phase changes or fringe distortions. Obviously, a higher phase sensitivity is desirable because the phase error leads to smaller errors in the final measurement results. The phase-depth sensitivity is strongly dependent on the geometry of the measurement system. Besides, as discussed in Section 4.1, the fringe frequency is also a critical factor for determining the phase-depth sensitivity and using fringes with small pitches is helpful for improving the phase-depth sensitivity. But for a measurement system with fixed geometry and fringe frequency, the fringe orientation is the dominant factor affecting the phase-depth sensitivity. Wang and Zhang [261] indicated that simply projecting horizontal or vertical fringe patterns is not the best choice for obtaining optimal phase-depth sensitivity in FPP. They also proposed a method to determine the optimal fringe angle by projecting a set of horizontal and vertical fringe patterns onto a step-height object. Zhou et al. [262] further analyzed the relation between fringe angle and the sensitivity, and suggested an optimal direction of fringes perpendicular to the projector camera baseline of the measurement system. Recently, Zhang et al. [263] gave a strict analysis about the dependence of the phase sensitivities on the fringe directions by use of the epipolar geometry. They found that the optimal fringes should be the circular fringes centered at the epipole straight lines, and simply using conventional straight fringes can only provide sub-optimal solutions.

### 7.3. Computational efficiency

Besides reducing the pattern count, the efficient computation of PSP algorithms is also essential to achieve high-speed, real-time 3D shape measurement. It can be found that most of the PSP algorithms involve the arctangent function for the phase calculation, which is computationally time-consuming and poses a major obstacle to real-time implementation [95,106,264]. Though using intensity-ratio-based approaches, such as trapezoidal PSP and triangular PSP, can effectively bypass this problem, they are less tolerant to lens defocusing and intensity nonlinearity than conventional PSP. To overcome this speed bottleneck, Zhang and Huang [95] proposed a fast three-step PSP algorithm, which replaces the calculation of the arctangent function with the intensity ratio calculation. The phase error caused by this replacement is further compensated for by use of a lookup table (LUT). Guo and Liu [264] presented a general method for approximating the arctangent function with a piecewise-defined function, which significantly improves the efficiencies for phase evaluations. Liu et al. [106] developed a LUT-based implementation of PSP algorithms that account for every possible combination of captured pixel values over the pattern set while storing double-precision results. For 8-bit cameras, the LUT-based processing is highly efficient and completely lossless. Another speed bottleneck for high-speed, real-time measurement lies in the 3D reconstruction process, which involves computationally time-consuming matrix operations for converting phase to 3D coordinates. Zhang et al. [265] accelerated the absolute 3D coordinates mapping with matrix operations by means of GPU processing. The GPU can quickly compute each 3D coordinate for each point in parallel, in lieu of sequentially as with the CPU [266]. By expanding the matrix operations including matrix inverse and matrix multiplication carefully, Liu et al. [106] also suggested a LUT-based implementation of matrix computation for 3-D coordinates reconstruction. The LUT-based approach can speed up the computation by nearly 10 times without resorting to special hardware such as GPU.

## 8. Conclusions

In this article, we provide an exhaustive and comprehensive survey of phase shifting techniques used for 3D measurement of object surfaces. The image formation model for FPP has been presented as a basis for designing and understanding different PSP techniques. We have also reviewed a large number of state-of-the-art phase shifting algorithms for implementing 3D surface profilometry. These existing techniques have been classified into two groups by considering whether they are

able to recover the absolute phase instead of the wrapped phase. For PSP algorithms reviewed in Section 3, only wrapped phase map containing the modulo  $2\pi$  discontinuities can be recovered. However, for PSP algorithms with capability of absolute phase recovery reviewed in Section 5, they solve the phase ambiguity problem with the built-in TPU algorithm, and thus can be directly used to measure spatially isolated objects and complicated surfaces. It is important to note that this article, by no means, covers all PSP algorithms that have been developed and utilized, but it serves as a reference for readers to understand some of the popular PSP algorithms and to learn about their typical properties.

Several error sources of the phase measurement in a typical PSP system have been analyzed and reviewed, and the corresponding solutions have been discussed. This allows us to discuss the advantages and constraints of each phase shifting strategy from the points of view of measurement accuracy, coding efficiency, and resistance to different types of phase errors. This article also provides a useful guide for easily finding the most suitable PSP algorithm for a given application.

## Acknowledgments

This work was supported by the National Key R&D Program of China (2017YFF0106403), National Natural Science Fund of China (61722506, 61705105, 111574152), Final Assembly ‘13th Five-Year Plan’ Advanced Research Project of China (30102070102), Equipment Advanced Research Fund of China (61404150202), Outstanding Youth Foundation of Jiangsu Province of China (BK20170034), National Defense Science and Technology Foundation of China (0106173), ‘Six Talent Peaks’ project of Jiangsu Province, China (2015-DZXX-009), ‘333 Engineering’ Research Project of Jiangsu Province, China (BRA2016407), Fundamental Research Funds for the Central Universities (30917011204, 30916011322), China Postdoctoral Science Foundation (2017M621747), and Jiangsu Planned Projects for Postdoctoral Research Funds (1701038A).

## References

- [1] Bak D. Rapid prototyping or rapid production? 3D printing processes move industry towards the latter. *Assem Autom* 2003;23(4):340–5.
- [2] Dagli CH. Artificial neural networks for intelligent manufacturing. Springer Science & Business Media; 2012.
- [3] Burdea Grigore C, Coiffet P. Virtual reality technology. London: Wiley-Interscience; 1994.
- [4] Stanco F, Battiato S, Gallo G. Digital imaging for cultural heritage preservation: analysis, restoration, and reconstruction of ancient artworks. CRC Press; 2011.
- [5] Honrado CP, Larrabee Jr WF. Update in three-dimensional imaging in facial plastic surgery. *Curr Opin Otolaryngol Head Neck Surg* 2004;12(4):327–31.
- [6] Sansoni G, Trebeschi M, Docchio F. State-of-the-art and applications of 3D imaging sensors in industry, cultural heritage, medicine, and criminal investigation. *Sensors* 2009;9(1):568–601.
- [7] Curless B. From range scans to 3D models. *ACM SIGGRAPH Comput Graph* 1999;33(4):38–41.
- [8] Hocken RJ, Pereira PH. Coordinate measuring machines and systems. CRC Press; 2016.
- [9] Hariharan P. Optical interferometry. Academic press; 2003.
- [10] Kemaq Q. Two-dimensional windowed fourier transform for fringe pattern analysis: principles, applications and implementations. *Opt Lasers Eng* 2007;45(2):304–17.
- [11] Malacara Z, Servin M. Interferogram analysis for optical testing. 84. CRC press; 2016.
- [12] Foix S, Alenya G, Torras C. Lock-in time-of-flight (ToF) cameras: a survey. *IEEE Sens J* 2011;11(9):1917–26.
- [13] Cui Y, Schuon S, Chan D, Thrun S, Theobalt C. 3D shape scanning with a time-of-flight camera. In: 2010 IEEE Computer Society Conference on Computer Vision and Pattern Recognition; 2010. p. 1173–80. doi:10.1109/CVPR.2010.5540082.
- [14] Marr D, Poggio T. A computational theory of human stereo vision. *Proc R Soc Lond B: Biol Sci* 1979;204(1156):301–28. doi:10.1098/rspb.1979.0029.
- [15] Cochran SD, Medioni G. 3D surface description from binocular stereo. *IEEE Trans Pattern Anal Mach Intell* 1992;14(10):981–94.
- [16] Pentland AP. A new sense for depth of field. *IEEE Trans Pattern Anal Mach Intell* 1987;9(4):523–31.
- [17] Nayar SK, Nakagawa Y. Shape from focus. *IEEE Trans Pattern Anal Mach Intell* 1994;16(8):824–31.
- [18] Favaro P, Soatto S. A geometric approach to shape from defocus. *IEEE Trans Pattern Anal Mach Intell* 2005;27(3):406–17.
- [19] Boyer KL, Kak AC. Color-encoded structured light for rapid active ranging. *IEEE Trans Pattern Anal Mach Intell* 1987;PAMI-9(1):14–28.

- [20] Zhang L, Curless B, Seitz SM. Rapid shape acquisition using color structured light and multi-pass dynamic programming. In: First international symposium on 3D data processing visualization and transmission; 2002. p. 24–36. doi:10.1109/TD-PVT.2002.1024035.
- [21] Scharstein D, Szeliski R. High-accuracy stereo depth maps using structured light. In: Proceedings of the 2003 IEEE computer society conference on computer vision and pattern recognition; 2003. p. 195–202. doi:10.1109/CVPR.2003.1211354.
- [22] Geng J. Structured-light 3D surface imaging: a tutorial. *Adv Opt Photon* 2011;3(2):128–60.
- [23] Chen F, Brown GM, Song M. Overview of 3D shape measurement using optical methods. *Opt Eng* 2000;39(1):10–23.
- [24] Blais F. Review of 20 years of range sensor development. *J Electron Imaging* 2004;13(1):231–44.
- [25] Gorthi SS, Rastogi P. Fringe projection techniques: whither we are? *Opt Lasers Eng* 2010;48(IMAC-REVIEW-2009-001):133–40.
- [26] Salvi J, Fernandez S, Pribanic T, Llado X. A state of the art in structured light patterns for surface profilometry. *Pattern Recognit* 2010;43(8):2666–80.
- [27] Salvi J, Pages J, Batlle J. Pattern codification strategies in structured light systems. *Pattern Recognit* 2004;37(4):827–49.
- [28] Su X, Zhang Q. Dynamic 3D shape measurement method: a review. *Opt Lasers Eng* 2010;48(2):191–204.
- [29] Zhang S. Recent progresses on real-time 3D shape measurement using digital fringe projection techniques. *Opt Lasers Eng* 2010;48(2):149–58.
- [30] Zhang Z. Review of single-shot 3D shape measurement by phase calculation-based fringe projection techniques. *Opt Lasers Eng* 2012;50(8):1097–106.
- [31] Van der Jeught S, Dirckx JJ. Real-time structured light profilometry: a review. *Opt Lasers Eng* 2016;87:18–31.
- [32] Pages J, Salvi J, Collewet C, Forest J. Optimised De Bruijn patterns for one-shot shape acquisition. *Image Vis Comput* 2005;23(8):707–20.
- [33] Maruyama M, Abe S. Range sensing by projecting multiple slits with random cuts. *IEEE Trans Pattern Anal Mach Intell* 1993;15(6):647–51.
- [34] Ito M, Ishii A. A three-level checkerboard pattern (TCP) projection method for curved surface measurement. *Pattern Recognit* 1995;28(1):27–40.
- [35] Morita H, Yajima K, Sakata S. Reconstruction of surfaces of 3D objects by M-array pattern projection method. In: Proceedings of the second international conference on computer vision; 1988. p. 468–73. doi:10.1109/CCV.1988.590025.
- [36] Posdamer JL, Altschuler M. Surface measurement by space-encoded projected beam systems. *Comput Graph Image Process* 1982;18(1):1–17.
- [37] Caspi D, Kiryati N, Shamir J. Range imaging with adaptive color structured light. *IEEE Trans Pattern Anal Mach Intell* 1998;20(5):470–80.
- [38] Sansoni G, Corini S, Lazzari S, Rodella R, Docchio F. Three-dimensional imaging based on gray-code light projection: characterization of the measuring algorithm and development of a measuring system for industrial applications. *Appl Opt* 1997;36(19):4463–72.
- [39] Je C, Lee SW, Park RH. High-contrast color-stripe pattern for rapid structured-light range imaging. In: European conference on computer vision. Springer; 2004. p. 95–107.
- [40] Geng ZJ. Rainbow three-dimensional camera: new concept of high-speed three-dimensional vision systems. *Opt Eng* 1996;35(2):376–84.
- [41] Takasaki H. Moiré topography. *Appl Opt* 1970;9(6):1467–72.
- [42] Meadows D, Johnson W, Allen J. Generation of surface contours by moiré patterns. *Appl Opt* 1970;9(4):942–7.
- [43] Halioua M, Krishnamurthy R, Liu H, Chiang F. Projection moiré with moving gratings for automated 3D topography. *Appl Opt* 1983;22(6):850–5.
- [44] Harding KG, Harris JS. Projection moiré interferometer for vibration analysis. *Appl Opt* 1983;22(6):856–61.
- [45] Pirodda L. Shadow and projection moiré techniques for absolute or relative mapping of surface shapes. *Opt Eng* 1982;21(4):2146–40.
- [46] Yoshizawa T, Tomisawa T. Shadow moiré topography by means of the phase-shift method. *Opt Eng* 1993;32(7):1668–75.
- [47] Jin L, Koderia Y, Yoshizawa T, Otani Y. Shadow moiré profilometry using the phase-shifting method. *Opt Eng* 2000;39(8):2119–24.
- [48] Asundi A. Computer aided moiré methods. *Opt Lasers Eng* 1993;18(3):213–38.
- [49] Su X, Chen W. Fourier transform profilometry: a review. *Opt Lasers Eng* 2001;35(5):263–84.
- [50] Kemao Q. Windowed fourier transform for fringe pattern analysis. *Appl Opt* 2004;43(13):2695–702.
- [51] Zhong J, Weng J. Spatial carrier-fringe pattern analysis by means of wavelet transform: wavelet transform profilometry. *Appl Opt* 2004;43(26):4993–8.
- [52] Huang L, Kemao Q, Pan B, Asundi AK. Comparison of fourier transform, windowed fourier transform, and wavelet transform methods for phase extraction from a single fringe pattern in fringe projection profilometry. *Opt Lasers Eng* 2010;48(2):141–8.
- [53] Zhang Z, Jing Z, Wang Z, Kuang D. Comparison of fourier transform, windowed fourier transform, and wavelet transform methods for phase calculation at discontinuities in fringe projection profilometry. *Opt Lasers Eng* 2012;50(8):1152–60.
- [54] Srinivasan V, Liu HC, Halioua M. Automated phase-measuring profilometry of 3D diffuse objects. *Appl Opt* 1984;23(18):3105–8.
- [55] Halioua M, Krishnamurthy RS, Liu HC, Chiang FP. Automated 360° profilometry of 3D diffuse objects. *Appl Opt* 1985;24(14):2193–6.
- [56] Bruning JH, Herriott DR, Gallagher J, Rosenfeld D, White A, Brangaccio D. Digital wavefront measuring interferometer for testing optical surfaces and lenses. *Appl Opt* 1974;13(11):2693–703.
- [57] Malacara D. Optical shop testing, 59. John Wiley & Sons; 2007.
- [58] Goldstein RM, Zebker HA, Werner CL. Satellite radar interferometry: two-dimensional phase unwrapping. *Radio Sci* 1988;23(4):713–20.
- [59] Su X, Chen W. Reliability-guided phase unwrapping algorithm: a review. *Opt Lasers Eng* 2004;42(3):245–61.
- [60] Flynn TJ. Two-dimensional phase unwrapping with minimum weighted discontinuity. *J Opt Soc Am A* 1997;14(10):2692–701.
- [61] Ghiglia DC, Romero LA. Minimum Lp-norm two-dimensional phase unwrapping. *J Opt Soc Am A* 1996;13(10):1999–2013.
- [62] Judge TR, Bryanston Cross P. A review of phase unwrapping techniques in fringe analysis. *Opt Lasers Eng* 1994;21(4):199–239.
- [63] Ghiglia DC, Pritt MD. Two-dimensional phase unwrapping: theory, algorithms, and software, 4. Wiley New York; 1998.
- [64] Zappa E, GBusca. Comparison of eight unwrapping algorithms applied to fourier-transform profilometry. *Opt Lasers Eng* 2008;46(2):106–16.
- [65] Zebker HA, Lu Y. Phase unwrapping algorithms for radar interferometry: residue-cut, least-squares, and synthesis algorithms. *J Opt Soc Am A* 1998;15(3):586–98.
- [66] Zhao M, Huang L, Zhang Q, Su X, Asundi A, Kemao Q. Quality-guided phase unwrapping technique: comparison of quality maps and guiding strategies. *Appl Opt* 2011;50(33):6214–24.
- [67] Sansoni G, Carocci M, Rodella R. Three-dimensional vision based on a combination of gray-code and phase-shift light projection: analysis and compensation of the systematic errors. *Appl Opt* 1999;38(31):6565–73.
- [68] Huntley JM, Saldner H. Temporal phase-unwrapping algorithm for automated interferogram analysis. *Appl Opt* 1993;32(17):3047–52.
- [69] Zhao H, Chen W, Tan Y. Phase-unwrapping algorithm for the measurement of three-dimensional object shapes. *Appl Opt* 1994;33(20):4497–500.
- [70] Cheng YY, Wyant JC. Two-wavelength phase shifting interferometry. *Appl Opt* 1984;23(24):4539–43.
- [71] Creath K, Cheng YY, Wyant JC. Contouring aspheric surfaces using two-wavelength phase-shifting interferometry. *Opt Acta: Int J Opt* 1985;32(12):1455–64.
- [72] Gushov V, Solodkin YN. Automatic processing of fringe patterns in integer interferometers. *Opt Lasers Eng* 1991;14(4-5):311–24.
- [73] Burke J, Bothe T, Osten W, Hess CF. Reverse engineering by fringe projection, 4778. International Society for Optics and Photonics; 2002. p. 312–25.
- [74] Ding Y, Xi J, Yu Y, Chicharo J. Recovering the absolute phase maps of two fringe patterns with selected frequencies. *Opt Lett* 2011;36(13):2518–20.
- [75] Falaggis K, Towers DP, Towers CE. Algebraic solution for phase unwrapping problems in multiwavelength interferometry. *Appl Opt* 2014;53(17):3737–47.
- [76] Petković T, Pribanić T, Djonlić M. Temporal phase unwrapping using orthographic projection. *Opt Lasers Eng* 2017;90:34–47.
- [77] Xing S, Guo H. Temporal phase unwrapping for fringe projection profilometry aided by recursion of chebyshev polynomials. *Appl Opt* 2017;56(6):1591–602.
- [78] Saldner HO, Huntley JM. Temporal phase unwrapping: application to surface profiling of discontinuous objects. *Appl Opt* 1997;36(13):2770–5.
- [79] Towers CE, Towers DP, Jones JD. Optimum frequency selection in multifrequency interferometry. *Opt Lett* 2003;28(11):887–9.
- [80] Takeda M, Gu Q, Kinoshita M, Takai H, Takahashi Y. Frequency-multiplex fourier-transform profilometry: a single-shot three-dimensional shape measurement of objects with large height discontinuities and/or surface isolations. *Appl Opt* 1997;36(22):5347–54.
- [81] Zhong J, Wang M. Phase unwrapping by lookup table method: application to phase map with singular points. *Opt Eng* 1999;38(12):2075–81.
- [82] Zuo C, Huang L, Zhang M, Chen Q, Asundi A. Temporal phase unwrapping algorithms for fringe projection profilometry: a comparative review. *Opt Lasers Eng* 2016;85:84–103.
- [83] Schreiber H, Bruning JH. Phase shifting interferometry. In: Optical shop testing; 2006. p. 547–666.
- [84] Rastogi P, Hack E. Phase estimation in optical interferometry. CRC Press; 2014.
- [85] Hariharan P, Oreb B, Eiju T. Digital phase-shifting interferometry: a simple error-compensating phase calculation algorithm. *Appl Opt* 1987;26(13):2504–6.
- [86] Li J, Su X, Guo L. Improved fourier transform profilometry for the automatic measurement of three-dimensional object shapes. *Opt Eng* 1990;29(12):1439–45.
- [87] Su XY, Von Bally G, Vukicevic D. Phase-stepping grating profilometry: utilization of intensity modulation analysis in complex objects evaluation. *Opt Comm* 1993;98(1-3):141–50.
- [88] Zhang H, Lalor MJ, Burton DR. Spatiotemporal phase unwrapping for the measurement of discontinuous objects in dynamic fringe-projection phase-shifting profilometry. *Appl Opt* 1999;38(16):3534–41.
- [89] Zhang H, Wu F, Lalor MJ, Burton DR. Spatiotemporal phase unwrapping and its application in fringe projection fiber optic phase-shifting profilometry. *Opt Eng* 2000;39(7):1958–65.
- [90] Huang PS, Hu QJ, Chiang FP. Double three-step phase-shifting algorithm. *Appl Opt* 2002;41(22):4503–9.
- [91] Zhang C, Huang PS, Chiang FP. Microscopic phase-shifting profilometry based on digital micromirror device technology. *Appl Opt* 2002;41(28):5896–904.
- [92] Yoneyama S, Morimoto Y, Fujigaki M, Yabe M. Phase-measuring profilometry of moving object without phase-shifting device. *Opt Lasers Eng* 2003;40(3):153–61.
- [93] Huang PS, Zhang S, Chiang FP. Trapezoidal phase-shifting method for 3D shape measurement, 5606. International Society for Optics and Photonics; 2004. p. 142–53.
- [94] Huang PS, Zhang S, Chiang FP. Trapezoidal phase-shifting method for three-dimensional shape measurement. *Opt Eng* 2005;44(12):123601.
- [95] Huang PS, Zhang S. Fast three-step phase-shifting algorithm. *Appl Opt* 2006;45(21):5086–91.
- [96] Meng X, Cai L, Xu X, Yang X, Shen X, Dong G, et al. Two-step phase-shifting interferometry and its application in image encryption. *Opt Lett* 2006;31(10):1414–16.
- [97] Zhang S, Yau ST. High-resolution, real-time 3D absolute coordinate measurement based on a phase-shifting method. *Opt Express* 2006;14(7):2644–9.

- [98] Jia P, Kofman J, English C. Intensity-ratio error compensation for triangular-pattern phase-shifting profilometry. *J Opt Soc Am A* 2007;24(10):3150–8.
- [99] Jia P, Kofman J, English CE. Two-step triangular-pattern phase-shifting method for three-dimensional object-shape measurement. *Opt Eng* 2007;46(8):083201.
- [100] Zhang S, Yau ST. High-speed three-dimensional shape measurement system using a modified two-plus-one phase-shifting algorithm. *Opt Eng* 2007;46(11):113603.
- [101] Hu E, He Y. Surface profile measurement of moving objects by using an improved  $\pi$  phase-shifting fourier transform profilometry. *Opt Lasers Eng* 2009;47(1):57–61.
- [102] Hu E, He Y, Hua Y. Profile measurement of a moving object using an improved projection grating phase-shifting profilometry. *Opt Comm* 2009;282(15):3047–51.
- [103] Hu E, He Y, Wu W. Further study of the phase-recovering algorithm for saturated fringe patterns with a larger saturation coefficient in the projection grating phase-shifting profilometry. *Opt-Int J Light Electron Opt* 2010;121(14):1290–4.
- [104] Zhang S. Composite phase-shifting algorithm for absolute phase measurement. *Opt Lasers Eng* 2012;50(11):1538–41.
- [105] Li JL, Su HJ, Su XY. Two-frequency grating used in phase-measuring profilometry. *Appl Opt* 1997;36(1):277–80.
- [106] Liu K, Wang Y, Lau DL, Hao Q, Hassebrook LG. Dual-frequency pattern scheme for high-speed 3D shape measurement. *Opt Express* 2010;18(5):5229–44.
- [107] Wang Y, Liu K, Hao Q, Lau DL, Hassebrook LG. Period coded phase shifting strategy for real-time 3D structured light illumination. *IEEE Trans Image Process* 2011;20(11):3001–13.
- [108] Wissmann P, Schmitt R, Forster F. Fast and accurate 3D scanning using coded phase shifting and high speed pattern projection. In: 2011 international conference on 3d imaging, modeling, processing, visualization and transmission; 2011. p. 108–15. doi:10.1109/3DIMPVT.2011.21.
- [109] Zuo C, Chen Q, Gu G, Feng S, Feng F. High-speed three-dimensional profilometry for multiple objects with complex shapes. *Opt Express* 2012;20(17):19493–510.
- [110] Zhang Y, Xiong Z, Wu F. Unambiguous 3D measurement from speckle-embedded fringe. *Appl Opt* 2013;52(32):7797–805.
- [111] Zuo C, Chen Q, Gu G, Feng S, Feng F, Li R, et al. High-speed three-dimensional shape measurement for dynamic scenes using bi-frequency tripolar pulse-width-modulation fringe projection. *Opt Lasers Eng* 2013;51(8):953–60.
- [112] Budianto B, Lun P, Hsung TC. Marker encoded fringe projection profilometry for efficient 3D model acquisition. *Appl Opt* 2014;53(31):7442–53.
- [113] Zhang Y, Xiong Z, Yang Z, Wu F. Real-time scalable depth sensing with hybrid structured light illumination. *IEEE Trans Image Process* 2014;23(1):97–109.
- [114] Feng S, Chen Q, Zuo C. Graphics processing unit-assisted real-time three-dimensional measurement using speckle-embedded fringe. *Appl Opt* 2015;54(22):6865–73.
- [115] Tao T, Chen Q, Da J, Feng S, Hu Y, Zuo C. Real-time 3D shape measurement with composite phase-shifting fringes and multi-view system. *Opt Express* 2016;24(18):20253–69.
- [116] Liu X, Kofman J. Background and amplitude encoded fringe patterns for 3D surface-shape measurement. *Opt Lasers Eng* 2017;94:63–9.
- [117] Zhang S, Yau ST. High dynamic range scanning technique. *Opt Eng* 2009;48(3):033604.
- [118] Jiang H, Zhao H, Li X. High dynamic range fringe acquisition: a novel 3D scanning technique for high-reflective surfaces. *Opt Lasers Eng* 2012;50(10):1484–93.
- [119] Greivenkamp JE. Generalized data reduction for heterodyne interferometry. *Opt Eng* 1984;23(4):234350.
- [120] Huang PS, Zhang C, Chiang FP. High-speed 3D shape measurement based on digital fringe projection. *Opt Eng* 2003;42(1):163–9.
- [121] Weise T, Leibe B, Gool LV. Fast 3D scanning with automatic motion compensation. In: 2007 IEEE conference on computer vision and pattern recognition; 2007. p. 1–8. doi:10.1109/CVPR.2007.383291.
- [122] Angel JRP, Wizinowich P. A method for phase shifting interferometry in the presence of vibration. In: European southern observatory conference and workshop proceedings; 1988. p. 561–7.
- [123] Wizinowich PL. Phase shifting interferometry in the presence of vibration: a new algorithm and system. *Appl Opt* 1990;29(22):3271–9.
- [124] Jia P, Kofman J, English C. Multiple-step triangular-pattern phase shifting and the influence of number of steps and pitch on measurement accuracy. *Appl Opt* 2007;46(16):3253–62.
- [125] Takeda M, Ina H, Kobayashi S. Fourier-transform method of fringe-pattern analysis for computer-based topography and interferometry. *J Opt Soc Am* 1982;72(1):156–60.
- [126] Takeda M, Mutoh K. Fourier transform profilometry for the automatic measurement of 3D object shapes. *Appl Opt* 1983;22(24):3977–82.
- [127] Guo H, Huang PS. 3D shape measurement by use of a modified fourier transform method. *ProcSPIE* 2008;7066. doi:10.1117/12.798170.
- [128] Zuo C, Tao T, Feng S, Huang L, Asundi A, Chen Q. Micro fourier transform profilometry ( $\mu$ ftp): 3D shape measurement at 10,000 frames per second. *Opt Lasers Eng* 2018;102:70–91.
- [129] Rathjen C. Statistical properties of phase-shift algorithms. *J Opt Soc Am A* 1995;12(9):1997–2008. doi:10.1364/JOSAA.12.001997.
- [130] Surrel Y. Additive noise effect in digital phase detection. *Appl Opt* 1997;36(1):271–6. doi:10.1364/AO.36.000271.
- [131] Li J, Hassebrook LG, Guan C. Optimized two-frequency phase-measuring-profilometry light-sensor temporal-noise sensitivity. *J Opt Soc Am A* 2003;20(1):106–15. doi:10.1364/JOSAA.20.000106.
- [132] Servin M, Estrada JC, Quiroga JA, Mosino JF, Cywiak M. Noise in phase shifting interferometry. *Opt Express* 2009;17(11):8789–94. doi:10.1364/OE.17.008789.
- [133] Wang Y, Liu K, Lau DL, Hao Q, Hassebrook LG. Maximum snr pattern strategy for phase shifting methods in structured light illumination. *J Opt Soc Am A* 2010;27(9):1962–71. doi:10.1364/JOSAA.27.001962.
- [134] Zuo C, Chen Q, Gu G, Ren J, Sui X, Zhang Y. Optimized three-step phase-shifting profilometry using the third harmonic injection. *Opt Appl* 2013;43(2).
- [135] Zhang S. Comparative study on passive and active projector nonlinear gamma calibration. *Appl Opt* 2015;54(13):3834–41. doi:10.1364/AO.54.003834.
- [136] Guo H, He H, Chen M. Gamma correction for digital fringe projection profilometry. *Appl Opt* 2004;43(14):2906–14. doi:10.1364/AO.43.002906.
- [137] Waddington CJ, Kofman JD. Modified sinusoidal fringe-pattern projection for variable illuminance in phase-shifting three-dimensional surface-shape metrology. *Opt Eng* 2014;53. doi:10.1117/1.OE.53.8.084109.
- [138] Liu K, Wang Y, Lau DL, Hao Q, Hassebrook LG. Gamma model and its analysis for phase measuring profilometry. *J Opt Soc Am A* 2010;27(3):553–62. doi:10.1364/JOSAA.27.000553.
- [139] Peng JZ, Ouyang HK, Yu Q, Yu YJ, Wang KS. Phase error correction for fringe projection profilometry by using constrained cubic spline. *Adv Manuf* 2014;2(1):39–47. doi:10.1007/s40436-014-0058-1.
- [140] Kakunai S, Sakamoto T, Iwata K. Profile measurement taken with liquid-crystal gratings. *Appl Opt* 1999;38(13):2824–8. doi:10.1364/AO.38.002824.
- [141] Baker MJ, Xi J, Chicharo JF. Elimination of  $\gamma$  non-linear luminance effects for digital video projection phase measuring profilometers. In: 4th IEEE international symposium on electronic design, test and applications (delta 2008); 2008. p. 496–501. doi:10.1109/DELTA.2008.90.
- [142] Li Z, Li Y. Gamma-distorted fringe image modeling and accurate gamma correction for fast phase measuring profilometry. *Opt Lett* 2011;36(2):154–6. doi:10.1364/OL.36.000154.
- [143] Hoang T, Pan B, Nguyen D, Wang Z. Generic gamma correction for accuracy enhancement in fringe-projection profilometry. *Opt Lett* 2010;35(12):1992–4. doi:10.1364/OL.35.001992.
- [144] Lü F, Xing S, Guo H. Self-correction of projector nonlinearity in phase-shifting fringe projection profilometry. *Appl Opt* 2017;56(25):7204–16.
- [145] Su XY, Zhou WS, von Bally G, Vukicevic D. Automated phase-measuring profilometry using defocused projection of a ronchi grating. *Opt Comm* 1992;94(6):561–73. doi:10.1016/0030-4018(92)90606-R.
- [146] Lei S, Zhang S. Flexible 3D shape measurement using projector defocusing. *Opt Lett* 2009;34(20):3080–2. doi:10.1364/OL.34.003080.
- [147] Hu Y, Xi J, Chicharo J, Yang Z. Improved three-step phase shifting profilometry using digital fringe pattern projection. In: International Conference on Computer Graphics, Imaging and Visualisation (CGIV'06); 2006. p. 161–7. doi:10.1109/CGIV.2006.58.
- [148] van Wingerden J, Frankena HJ, Smorenburg C. Linear approximation for measurement errors in phase shifting interferometry. *Appl Opt* 1991;30(19):2718–29. doi:10.1364/AO.30.002718.
- [149] Stetson KA, Brohinsky WR. Electrooptic holography and its application to hologram interferometry. *Appl Opt* 1985;24(21):3631–7. doi:10.1364/AO.24.003631.
- [150] Surrel Y. Design of algorithms for phase measurements by the use of phase stepping. *Appl Opt* 1996;35(1):51–60. doi:10.1364/AO.35.000051.
- [151] Baker MJ, Xi J, Chicharo JF. Neural network digital fringe calibration technique for structured light profilometers. *Appl Opt* 2007;46(8):1233–43. doi:10.1364/AO.46.001233.
- [152] Hibino K, Oreb BF, Farrant DI, Larkin K. Phase shifting for nonsinusoidal waveforms with phase-shift errors. *J Opt Soc Am A* 1995;12(4):761–8. doi:10.1364/JOSAA.12.000761.
- [153] Ekstrand L, Zhang S. Three-dimensional profilometry with nearly focused binary phase-shifting algorithms. *Opt Lett* 2011;36(23):4518–20. doi:10.1364/OL.36.004518.
- [154] Zhang S, Huang PS. Phase error compensation for a 3D shape measurement system based on the phase-shifting method. *Opt Eng* 2007;46:063601. doi:10.1117/1.2746814.
- [155] Zhang S, Yau ST. Generic nonsinusoidal phase error correction for three-dimensional shape measurement using a digital video projector. *Appl Opt* 2007;46(1):36–43. doi:10.1364/AO.46.000036.
- [156] Pan B, Kemao Q, Huang L, Asundi A. Phase error analysis and compensation for nonsinusoidal waveforms in phase-shifting digital fringe projection profilometry. *Opt Lett* 2009;34(4):416–18. doi:10.1364/OL.34.000416.
- [157] Xiong L, Jia S. Phase-error analysis and elimination for nonsinusoidal waveforms in hilbert transform digital-fringe projection profilometry. *Opt Lett* 2009;34(15):2363–5. doi:10.1364/OL.34.002363.
- [158] Ma S, Quan C, Zhu R, Chen L, Li B, Tay C. A fast and accurate gamma correction based on fourier spectrum analysis for digital fringe projection profilometry. *Opt Comm* 2012;285(5):533–8. doi:10.1016/j.optcom.2011.11.041.
- [159] Ma S, Zhu R, Quan C, Li B, Tay C, Chen L. Blind phase error suppression for color-encoded digital fringe projection profilometry. *Opt Comm* 2012;285(7):1662–8. doi:10.1016/j.optcom.2011.12.027.
- [160] Li B, Wang Y, Dai J, Lohry W, Zhang S. Some recent advances on superfast 3D shape measurement with digital binary defocusing techniques. *Opt Lasers Eng* 2014;54:236–46.
- [161] Zhang S. Flexible 3D shape measurement using projector defocusing: extended measurement range. *Opt Lett* 2010;35(7):934–6. doi:10.1364/OL.35.000934.
- [162] Zhang Q, Su X, Xiang L, Sun X. 3D shape measurement based on complementary gray-code light. *Opt Lasers Eng* 2012;50(4):574–9. doi:10.1016/j.optlaseng.2011.06.024.
- [163] Zheng D, Da F, Kemao Q, Seah HS. Phase-shifting profilometry combined with gray-code patterns projection: unwrapping error removal by an adaptive median filter. *Opt Express* 2017;25(5):4700–13. doi:10.1364/OE.25.004700.
- [164] Zheng D, Kemao Q, Da F, Seah HS. Ternary gray code-based phase unwrapping for 3D measurement using binary patterns with projector defocusing. *Appl Opt* 2017;56(13):3660–5. doi:10.1364/AO.56.003660.

- [165] Wang Y, Zhang S. Novel phase-coding method for absolute phase retrieval. *Opt Lett* 2012;37(11):2067–9. doi:10.1364/OL.37.002067.
- [166] Li B, Fu Y, Zhang J, Wu H, Zeng Z. Period correction method of phase coding fringe. *Opt Rev* 2015;22(5):717–23. doi:10.1007/s10043-015-0137-y.
- [167] Hyun JS, Zhang S. Superfast 3D absolute shape measurement using five binary patterns. *Opt Lasers Eng* 2017;90:217–24. doi:10.1016/j.optlaseng.2016.10.017.
- [168] Gong Y, Zhang S. Ultrafast 3D shape measurement with an off-the-shelf DLP projector. *Opt Express* 2010;18(19):19743–54. doi:10.1364/OE.18.019743.
- [169] Zhang S, Weide DVD, Oliver J. Superfast phase-shifting method for 3D shape measurement. *Opt Express* 2010;18(9):9684–9. doi:10.1364/OE.18.009684.
- [170] Su XY, Zhou WS, Von Bally G, Vukicevic D. Automated phase-measuring profilometry using defocused projection of a ronchi grating. *Opt Comm* 1992;94(6):561–73.
- [171] Xian T, Su X. Area modulation grating for sinusoidal structure illumination on phase-measuring profilometry. *Appl Opt* 2001;40(8):1201–6.
- [172] Ayubi GA, Ayubi JA, Di Martino JM, Ferrari JA. Pulse-width modulation in defocused three-dimensional fringe projection. *Opt Lett* 2010;35(21):3682–4.
- [173] Zuo C, Chen Q, Feng S, Feng F, Gu G, Sui X. Optimized pulse width modulation pattern strategy for three-dimensional profilometry with projector defocusing. *Appl Opt* 2012;51(19):4477–90.
- [174] Wang Y, Zhang S. Superfast multifrequency phase-shifting technique with optimal pulse width modulation. *Opt Express* 2011;19(6):5149–55.
- [175] Wang Y, Zhang S. Three-dimensional shape measurement with binary dithered patterns. *Appl Opt* 2012;51(27):6631–6.
- [176] Dai J, Zhang S. Phase-optimized dithering technique for high-quality 3D shape measurement. *Opt Lasers Eng* 2013;51(6):790–5.
- [177] Dai J, Li B, Zhang S. High-quality fringe pattern generation using binary pattern optimization through symmetry and periodicity. *Opt Lasers Eng* 2014;52:195–200.
- [178] Dai J, Li B, Zhang S. Intensity-optimized dithering technique for three-dimensional shape measurement with projector defocusing. *Opt Lasers Eng* 2014;53:79–85.
- [179] Sun J, Zuo C, Feng S, Yu S, Zhang Y, Chen Q. Improved intensity-optimized dithering technique for 3D shape measurement. *Opt Lasers Eng* 2015;66:158–64.
- [180] Wang Y, Zhang S. Optimal pulse width modulation for sinusoidal fringe generation with projector defocusing. *Opt Lett* 2010;35(24):4121–3.
- [181] Schwider J, Burrow R, Elssner KE, Grzanna J, Spolaczyk R, Merkel K. Digital wave-front measuring interferometry: some systematic error sources. *Appl Opt* 1983;22(21):3421–32. doi:10.1364/AO.22.003421.
- [182] Schwider J. Phase shifting interferometry: reference phase error reduction. *Appl Opt* 1989;28(18):3889–92. doi:10.1364/AO.28.003889.
- [183] Creath K. Phase-measurement interferometry techniques. In: *Progress in Optics*, 26. Elsevier; 1988. p. 349–93. doi:10.1016/S0079-6638(08)70178-1.
- [184] Carré P. Installation et utilisation du comparateur photoélectrique et interférentiel du bureau international des poids et mesures. *Metrologia* 1966;2(1):13.
- [185] Cong P, Xiong Z, Zhang Y, Zhao S, Wu F. Accurate dynamic 3D sensing with fourier-assisted phase shifting. *IEEE J Select Top Signal Process* 2015;9(3):396–408. doi:10.1109/JSTSP.2014.2378217.
- [186] Li B, Liu Z, Zhang S. Motion-induced error reduction by combining fourier transform profilometry with phase-shifting profilometry. *Opt Express* 2016;24(20):23289–303. doi:10.1364/OE.24.023289.
- [187] Lu L, Xi J, Yu Y, Guo Q. New approach to improve the accuracy of 3D shape measurement of moving object using phase shifting profilometry. *Opt Express* 2013;21(25):30610–22. doi:10.1364/OE.21.030610.
- [188] Chen C, Cao YP, Zhong LJ, Peng K. An on-line phase measuring profilometry for objects moving with straight-line motion. *Opt Comm* 2015;336:301–5. doi:10.1016/j.optcom.2014.09.003.
- [189] Lu L, Ding Y, Luan Y, Yin Y, Liu Q, Xi J. Automated approach for the surface profile measurement of moving objects based on PSP. *Opt Express* 2017;25(25):32120–31. doi:10.1364/OE.25.032120.
- [190] Li Y, Cao YP, Huang ZF, Chen DL, Shi SP. A three dimensional on-line measurement method based on five unequal steps phase shifting. *Opt Comm* 2012;285(21):4285–9. doi:10.1016/j.optcom.2012.06.062.
- [191] Lau DL, Liu K, Hassebrook LG. Real-time three-dimensional shape measurement of moving objects without edge errors by time-synchronized structured illumination. *Opt Lett* 2010;35(14):2487–9. doi:10.1364/OL.35.002487.
- [192] Feng S, Chen Q, Zuo C, Li R, Shen G, Feng F. Automatic identification and removal of outliers for high-speed fringe projection profilometry. *Opt Eng* 2013;52:013605. doi:10.1117/1.OE.52.1.013605.
- [193] Lu L, Xi J, Yu Y, Guo Q. Improving the accuracy performance of phase-shifting profilometry for the measurement of objects in motion. *Opt Lett* 2014;39(23):6715–18. doi:10.1364/OL.39.006715.
- [194] Feng S, Zuo C, Tao T, Hu Y, Zhang M, Chen Q, et al. Robust dynamic 3D measurements with motion-compensated phase-shifting profilometry. *Opt Lasers Eng* 2018;103:127–38. doi:10.1016/j.optlaseng.2017.12.001.
- [195] Ekstrand L, Zhang S. Autoexposure for three-dimensional shape measurement using a digital-light-processing projector. *Opt Eng* 2011;50:123603. doi:10.1117/1.3662387.
- [196] Ri S, Fujigaki M, Morimoto Y. Intensity range extension method for three-dimensional shape measurement in phase-measuring profilometry using a digital micromirror device camera. *Appl Opt* 2008;47(29):5400–7. doi:10.1364/AO.47.005400.
- [197] Yin Y, Cai Z, Jiang H, Meng X, Xi J, Peng X. High dynamic range imaging for fringe projection profilometry with single-shot raw data of the color camera. *Opt Lasers Eng* 2017;89:138–44. doi:10.1016/j.optlaseng.2016.08.019.
- [198] Waddington C, Kofman J. Saturation avoidance by adaptive fringe projection in phase-shifting 3D surface-shape measurement. In: 2010 international symposium on optomechatronic technologies; 2010. p. 1–4. doi:10.1109/ISOT.2010.5687390.
- [199] Waddington C, Kofman J. Sinusoidal fringe-pattern projection for 3D surface measurement with variable illuminance. In: 2010 international symposium on optomechatronic technologies; 2010. p. 1–5. doi:10.1109/ISOT.2010.5687389.
- [200] Li D, Kofman J. Adaptive fringe-pattern projection for image saturation avoidance in 3D surface-shape measurement. *Opt Express* 2014;22(8):9887–901. doi:10.1364/OE.22.009887.
- [201] Zhang C, Xu J, Xi N, Zhao J, Shi Q. A robust surface coding method for optically challenging objects using structured light. *IEEE Trans Autom Sci Eng* 2014;11(3):775–88. doi:10.1109/TASE.2013.2293576.
- [202] Babaie G, Abolbashi M, Farahi F. Dynamics range enhancement in digital fringe projection technique. *Precis Eng* 2015;39:243–51. doi:10.1016/j.precisioneng.2014.06.007.
- [203] Lin H, Gao J, Mei Q, He Y, Liu J, Wang X. Adaptive digital fringe projection technique for high dynamic range three-dimensional shape measurement. *Opt Express* 2016;24(7):7703–18. doi:10.1364/OE.24.007703.
- [204] Chen T, Lensch HPA, Fuchs C, Seidel HP. Polarization and phase-shifting for 3D scanning of translucent objects. In: 2007 IEEE conference on computer vision and pattern recognition; 2007. p. 1–8. doi:10.1109/CVPR.2007.383209.
- [205] Salahieh B, Chen Z, Rodriguez JJ, Liang R. Multi-polarization fringe projection imaging for high dynamic range objects. *Opt Express* 2014;22(8):10064–71. doi:10.1364/OE.22.010064.
- [206] Feng S, Zhang Y, Chen Q, Zuo C, Li R, Shen G. General solution for high dynamic range three-dimensional shape measurement using the fringe projection technique. *Opt Lasers Eng* 2014;59:56–71. doi:10.1016/j.optlaseng.2014.03.003.
- [207] Chen Y, He Y, Hu E. Phase deviation analysis and phase retrieval for partial intensity saturation in phase-shifting projected fringe profilometry. *Opt Comm* 2008;281(11):3087–90. doi:10.1016/j.optcom.2008.01.070.
- [208] Hu E, He Y, Chen Y. Study on a novel phase-recovering algorithm for partial intensity saturation in digital projection grating phase-shifting profilometry. *Opt - Int J Light Electron Opt* 2010;121(1):23–8. doi:10.1016/j.jille.2008.05.010.
- [209] Chen B, Zhang S. High-quality 3D shape measurement using saturated fringe patterns. *Opt Lasers Eng* 2016;87:83–9. doi:10.1016/j.optlaseng.2016.04.012.
- [210] Jiang C, Bell T, Zhang S. High dynamic range real-time 3D shape measurement. *Opt Express* 2016;24(7):7337–46. doi:10.1364/OE.24.007337.
- [211] Guo H, Lü B. Phase-shifting algorithm by use of hough transform. *Opt Express* 2012;20(23):26037–49.
- [212] Coggrave C, Huntley JM. Optimization of shape measurement system based on spatial light modulators. *Opt Eng* 2000;39(1):91–9.
- [213] Wang Y, Bhattacharya B, Winer EH, Kosmicki P, El-Ratal WH, Zhang S. Digital micromirror transient response influence on superfast 3D shape measurement. *Opt Lasers Eng* 2014;58:19–26.
- [214] Lu G, Wu S, Palmer N, Liu H. Application of phase-shift optical triangulation to precision gear gauging, 3520. International Society for Optics and Photonics; 1998. p. 52–64.
- [215] Tatsuno K, Tsunoda Y. Diode laser direct modulation heterodyne interferometer. *Appl Opt* 1987;26(1):37–40.
- [216] Onodera R, Ishii Y, Ohde N, Takahashi Y, Yoshino T. Effect of laser-diode power change on optical heterodyne interferometry. *J Light Technol* 1995;13(4):675–81.
- [217] Onodera R, Ishii Y. Phase-extraction analysis of laser-diode phase-shifting interferometry that is insensitive to changes in laser power. *J Opt Soc Am A* 1996;13(1):139–46. doi:10.1364/JOSAA.13.000139.
- [218] Okada K, Sato A, Tsujiuchi J. Simultaneous calculation of phase distribution and scanning phase shift in phase shifting interferometry. *Opt Comm* 1991;84(3-4):118–24.
- [219] Liu Q, Wang Y, He J, Ji F. Phase shift extraction and wavefront retrieval from interferograms with background and contrast fluctuations. *J Opt* 2015;17(2):025704.
- [220] Lu Y, Zhang R, Guo H. Correction of illumination fluctuations in phase-shifting technique by use of fringe histograms. *Appl Opt* 2016;55(1):184–97.
- [221] Chen C, Wan Y, Cao Y. Instability of projection light source and real-time phase error correction method for phase-shifting profilometry. *Opt Express* 2018;26(4):4258–70.
- [222] Wust C, Capson DW. Surface profile measurement using color fringe projection. *Mach Vis Appl* 1991;4(3):193–203. doi:10.1007/BF01230201.
- [223] Huang PS, Hu Q, Jin F, Chiang FP. Color-encoded digital fringe projection technique for high-speed 3D surface contouring. *Opt Eng* 1999;38:1065–71. doi:10.1117/1.602151.
- [224] Pan J, Huang PS, Chiang FP. Color-encoded digital fringe projection technique for high-speed 3D shape measurement: color coupling and imbalance compensation, 5265. International Society for Optics and Photonics; 2004. p. 205–13.
- [225] Pan J, Huang PS, Chiang FP. Color phase-shifting technique for three-dimensional shape measurement. *Opt Eng* 2006;45:013602. doi:10.1117/1.2151160.
- [226] Pan J, Huang PS, Chiang FP. Color-coded binary fringe projection technique for 3D shape measurement. *Opt Eng* 2005;44:023606. doi:10.1117/1.1840973.
- [227] Zhang Z, Towers CE, Towers DP. Time efficient color fringe projection system for 3D shape and color using optimum 3-frequency selection. *Opt Express* 2006;14(14):6444–55. doi:10.1364/OE.14.006444.
- [228] Su WH, Kuo CY. 3D shape reconstruction using multiple projections: a method to eliminate shadowing for projected fringe profilometry. *ProcSPIE* 2007;669811. doi:10.1117/12.738699.
- [229] Zhang Z, Towers DP, Towers CE. Snapshot color fringe projection for absolute three-dimensional metrology of video sequences. *Appl Opt* 2010;49(31):5947–53. doi:10.1364/AO.49.005947.
- [230] Zhang Z, Towers CE, Towers DP. Robust color and shape measurement of full color artifacts by rgb fringe projection. *Opt Eng* 2012;51:021109. doi:10.1117/1.OE.51.2.021109.

- [231] Zhang S, Huang PS. High-resolution, real-time three-dimensional shape measurement. *Opt Eng* 2006;45:123601. doi:10.1117/1.2402128.
- [232] Creath K. Step height measurement using two-wavelength phase-shifting interferometry. *Appl Opt* 1987;26(14):2810–16. doi:10.1364/AO.26.002810.
- [233] Wang Y, Zhang S, Oliver JH. 3D shape measurement technique for multiple rapidly moving objects. *Opt Express* 2011;19(9):8539–45. doi:10.1364/OE.19.008539.
- [234] Pan J, Huang PS, Zhang S, Chiang F-P. Color n-ary gray code for 3D shape measurement. In: *Proceedings of ICEM, Italy*; 2004.
- [235] Zheng D, Da F. Phase coding method for absolute phase retrieval with a large number of codewords. *Opt Express* 2012;20(22):24139–50. doi:10.1364/OE.20.024139.
- [236] Zhou C, Liu T, Si S, Xu J, Liu Y, Lei Z. An improved stair phase encoding method for absolute phase retrieval. *Opt Lasers Eng* 2015;66:269–78. doi:10.1016/j.optlaseng.2014.09.011.
- [237] Feng S, Chen Q, Zuo C, Sun J, Yu SL. High-speed real-time 3D coordinates measurement based on fringe projection profilometry considering camera lens distortion. *Opt Comm* 2014;329:44–56. doi:10.1016/j.optcom.2014.04.067.
- [238] Guan C, Hassebrook LG, Lau DL. Composite structured light pattern for three-dimensional video. *Opt Express* 2003;11(5):406–17. doi:10.1364/OE.11.000406.
- [239] Sansoni G, Redaelli E. A 3D vision system based on one-shot projection and phase demodulation for fast profilometry. *Meas Sci Technol* 2005;16(5):1109.
- [240] Yue HM, Su XY, Liu YZ. Fourier transform profilometry based on composite structured light pattern. *Opt Laser Technol* 2007;39(6):1170–5. doi:10.1016/j.optlastec.2006.08.014.
- [241] Christian Bruer-Burchardt Peter Khmstedt GN. Phase unwrapping using geometric constraints for high-speed fringe projection based 3D measurements. *ProcSPIE* 2013;8789. doi:10.1117/12.2020262.
- [242] Li Z, Zhong K, Li YF, Zhou X, Shi Y. Multiview phase shifting: a full-resolution and high-speed 3D measurement framework for arbitrary shape dynamic objects. *Opt Lett* 2013;38(9):1389–91. doi:10.1364/OL.38.001389.
- [243] Bruer-Burchardt C, Breitbarth A, Khmstedt P, Notni G. High-speed three-dimensional measurements with a fringe projection-based optical sensor. *Opt Eng* 2014;53:112213. doi:10.1117/1.OE.53.11.112213.
- [244] Garcia RR, Zakhora A. Consistent stereo-assisted absolute phase unwrapping methods for structured light systems. *IEEE J Select Top Signal Process* 2012;6(5):411–24. doi:10.1109/JSTSP.2012.2195157.
- [245] An Y, Hyun JS, Zhang S. Pixel-wise absolute phase unwrapping using geometric constraints of structured light system. *Opt Express* 2016;24(16):18445–59. doi:10.1364/OE.24.018445.
- [246] Jiang C, Li B, Zhang S. Pixel-by-pixel absolute phase retrieval using three phase-shifted fringe patterns without markers. *Opt Lasers Eng* 2017;91:232–41. doi:10.1016/j.optlaseng.2016.12.002.
- [247] Liu X, Kofman J. High-frequency background modulation fringe patterns based on a fringe-wavelength geometry-constraint model for 3D surface-shape measurement. *Opt Express* 2017;25(14):16618–28. doi:10.1364/OE.25.016618.
- [248] Tao T, Chen Q, Feng S, Hu Y, Da J, Zuo C. High-precision real-time 3D shape measurement using a bi-frequency scheme and multi-view system. *Appl Opt* 2017;56(13):3646–53. doi:10.1364/AO.56.003646.
- [249] Tao T, Chen Q, Feng S, Hu Y, Zhang M, Zuo C. High-precision real-time 3D shape measurement based on a quad-camera system. *J Opt* 2018;20(1):014009.
- [250] Guo H, He H, Yu Y, Chen M. Least-squares calibration method for fringe projection profilometry. *Opt Eng* 2005;44(3):033603.
- [251] Zhang S, Huang PS. Novel method for structured light system calibration. *Opt Eng* 2006;45(8):083601.
- [252] Li Z, Shi Y, Wang C, Wang Y. Accurate calibration method for a structured light system. *Opt Eng* 2008;47(5):053604.
- [253] Huang L, Chua PS, Asundi A. Least-squares calibration method for fringe projection profilometry considering camera lens distortion. *Appl Opt* 2010;49(9):1539–48.
- [254] Vo M, Wang Z, Hoang T, Nguyen D. Flexible calibration technique for fringe-projection-based three-dimensional imaging. *Opt Lett* 2010;35(19):3192–4.
- [255] Huang J, Wang Z, Xue Q, Gao J. Calibration of a camera-projector measurement system and error impact analysis. *Meas Sci Technol* 2012;23(12):125402.
- [256] Moreno D, Taubin G. Simple, accurate, and robust projector-camera calibration. In: *Second international conference on 3D imaging, modeling, processing, visualization and transmission (3DIMPVT)*. IEEE; 2012. p. 464–71.
- [257] Vo M, Wang Z, Pan B, Pan T. Hyper-accurate flexible calibration technique for fringe-projection-based three-dimensional imaging. *Opt Express* 2012;20(15):16926–41.
- [258] Yin Y, Peng X, Li A, Liu X, Gao BZ. Calibration of fringe projection profilometry with bundle adjustment strategy. *Opt Lett* 2012;37(4):542–4.
- [259] Zhao H, Wang Z, Jiang H, Xu Y, Dong C. Calibration for stereo vision system based on phase matching and bundle adjustment algorithm. *Opt Lasers Eng* 2015;68:203–13.
- [260] Li K, Bu J, Zhang D. Lens distortion elimination for improving measurement accuracy of fringe projection profilometry. *Opt Lasers Eng* 2016;85:53–64.
- [261] Wang Y, Zhang S. Optimal fringe angle selection for digital fringe projection technique. *Appl Opt* 2013;52(29):7094–8.
- [262] Zhou P, Liu X, Zhu T. Analysis of the relationship between fringe angle and three-dimensional profilometry system sensitivity. *Appl Opt* 2014;53(13):2929–35.
- [263] Zhang R, Guo H, Asundi AK. Geometric analysis of influence of fringe directions on phase sensitivities in fringe projection profilometry. *Appl Opt* 2016;55(27):7675–87.
- [264] Guo H, Liu G. Approximations for the arctangent function in efficient fringe pattern analysis. *Opt Express* 2007;15(6):3053–66.
- [265] Zhang S, Royer D, Yau ST. Gpu-assisted high-resolution, real-time 3D shape measurement. *Opt Express* 2006;14(20):9120–9.
- [266] Karpinsky NL, Hoke M, Chen V, Zhang S. High-resolution, real-time three-dimensional shape measurement on graphics processing unit. *Opt Eng* 2014;53(2):024105.